

Preliminary Investigations into the Evaporation Process using a High Brightness Electron Beam Gun

Paul R. Carrière

Masters of Engineering

Department of Mining and Materials Engineering

McGill University

Montreal, Quebec

2013-12-14

A thesis submitted to McGill University in partial fulfillment
of the requirements of a degree of
Masters of Engineering

©PR Carriere 2013

Acknowledgements

I would like to thank Jan Krygier, Dr. Sriraman Rajagopalan, Dr. Lihong Shang and the McGill Machine Shop staff for their technical support during the course of this research. I'd like to also thank Jim Bobyn, Barbara Hanley, Courtney Jeleco and Terry Zatylny for their assistance in navigating the administrative and bureaucratic landscape at McGill. Dmitri Sandler, Jason Gao, Rudi Klossak and Ralf Edinger at PAVAC continue to give hardware support, as well as insight into electron beam technology. Prof Raynald Gauvin, Prof Mathieu Brochu and Prof Frank Mucciardi provided many stimulating discussions on the topic of materials processing and characterization. I'd also like to thank Joel Larose and Dr Elvi Delgaard at Pratt and Whitney Canada, and Dr Simon Durham at MDS Coatings for their insight into the commercial applications of coatings and coating technology.

Most importantly, I would like to thank Prof Stephen Yue for his patience and encouragement during this challenging and sometimes confusing research.

The work conducted in this document has been supported by the Natural Sciences and Engineering Research Council of Canada(NSERC) as well as the Canadian Foundation for Innovation(CFI).

Abstract

The high power density and net power achievable with axial electron beams make them an invaluable tool in the deposition of refractory coatings. Yet, the exact details of the coating process are often hidden behind proprietary techniques and technology. The work contained in this document involves the first examination of electron beam physical vapour deposition hardware fabricated by PAVAC Industries, Canada. The document traces the evaporation process from start to finish, examining the vacuum system, electron beam gun parameters, heat transfer and vapour transport. Experiments demonstrating the relative importance of these topics are given, as well as their inter dependencies. The conclusions drawn illustrate the transient nature of the process, which is due to the exponential temperature dependence on the evaporation rate and the moving beam spot. The main objective of this thesis is to develop some intuition into the evaporation hardware, review the over 60+ years of electron beam evaporation research and establish the tools and procedures needed for future research in this exciting field.

ABRÉGÉ

La puissance de haute densité et nette réalisable avec des faisceaux d'électrons axiaux en font un outil précieux dans le dépôt de revêtements réfractaires. Pourtant, les détails exacts de la fabrication des revêtements sont souvent inconnus car les techniques et les technologies sont propriétaires. Dans ce document, le faisceau d'électrons utilisé pour la déposition physique en phase vapeur et fabriqué par PAVAC Industries, Canada est examiné pour la première fois. Le document examine le processus d'évaporation du début jusqu'à la fin, le système à vide, les paramètres du canon à faisceau d'électrons, le transfert de chaleur et la diffusion de la vapeur. Des expériences qui démontrent l'importance relative de ces sujets sont présentées, ainsi que leurs interdépendances. Les conclusions obtenues illustrent la nature transitoire du procédé, ce qui est expliqué par la dépendance exponentielle de la température sur le taux d'évaporation et le déplacement du faisceau. L'objectif principal de cette thèse est de comprendre le fonctionnement général de base du système d'évaporation par faisceau d'électrons, passer en revue plus de 60 ans de recherche sur l'évaporation par faisceau d'électrons et établir les outils et les procédures nécessaires pour l'étude future de ce domaine passionnant.

Table of Contents

Acknowledgements	ii
Abstract	iii
ABRÉGÉ	iv
List of Tables	viii
List of Figures	ix
1 Introduction	1
1.1 Materials research and engineered coatings	1
1.1.1 Vapour Deposition	4
1.1.2 Document Organization	6
2 Vacuum Technology	7
2.1 Vacuum Basics	7
2.1.1 Base Pressure	10
2.2 High Purity Coatings	17
2.3 Vacuum Materials	20
2.3.1 Target Holder Design and Fabrication	21
3 Electron Beam Generation	23
3.1 Electron Beam Technology	23
3.2 Electron Beam Gun	27
3.2.1 Laser Heating and Cathode Emission	29
3.2.2 Current Regulation	34
3.2.3 Focus Coil	36
3.2.4 Deflection Coils	44
3.3 PAVAC Electronics	51
3.3.1 High Voltage Power Supplies	52

3.3.2	Control System Architecture	52
4	Electron Beam Heating	54
4.1	Electron/Matter Interactions	54
4.2	Electron Beam Transit	55
4.2.1	Elastic Collisions: Transit Losses	56
4.2.2	Inelastic Collisions: Ionization	57
4.3	Backscatter and Secondary Electrons	60
4.3.1	BSE Losses & CASINO	62
4.3.2	Electron Beam Heat deposition	65
4.4	X-Ray Generation	66
4.5	Electron Beam Heating	69
4.5.1	Nickel Evaporations C3-C7: Global Heat Transfer	77
4.5.2	Heat Transfer Discussion	89
4.6	Heat Equation	90
4.6.1	Semi-infinite Solid with Surface Flux	92
4.6.2	Electron Beam Evaporation: 1 ^D Solver	95
5	Vapour Generation	110
5.1	Electron Beam Evaporation	110
5.2	Vapour Generation	111
5.2.1	Evaporation Theory	112
5.3	Deposition Rate	120
5.3.1	Co-Evaporation	122
5.3.2	Non-ideal Deposition Rates and Distribution	128
5.3.3	Spitting	131
5.3.4	Oxide Evaporation	136
5.4	Vapour Adsorption and Diffusion on a Substrate	148
6	Conclusion	150
6.1	Future Work	152
6.1.1	Hardware and Process Work	152
6.1.2	Experimental Work	154
	Appendices	157
A	Abbreviations	157

References 159

List of Tables

<u>Table</u>		<u>page</u>
2-1	Gas density and mean free path at various pressures	8
3-1	Electron beam processing methods and related gun parameter	25
3-2	Fit parameters of Eq. 3.10 for data shown in Fig. 3-19	47
3-3	Simulated deflection coil signals	49
4-1	C3-C7 Deflection pattern signals	79
4-2	C3-C7 Coating thickness	82
4-3	C3-C7 Conduction loss calculation	84
4-4	C3-C7 Radiative heating loss calculation	86
4-5	C3-C7 Net thermal accounting	87
4-6	Thermophysical material parameters of Nickel target [1]-[2]	94
4-7	Beam parameters for q_{beam} defined in Fig. 4-19	96
5-1	Cu-Ni deflection pattern	127
5-2	Cu-Ni co-evaporation parameters during D3, D4, D5 evaporation . . .	127
5-3	Technology comparison of axial EB-PVD coaters	134
5-4	Deposition parameters for Al_2O_3	143

List of Figures

<u>Figure</u>	List of Figures	<u>page</u>
2-2	Partial pressures of vacuum chamber at base pressure	13
2-3	Gettering effect of titanium	15
2-4	Determination of water pump speed	16
2-5	Target holder CAD model	22
2-6	Comparison of vacuum pumpdown	22
3-1	Axial and transverse electron beam evaporators	24
3-2	PAVAC electron beam column	28
3-3	Current density regimes for electron emission from a solid	30
3-4	Saturated beam current as a function of $L1$ at 60/80kV	31
3-5	Cathode wear after extended use	32
3-6	Localized cathode wear	33
3-7	Current regulation using bias voltage	34
3-8	Current regulation algorithm used in the PAVAC gun	35
3-9	Focus coil geometry	37
3-10	Focus current at 60kV with $L1 = 55\%$	38
3-11	Optical micrograph of solidified welds on 316 stainless steel as a function of focus current and pulse length	39
3-12	Solidified laps during pulsed beam operation	39
3-13	PAVAC chamber geometry	41

3-14 Solidified welds on 316 stainless steel showing beam projection	42
3-15 Shaded plot of beam projection according to Eq. 3.6	43
3-16 Effect of translation on work distance	44
3-17 Effect of beam deflection on temperature profile	45
3-18 Electrical and magnetic circuit used for beam deflection	46
3-19 Deflection coil transfer function	47
3-20 Flow diagram of deflection coil subsystem	48
3-21 Deflection coil distortion for square wave at 500Hz	49
3-22 Beam spot position and velocity for $[u, v]$ parameters of Table 3-3 . .	50
4-1 Inelastic collision cross section for electron impact	57
4-2 Scattering cross section of O_2	58
4-3 Normalized backscattered electron energy distribution	63
4-4 BSE convergence	64
4-5 Power distribution and electron range	66
4-6 Simulated heating profile from CASINO	67
4-7 X-Ray spectrum generated during electron impact	68
4-8 e^- beam heating with parasitic sources of energy loss	70
4-9 Simulated pool shape, fluid flow and temperature profile for rod-fed EB-PVD of Ti	75
4-10 Target cross section	78
4-11 C3-C7 Deflection pattern and velocity profile	79
4-12 Vapour pressure of nickel	81
4-13 $TC_{Holder2}$ readout during C3-C7 Ni evaporations	83
4-14 C3-C7: TC_{target} location and response	85

4-15 C3-C7: Assumed temperature profile and radial radiative power . . .	85
4-16 Proposed deflection pattern for improved evaporation behavior	89
4-17 Normalized temperature distribution for surface flux on semi-infinite solid	93
4-18 Comparison of analytical and numerical solution for 1 ^D constant sur- face flux	95
4-19 Incident power absorption of Ni as a function of beam velocities . . .	96
4-20 Surface temperature of Ni with $T_o = 300$ K	98
4-21 Normalized temperature-depth profiles for $\tau/2$ increments, demon- strating linear response of material for $T_o = 300$ K	99
4-22 Thermal response of Ni with $T_o = 1673$ K	100
4-23 Beam, radiation and evaporative flux of nickel	100
4-24 Transient surface heat flux for Ni evaporation at $v = 800$ cm s ⁻¹ at $T_o = 1673$ K	101
4-25 ψ as a function of T_o and beam FWHM for $v = 800$ cm s ⁻¹	103
4-26 Power and temperature profiles for $v = 800$ cm s ⁻¹ at $T_o = 1400$ K .	104
4-27 Power and temperature profiles for $v = 800$ cm s ⁻¹ at $T_o = 1600$ K .	105
4-28 ψ as a function of T_o and beam speed for FWHM = 950 μm	105
5-1 Evaporation rate for common elements	114
5-2 Evaporation rate of Ti-Al system	116
5-3 Evaporation ratio and net flux of Ti-Al System	117
5-4 SEM cross section of B5-Ti64	118
5-5 Configuration of source and substrate geometry and definitions	121
5-6 Schematic of co-evaporation	123
5-7 Co-Evaporation: effects of source separation and height	125

5-8	Plain view of target configuration used during Cu-Ni Experiments . . .	126
5-9	Thermocouple response during Cu-Ni co-evaporation	128
5-10	Viscous and molecular flow regions during high rate EB-PVD	129
5-11	Evaporation rate of aluminium as function of beam focussing	131
5-12	Plain view of molten particles condensed onto substrate C3 during nickel evaporation	132
5-13	Underside of Ni target post evaporation of substrates C3(ZrO_2 and C7 (Al_2O_3)	135
5-14	Charging of Al_2O_3 target	137
5-15	Partial pressure and relative composition of Al_2O_3 as a function of temperature [3]	139
5-16	Deflection pattern signals u, v used during Al_2O_3 evaporation	143
5-17	Deflection pattern comparison for C14 and C15	144
5-18	Beam speed comparison between C14 and C15	144
5-19	Thermophysical material parameters of Al_2O_3 [4]	145
5-20	Deflection pattern comparison for C14 and C15	146
5-21	Thornton zone model for coating microstructure	149

CHAPTER 1 Introduction

1.1 Materials research and engineered coatings

The use of advanced coatings continues to increase as new applications demand multiple, often conflicting material properties. For example, engineering materials often require a combination of high temperature strength, light weight, wear resistance, biocompatibility, low cost, etc. In most cases, a single material cannot meet these requirements effectively. The benefit of coatings are thus apparent: the surface properties (corrosion resistance, biocompatibility, etc.) are optimized independently of the bulk properties (high temperature strength, toughness, weight, etc.). Nowhere is this division of labour more apparent than the modern jet turbine blade, which operates in a corrosive, high stress, high temperature environment. The turbine solution is composed of three separate materials, each with a specific functionality:

- Single or polycrystalline superalloy substrate: high temperature strength and creep resistance
- Bond coat: adhesion; oxidation and corrosion resistance
- Ceramic top coat: thermal insulation between substrate and environment

By optimizing the three separate material systems for performance and compatibility, turbine designers have increased engine temperatures beyond the restrictions of any single material. Yet, the application of a coating will add to both the per unit

costs as well as the net development costs. In many cases, the high development cost will hinder or even prevent new materials solutions from being discovered and applied.

As an example, consider the Ni-based superalloys, which are composed of 8-11 elements combined in well-specified proportions. As the number of elements increases, the number of experiments required to predict the alloy properties increases rapidly. The traditional one-alloy-at-a-time approach becomes both slow and expensive, generally resulting in only incremental improvements on established knowledge and techniques. [5] This outcome can be seen as a search for the local performance minimum, with the barrier to broader investigations being time and capital.

Thus, we can classify material research objectives according to a spectrum. At one extreme, we have the continued refinement of an established technique. By definition, this approach has proven its success and with improved diagnostics, analysis and characterization, some subtle parameters can hopefully be teased out and manipulated. At the other end of the spectrum, we have the development of radically new tools, often the result of cross-discipline pollination. The hope is that new technology will reduce costs, improve performance or accelerate the rate of discovery. Both approaches have their respective advantage, and the philosophy taken during the course of this work is a rough version of the former, with the objective of establishing the latter.

Specifically, the results and discussion contained within this thesis form a preliminary examination of a novel deposition technology called Pulsed Electron-Beam Physical Vapor Deposition (PEB-PVD). Conceptually, PEB-PVD is simple: an electron beam sequentially evaporates an array of targets using the pulse capability. By varying the target materials and pulse sequence, new coating compositions can be rapidly prototyped. Thus, new material solutions can be investigated with only a fraction of the investment required from conventional Electron-Beam Physical Vapor Deposition (EB-PVD) techniques because the costly ingot development phase has been removed. The challenges are multidisciplinary, shifting from coating development to coating hardware development.

As will be shown, the process of vapour generation is extremely complex, even when considering the simplest case of a continuous beam evaporating a pure element. This work attempts to consolidate the 60+ years of research on thermal processing using electron beams, touching upon electromagnetism, optics, heat transfer and vacuum science. The philosophy is that by understanding and reproducing the established electron beam work, aberrations in pulsed evaporation can be identified and corrected according to known electron beam theory. Also, as the first student to work with this particular equipment, a conservative research schedule was taken in order to fully characterize each subsystem. It is hoped that by reading this thesis, incoming researchers can quickly familiarize themselves with the details surrounding both pulsed and conventional EB-PVD, as well as generalized electron beam processing.

As an example, one of the initial challenges was grasping the magnitude of the scales involved. During EB-PVD, electrons travel through a medium which is 100 million times less dense than atmospheric conditions at 50% of the velocity of light, delivering a heat flux which is 100,000 times that which is delivered by the sun to earths' outer atmosphere. As a result, the target is heated to a temperature anywhere between 5-10 times higher than room temperature, resulting in micrograms of vapour transferred from the target to the substrate, with a corresponding coating thickness which may be as thin as a single atom. The question arises: if we change one parameter by 5%, what will happen? It is hoped that this document will untangle the relevancy of each parameter, as well as establish the technological and theoretical underpinnings surrounding PEB-PVD.

1.1.1 Vapour Deposition

In general, coating processes can be divided into one of two types:

- Droplet transfer: plasma spraying, arc spraying, wire-explosion spraying, detonation gun coating, cold spray
- Atom-by-atom transfer: physical vapour deposition, ion plating, sputtering, chemical vapour deposition, electrodeposition

As mentioned, the focus of this work is the atom-by-atom transfer technique referred to as Electron-Beam Physical Vapor Deposition (EB-PVD). Thus, many of the concepts discussed in this document pertain to broader vapour deposition techniques, including vacuum systems, microstructure evolution and coating homogeneity.

During the EB-PVD process, the electron beam couples energy from the power supply to the target, resulting in an increased surface temperature. Unlike resistive or inductive heating, energy exchange between the electron beam (e^- beam) and evaporant occurs exactly where it is needed: on the evaporating surface. This allows the evaporating surface to be contained within an autogenous molten skull, thus minimizing crucible contamination. The advantage of EB-PVD becomes apparent when evaporating refractory materials, which often require surface temperature in excess of $2,000^\circ\text{C}$.

As will be shown, the exponential temperature dependence of evaporation makes EB-PVD extremely sensitive to process fluctuations. [6] The EB-PVD coating process is characterized according to three main features. First, the beam parameters such as power density, net power, and beam deflection must be controlled in order to accurately distribute the power of the small beam spot over a large area. [7] Second, the stability of heat transfer within the target is critical, since the heat distribution defines the temperature distribution. Finally, the conditions in which the vapour condense onto the substrate will dictate many of the final coating properties, which are linked to vacuum conditions. Throughout these chapters, experimental results are presented which illuminate the relative importance of each processing parameter.

Thus, this work will show which of these these parameters need to be well controlled as well as their interdependency. The approach is as generalized, since it is hoped that this understanding will inform the opportunities and limitations

surrounding the Pulsed Electron-Beam Physical Vapor Deposition (PEB-PVD) concept.

1.1.2 Document Organization

The organization of this document mimics the order of operations surrounding an EB-PVD deposition campaign. Chapter 2 discusses the first step in the coating process: drawing a high vacuum. It also discusses the importance of the vacuum with respect to coating, as well as the technology and techniques surrounding the deposition chamber. The following chapter discusses electron beams in general, with an emphasis on beam generation, focusing and deflection. Chapter 4 discusses the interaction between electrons and matter as well as the details surrounding heat transfer within the target. Finally, Chapter 5 discusses the details of vapour generation and condensation, with a specific focus on alloy and oxide evaporation, as well as coating distribution.

Each chapter demonstrates the relevant process parameters as they pertain to the net EB-PVD process. Certain sections will skip ahead in the process in order to maintain a coherent discussion of the topic at hand. Thus, the uninitiated will most likely be required to re-read certain sections, as the relevancy of a given section may not have been apparent. Unfortunately, no other structure could be identified which captured the inter-related nature of the EB-PVD process.

CHAPTER 2 Vacuum Technology

2.1 Vacuum Basics

Vacuum technology is not unique to EB-PVD, and is used in many other coating techniques including sputtering, cathodic arc, pulsed laser deposition, chemical vapour deposition and vacuum plasma spray. The vacuum requirements will form a significant fraction of the process cost, with improved vacuums adding exponentially greater costs and reduced productivity. In this context, the vacuum does not simply imply base pressure, but includes the materials, design, cleanliness and protocols used in designing and running a deposition process. In a very simple sense, the vacuum represents any reactions between the freshly condensed atoms and the environment. More precisely, evaporative coating is a process governed by non-equilibrium surface diffusion, and residual gas molecules can have a dramatic effect on the surface growth kinetics. [8] As an example, minute levels of fluid backstreaming from a pump may not register on pressure gauge, but can have negative consequences for the process as hydrocarbons crack on the hot substrate surface. Thus, a vacuum is a fundamental process parameter, and a thorough understanding of vacuum science and technology is critical to EB-PVD research.

A vacuum represents a reduced gas density, and it is illuminating to compare the various states of vacuum. Table 2-1 gives a broad range of vacuum levels as well as values for the vacuum related parameters. The mean free path represents

the length a molecule will travel before striking another molecule, the impingement rate represents the molecular flux and t_{ML} represents the time needed to saturate a surface with one layer of molecules, or a Monolayer (ML), assuming a unity condensation coefficient.

Pressure	Molecules/cm ³	Mean free path [m]	Impingement Rate [cm ⁻² s ⁻¹]	t_{ML} [s]
Solid matter	10 ²²	N/A	N/A	N/A
1000 mbar: Atmosphere	10 ¹⁹	5 · 10 ⁻⁸	10 ²³	10 ⁻⁹
1 mbar	10 ¹⁶	5 · 10 ⁻⁵	10 ²⁰	10 ⁻⁶
10 ⁻⁵ mbar	10 ¹¹	5	10 ¹⁵	10 ⁻¹
10 ⁻¹⁴ mbar: Best Lab	10 ²	5 · 10 ⁹	10 ⁶	10 ⁸
10 ⁻²¹ mbar: Deep Space	10 ⁻⁵	5 · 10 ¹⁶	10 ⁻¹	10 ¹⁵

Table 2–1: Gas density and mean free path at various pressures

Table 2–1 clearly shows that as the pressure is reduced, the impingement rate of residual gas molecules decreases accordingly, thus reducing the possibility for contamination. It is worth highlighting the incredible range of artificial vacuum (10¹⁷) achievable, as it demonstrates utility of this remarkable environment.

There are other reasons for operating in a high vacuum that are unique to EB-PVD, including:

1. Reduced coating contamination from ambient gas molecules
2. Reduced electron beam scattering from gas molecules
3. Prevention of voltage breakdown between anode and cathode
4. Erosion of cathode filament from excessive ion bombardment/sputtering

The PAVAC system operates in the High Vacuum (HV) regime, as defined by the spectrum of Fig. 2–1. The base pressure of the chamber is approximately

$2 \cdot 10^{-6}$ mbar. The manufacturer recommended maximum gun pressure is $5 \cdot 10^{-3}$ mbar, which, according to the experimentally observed decoupling ratio of 1:5 results in a maximum deposition pressure of approximately $1 \cdot 10^{-3}$ mbar.



Figure 2-1: Spectrum of vacuum pressure and definitions

Generally, the HV environment is defined by the onset of molecular flow of gas molecules. At atmospheric pressure, gas behaviour is governed by molecule-molecule interactions, referred to as the viscous flow regime. In HV, molecules are so sparse that the gas behaviour is governed by molecule-wall interactions, as molecule-molecule collisions are comparatively infrequent. The transition between viscous and molecular flow occurs when the chamber length scale supersedes the gas mean free path.

Because of the low density of fluid in the HV regime, convective heat transfer between components is negligible. Also, drawing a high vacuum requires two separate pumps: one that operates in the viscous regime, and another that operates in the molecular regime. HV pumps operate by capturing molecules which impinge on the pump inlet, and entail a unique design and operation. Extreme care must be taken when operating HV pumps, as accidental exposure to atmosphere could destroy the pump.

Readers interested in learning more about the art of vacuum systems are encouraged to consult the prominent textbooks by O'Hanlon [9] and Hablanian[10] as

well as the various technical briefs available from manufacturers. In the following sections, specifics relating the EB-PVD process with the vacuum will be discussed: base pressure, coating quality and materials.

2.1.1 Base Pressure

The ultimate pressure of a high-vacuum system is determined by the pumping speed versus the constant formation of gases within the vacuum chamber. Out-gassing, which is the release of gas molecules from the chamber surface, is the pressure limiting effect in an unbaked HV chamber. [9] Base pressure can also be limited by:

- **Backstreaming:** pump fluid vapours travel up the vacuum hose, and enter the chamber via diffusion or creep. Backstreaming can affect the base pressure, but will have dramatic effects on the coating quality due to hydrocarbon cracking particles interfering with the vapour growth kinetics
- **Leaks:** real leaks result from a poor seal between the chamber and atmosphere, while virtual leaks are created when gas is trapped inside blind tapped holes or between two smooth surfaces
- **Permeation:** Results from the permeation of gas through a metal or elastomer gasket and chamber walls
- **Diffusion:** Gas leaching out of the vacuum chamber materials due to a concentration gradient

The effects of leaks, backstreaming and diffusion can be made negligible by proper design, materials selection and system operation. Under this assumption,

the pressure can be mathematically described as:

$$P(t) = P_o e^{\frac{-St}{V}} + \frac{1}{S} * (Q_o + Q_d + Q_k) \quad (2.1)$$

where P_o [mbar] is the initial pressure(usually 1000mbar), S [liter s⁻¹] is the pumping speed, V [liter] is the volume, t [s] is time, and Q_i [mbar liter s⁻¹] are the gas loads.

The first term of Eq. 2.1 represents the initial evacuation of the chamber, and rapidly goes to zero. Therefore, the final pressure is defined by the gas loads, $\sum Q_i$, and pumping speed, S .

Q_o represents the release of gas molecules weakly bonded to the chambers' interior surface, and is referred to as desorption, or outgassing. In most cases, Q_o decays as t^{-n} , where n is between 1 and 2. [9] Q_d represents the diffusion gas load, and initially decays as \sqrt{t} . Q_k is the permeation gas load, and is a constant function of time.

In an unbaked system, the gas load is dominated by outgassing, Q_o , and is composed predominately of water vapour. Unbaked, routinely cycled systems such as the PAVAC system are never pumped below the outgassing limit. Therefore, the physics surrounding adsorption and desorption merit a further discussion. The theory presented also pertains to vapour condensation, as the mechanics are identical.

Outgassing

Gas molecules can become physi- and chemisorbed on the vacuum surfaces, and are commonly referred to as adatoms. The adatoms are arranged in planes

referred to as a Monolayer (ML) with a single plane containing approximately 10^{15} atoms cm^{-2} . As an example, the number of molecules in a $1,000,000 \text{ cm}^3 (1\text{m}^3)$ square chamber at a pressure of 10^{-5} mbar is equivalent to a single ML of 100cm^2 . Thus, the interior surface represents a reservoir of gaseous atoms, which desorb into the vacuum space at a rate which will define the pressure. The desorption rate is defined by the average residence time that an adatom stays on the surface:

$$t = t_o * \exp\left(\frac{-E_d}{RT}\right) \quad (2.2)$$

where t_o is constant ($\approx 10^{-12}\text{s}$), $E_d[\text{J mol}^{-1}]$ is the specific heat of adsorption for the molecule/surface pair and R is the gas constant. [9] Long residence times mean low desorption rates, which result in small gas loads and lower base pressure.

In the EB-PVD chamber, the composition of the adsorbed gases consists of large quantities of water vapour along with nitrogen, oxygen, helium and carbon oxides. [11] Interestingly, the composition of the desorbed gas within the chamber does not match the composition of the atmosphere. This is experimentally demonstrated using a residual gas analyser to measure the gas composition of at a base pressure of $2*10^{-6}$ mbar, with the results shown in Fig 2-2.

The high concentration of water vapour is attributed to its room temperature residence time of 28hr, which is short enough to desorb at appreciable rates, but long enough that waiting multiple time constants is impractical. [9] This motivates the practice of baking a vacuum chamber in order to decrease the residence time, thus depleting the reservoir of adsorbed water vapour.

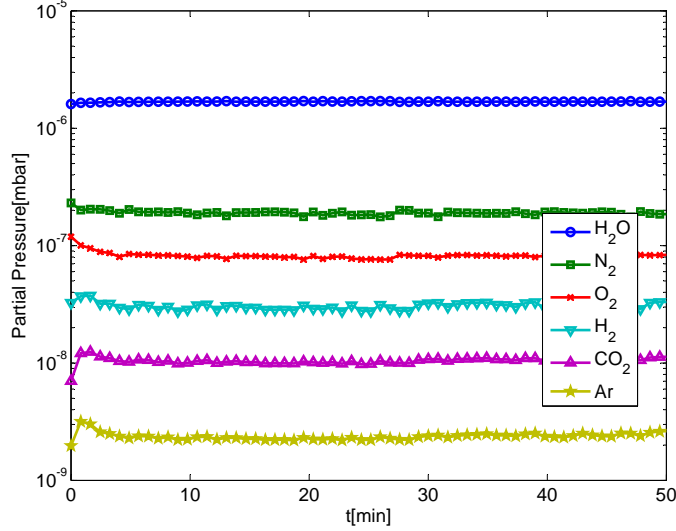


Figure 2-2: Partial pressures of vacuum chamber at base pressure, $2\text{E-}6$ mbar. The residual gas analysis was taken with a Thermo-Scientific Smart IQ+ quadrupole mass spectrometer. The ionizing electron energy was 67.2 eV, with ion intensity correction factors of 0.740, 1.000, 0.830, 0.406, 1.390, 1.450 for H_2O , N_2 , O_2 , He_2 , CO_2 , Ar, respectively

The nature and quantity of the adsorbed layer is also a function of the gas used to vent the system to atmosphere and the time exposed to atmosphere. This motivated the installation of a gas handling system that vents to atmosphere using dry N_2 , since N_2 has a shorter residence time than H_2O . Also, when the chamber is left idle, the chamber is vented to approximately 100mbar with N_2 and valved off. The pressure differential between the chamber and atmosphere is sufficient to seal the elastomer o-rings and prevent further adsorption of water vapour.

During deposition, a porous deposit condenses onto the chamber walls which is capable of absorbing large amounts of atmospheric gas. High-vacuum

grade aluminium foil is installed within the chamber as a deposition shield, and periodically replaced. [12]

When the beam is energized, a significant amount of heat is transferred to the chamber walls via radiation and conduction, raising the chamber temperature. As Eq. 2.2 shows, this will decrease the residence time and result in increased gas load, Q_o . Also, as Back-Scattered Electrons (BSE) leave the target, the gas load will increase via a process called Electron Stimulated Desorption (ESD). [9] The implication is that, as the deposition process proceeds, the operating pressure will increase due to the increased desorption and ESD rates, which is shown in Fig. 2-3. This also implies that increased beam power results in increased evaporation rates, increased chamber temperature and increased pressure. This is an unfortunate scenario, as it will be shown that low pressure and high deposition rates are desirable.

Magnitude of gas load

During system characterization, it was not possible to determine the pumping speed of the CTI Cryogenics water pump via any information in the manual. Thus, a simple experiment was conducted to determine the pump speed while furthering the understanding of the vacuum system.

The experiment assumes that the outgassing coefficient and turbo pump speed are constant, and the chamber pressure is fit to the following equation:

$$P(t) = a * t^{-n} + b \tag{2.3}$$

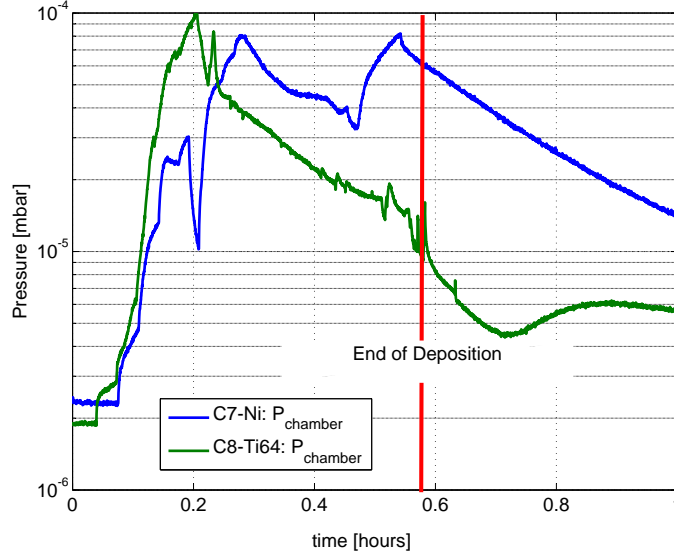


Figure 2-3: Gettering effect of titanium. Both depositions processes had similar beam power and deposition times. The above graph shows that the Ti vapor acts as a vacuum pump, lowering the pressure

which is motivated by Eq. 2.1, whereby $a = Q_o/S$, n is a fit parameter and b is a constant representing permeation and diffusion. The exponential term in Eq. 2.1 is ignored since the fit is performed in the HV regime and thus goes to zero.

To determine the pump speed, Eq. 2.3 is fit to a series of pressure windows:

1. P_1 : only turbo pump
2. P_2 : combined turbo and water pump
3. P_3 : only turbo pump

Ignoring the small conductance loss of the inline water pump, the rated pump speed of $S_{turbo} = 520 \text{ l s}^{-1}$ was used. The outgassing coefficient Q_o can then be determined via the fit parameter a . Thus, with the combined turbo and water

pumps, $S = S_{turbo} + S_{water}$ can be determined under the assumption that Q_o remains constant. The result of this measurement and fit is shown in Fig 2-4.

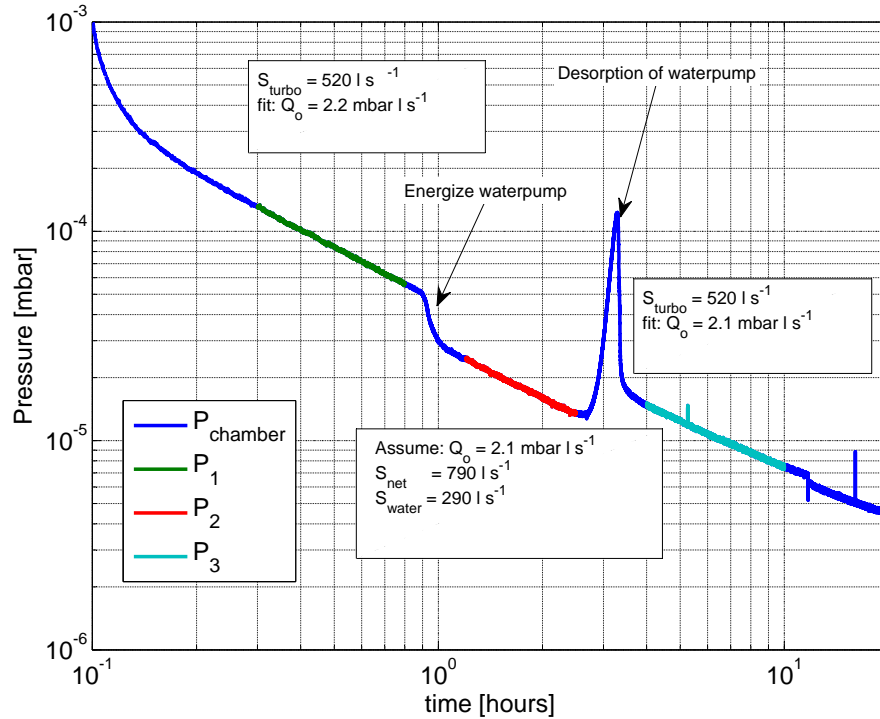


Figure 2-4: Determination of water pump speed, demonstrating pressure windows, and curve fitting results

As shown above, the outgassing rate before the water pump is energized is nearly identical to the outgassing rate after the cryopump has warmed up ($2.2 \cdot 10^{-2}$ vs $2.1 \cdot 10^{-2}$ mbar l s $^{-1}$). The water pump speed was determined to be 290 l s^{-1} . Besides determining a useful system parameter, this experiment demonstrates the orders of magnitude that occur during system operation.

2.2 High Purity Coatings

During the coating process, vapour of the target material condense onto the substrate surface. As demonstrated, a vacuum is not perfect, thus residual gas molecules impinge on the substrate as well (Note: vapour refers to the material being evaporated, while gas refers to the residual gases within the chamber). Depending on the species, these gas molecules will chemically react with the nucleating vapour molecules, and may be detrimental to the film structure and thus performance (ie crystallinity, density, hardness, adherence, optical and electrical properties [13]). In some instances, these gas/vapour reactions are essential for depositing materials such as ceramics. Oxygen, water vapour and pump oils are possible reaction species, while argon and nitrogen have little or no observable effects. From a process perspective, the absolute pressure is less important than the ratio of evaporant molecules to contaminating molecules, which can be expressed as: [14, 15]

$$\frac{\nu_{gas}}{\nu_{vapor}} = 5550 * \frac{M_v p_i}{\rho a_k} \quad (2.4)$$

where ν_{gas} and ν_{vapor} [$\text{m}^{-2} \text{s}^{-1}$] are the particle specific collision rate, M_v is the molecular weight of the vapour particles, p_i [mbar] is the partial pressure of gas species i , ρ [g cm^{-3}] is the density of the evaporant and a_k [nm s^{-1}] is the deposition rate. High purity coatings require that this ratio is minimized, thus P_i should be minimized and a_k maximized.

The influence of the gas cannot be assessed by collision ratio alone as the surface diffusion, atomic ordering and activation energy will also determine the

surface reaction. From an operational perspective, these phenomena manifest themselves as the gas type, vapour type, substrate material, substrate temperature. [13]

For instance, chemically inactive species (Ar,He) will often have a small probability of condensation, and thus ν_{gas}/ν_{vapor} can approach unity without incorporation into the film. Conversely, the probability of condensation for oxygen, water vapour and hydrocarbons is significantly larger, thus the partial pressures of these components should be reduced when metallic coatings are desired.

Evaporation of reactive metals such as niobium, titanium and tantalum getter the contaminating gas molecules faster than they can be replaced, thus reducing the coating contamination at the substrate to a lower than expected value. [14] This can be demonstrated by comparing the vacuum pressure of similar Ni and Ti evaporations, which was shown in Fig. 2–3, and shows a surprising decrease in vacuum pressure as the process proceeds. Physically, the Ti is reacting and condensing the water vapour and O₂ during deposition, resulting in a reduction in chamber pressure.

Returning to Eq. 2.4, consider aluminium evaporation at a pressure of 10⁻⁴ mbar and deposition rates of 1, 10 and 100 nm s⁻¹. According to Eq. 2.4, $\nu_{gas}/\nu_{vapor} \approx 10, 1, 0.1$ respectively. Thus, even in the high vacuum regime, where gas density is 10 million times less than atmosphere, the gas and vapour collisions are comparable.

As another example, during EB-PVD of Yttria-stabilized Zirconia (YSZ) Thermal Barrier Coatings (TBC), oxygen is bled into the chamber in a process

called Reactive Evaporation (RE). At the Penn State Applied Naval Research Lab, TBCs are deposited at $\approx 30\text{nm s}^{-1}$ with a 90:10% Ar:O₂ pressure of 10^{-3} mbar, resulting in a $\nu_{gas}/\nu_{vapor} \approx 4$. [16]

At the opposite end of the spectrum, during molecular beam epitaxy, extremely low vacuum pressures are needed in order to precisely deposit very pure single MLs. Generally, deposition proceeds at 10^{-10} mbar and with a rate of 0.3 nm s^{-1} . [17] Thus, if depositing aluminium, $\nu_{gas}/\nu_{vapor} \approx 10^{-5}$, resulting in extremely accurate thin film composition and structure.

Finally, consider the McGill PEB-PVD pulsed evaporation concept, which uses a rotating carousel to move targets under the beam spot where they are sequentially evaporated with the goal of creating alloy coatings. In order to deposit true multi-element alloys, as opposed to a multi-layer, sandwich-type structures, approximately one ML should be deposited during each carousel rotation. If the carousel is spun at the maximum rotation rate of 1,200 RPM, the deposition rate is 20 ML s^{-1} , with a resulting vapour impingement rate of $2*10^{16}$ molecules $\text{cm}^{-2}\text{s}^{-1}$. In the best case scenario, the vacuum pressure during deposition remains at $1*10^{-5}\text{mbar}$, with the water being the major vapour constituent. The resulting gas impingement rate is $5*10^{15}$ molecules $\text{cm}^{-2}\text{s}^{-1}$, giving a impingement ratio of 0.25.

This section should highlight the importance of maintaining a low vacuum pressure. From a production perspective, vacuum pressure is both costly and time consuming, and the highest permissible base pressure is usually sought. From a research perspective, the vacuum pressure can thought of as noise with regards to

the coating performance, as surface reactions will introduce unknowns into new coating compositions or techniques.

2.3 Vacuum Materials

As shown in the previous sections show, vacuum pressure is an important processing parameter, and is defined by the chamber outgassing. Thus, the chamber materials will impact the coatings. Since many modifications were made within the interior of the vacuum chamber since the beginning of this thesis, a short discussion of the materials and designs will be given.

The materials used within a vacuum system will have a number of specifications including optical, electrical, magnetic and thermal. Also, the materials must lend themselves to joining, machining and cleaning. Beyond these conventional requirements, the materials must be vacuum compatible, implying a low permeability to atmospheric gas, low outgassing rate and a low vapour pressure at operating temperature. The surfaces within the chamber should also be smooth, as this will reduce the effective surface area for adsorbates. The ratio of projected to actual surface area due to roughness can be as low as 5 for smooth, electropolished aluminium and as high as 1000 for anodized aluminium. In practice, vacuum compatible materials have a ratio of ≈ 50 . [10] Similarly, single strand electrical cables should be used within the chamber, as multi-stranded cables have a very large surface area.

Component design should try to minimize surface area, be easily cleaned, account for thermal expansion (especially at joints), have a minimal vapour pressure at maximum operating temperature, not be porous, and free of cracks and

crevices. [18] Also, in the PEB-PVD system, the materials must be resistant to radiation and electron bombardment.

2.3.1 Target Holder Design and Fabrication

Due to mechanical issues surrounding the original carousel PEB-PVD assembly, the carousel was replaced with a stationary target holder. The target holder was designed to be ‘vacuum-compatible’ while accommodating the large heat loads associated with e⁻ beam thermal conduction. The specific design features include:

- Material: 6061-T6 Aluminum, good thermal conductivity and vacuum properties
- 316 stainless steel fasteners
- Vacuum compatible Rocol DryLube MoS₂ dry lubricant on stainless steel/stainless steel fastener pairs
- Minimize virtual leaks: no blind tapped holes and vented fasteners
- Vacuum-rated alumina thermocouple connectors and insulator sleeves
- Easily cleaned

The substrate holder was designed in SolidWorks and machined at McGill. A CAD image of the substrate holder with the thermocouple measurement locations is shown in Fig. 2-5.

As a comparison, the pump down curves of the evaporation chamber with the aluminium target holder and carousel are shown in Fig. 2-6. Compared to the original system, the aluminium target holder has a significantly smaller outgassing rate, which resulted in a 2000% reduction base pressure.

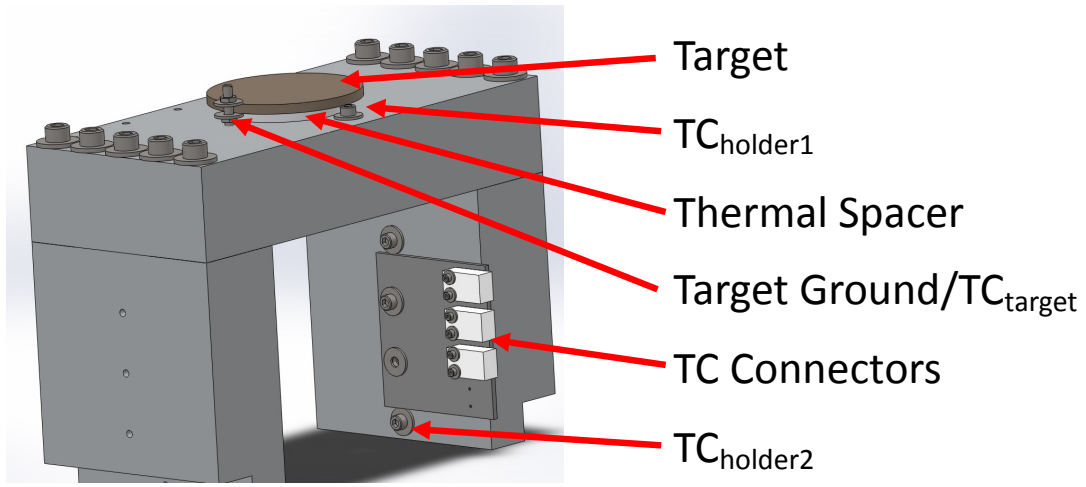


Figure 2-5: Target holder CAD model

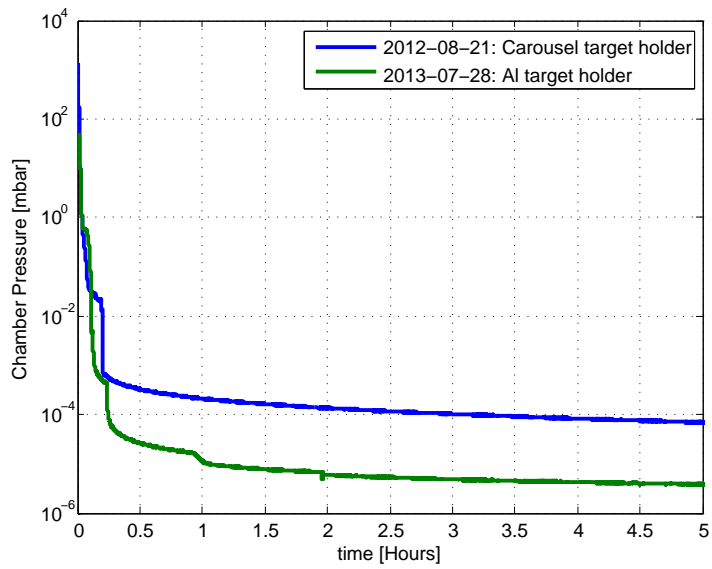


Figure 2-6: Comparison of vacuum pumpdown: Carousel vs. Aluminum target holder

CHAPTER 3 Electron Beam Generation

3.1 Electron Beam Technology

The developments of electron beam technology are intimately tied to advancements in vacuum engineering and electron optics. Although the possibility of electron beam heating was first investigated in 1905, it wasn't until the 1950s that demands in nuclear and space technology stimulated industrial research into electron beam processing. [15]

Interestingly, research and development in EB-PVD diverged as the Iron Curtain was raised. [19, 20] The Soviet Union developed axial e^- -beam coaters in order to coat steel with aluminium, as trade embargoes created zinc shortages. The result was over 100MW of total installed e^- -beam power, with the largest system exceeding 2MW. In the West, transverse coaters were well suited to the fast growing microelectronics industry, which required vapour sources for circuit metallization. Schematics of the transverse and axial electron beam configurations are shown in Fig. 3-1.

Transverse guns are generally simpler than axial guns, as the electron gun and crucible are contained within the same assembly. This design simplifies the vacuum requirement while maintaining high coating quality. Since the vacuum is a major system expense, transverse evaporators are significantly less expensive.

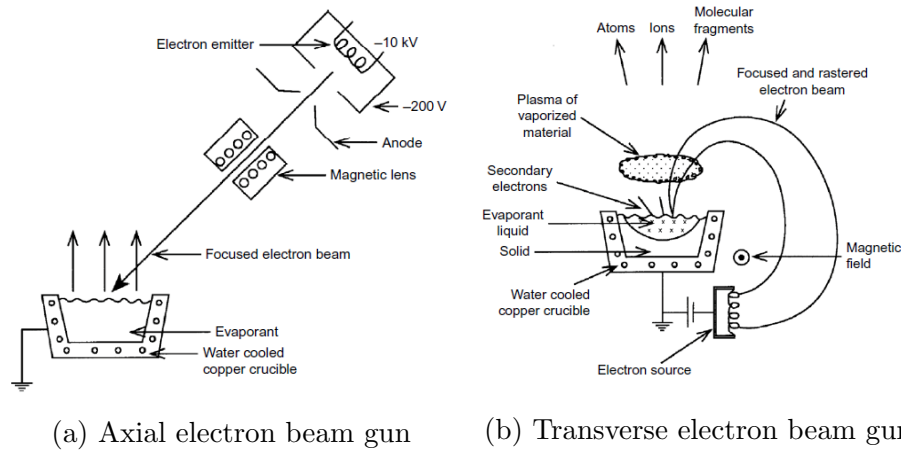


Figure 3-1: Axial and transverse electron beam evaporators.[8]

Unfortunately, aberrations incurred during magnetic beam bending limit the maximum power density, and the maximum power is limited to 10-15kW. [15]

Axial e^- beam guns are characterized by their sophisticated electron optics, which allow for variable power density and 2-axis beam deflection. Since the electron gun is physically separated from the crucible, axial guns are well suited for evaporation in poor or reactive vacuums. Also, the axial configuration allows the gun and crucible to be optimized independently. Consequently, axial electron beams are more expensive, but are generally associated with higher net powers and/or power densities than their transverse counterparts. [15]

The features associated with axial electron beam guns (high power, high power density, fast deflection) are utilized for a variety of applications. The intrinsic vacuum and high power are beneficial when casting purified ingots of refractory and reactive metals, in a process called electron beam melting.[15] Axial guns are also used for welding, where the high energy density and the penetrating

nature of the heat source results in a small heat-affected zone. Finally, the small spot sizes and precise electromagnetic deflection of axial guns are utilized in electron beam additive manufacturing, lithography and machining. Requirements for each of these e⁻beam thermal processes is given in Table. 3–1.

Processing	Power [W]	Power density [W m ⁻²]	U _b [kV]	Min spot size [mm]
Melting	10 ⁵ -10 ⁷	10 ³ -10 ⁴	20-50	10-50
Evaporation	10 ³ -10 ⁶	10 ³ -10 ⁴	10-40	2-30
Welding	10 ² -10 ⁵	10 ⁵ -10 ⁷	15-180	0.1-5
Machining	10-10 ³	10 ⁵ -10 ⁹	20-150	10 ⁻³ -0.1

Table 3–1: Electron beam processing methods and related gun parameters[21]

Table 3–1 shows that for a particular application, the gun design must provide a defined power, power density and spot size at the work plane. (Note: the work plane is defined by geometry, while the focal plane is defined by the optics). Unfortunately, gun design is an optimization process, since power density is roughly defined by the net power divided by the spot size, and will be limited by physics. Table 3–1 shows that as the net power increases, the power density decreases and spot size increases. The maximum current density, often referred to as brightness, is determined according to the following phenomenon: [15]

- Forces exerted on electrons due to the intrinsic space-charge of the beam
- Velocity distribution of emitted electrons
- Aberrations due to electron lens and the ion formation

The effect of the repulsive force between beam electrons can be determined according to the perveance, P , of the gun, which is defined according to:

$$P = \frac{I_b}{U_b^{3/2}} \quad (3.1)$$

where I_b is the beam current and U_b is the accelerating voltage. For instance, high power guns used for melting will have a high perveance ($>10^{-8}$), thus maximum power density is limited by space-charge effects. In the worst case scenario of 200mA at 20kV, the perveance of the PAVAC gun is $7*10^{-8}$, and space-charge effects will factor into the maximum achievable power density. Under the operating conditions used in this work ($<30\text{mA}$, 60kV), the perveance is $2*10^{-9}$ and the maximum power density is dictated by electron velocity and optics, which will be presented in later sections.

Finally, electron beams share many similarities to lasers, in that high power and power densities are achievable. The main distinction between the two sources are:

- Environment: e^- beams must operate in a vacuum, while lasers can operate in atmospheric conditions
- Power: electron beams are capable of achieving higher average power, while lasers can achieve higher peak powers
- Pulse Width: our equipment can reach microsecond pulse lengths while lasers can achieve pulse widths on the order of picoseconds
- Beam Steering: lasers require a mechanical system to steer the beam, while electron beams use magnetic fields

- Reflected Energy: e^- beams are sensitive to density and atomic number of the incident material, reflecting BSE power. Lasers reflect power as a function of surface reflectivity
- Depth of interaction: lasers and electron beams both have a variable depth of interaction, which are dependent on the material and the wavelength or accelerating voltage, respectively. The heat deposition of a laser goes as $exp(-x/\alpha)$, and thus peak heat is at the surface. The heat distribution for electron beam occur within the material, and has a more distributed nature
- Safety: e^- beam sources generate a spectrum of x-rays that require shielding. With lasers, special care must be taken to absorb the reflected beam

These distinctions are worth highlighting, as they offer some insight into the advantages and disadvantages of both lasers and electron beams.

3.2 Electron Beam Gun

The electron emitter, accelerating volume and electromagnetic lenses are commonly referred to as an electron beam gun. The purpose of the gun is to compress and deflect an image of the cathode electron emission onto the work plane. The electron beam gun installed at McGill is fabricated by PAVAC Industries, and is a differentially pumped, axial gun with a tungsten ribbon cathode. The gun design is the Rogowski-type, which can control the beam current without significant shifts in the focal plane. [15] The tungsten cathode is heated to electron emission using a fiber-coupled, 75W 808nm diode laser. Compared to resistive heating, laser heating does not create electromagnetic fields, resulting in lower electron velocities and improved beam brightness. [15] The PAVAC gun column is shown in Fig. 3-2.

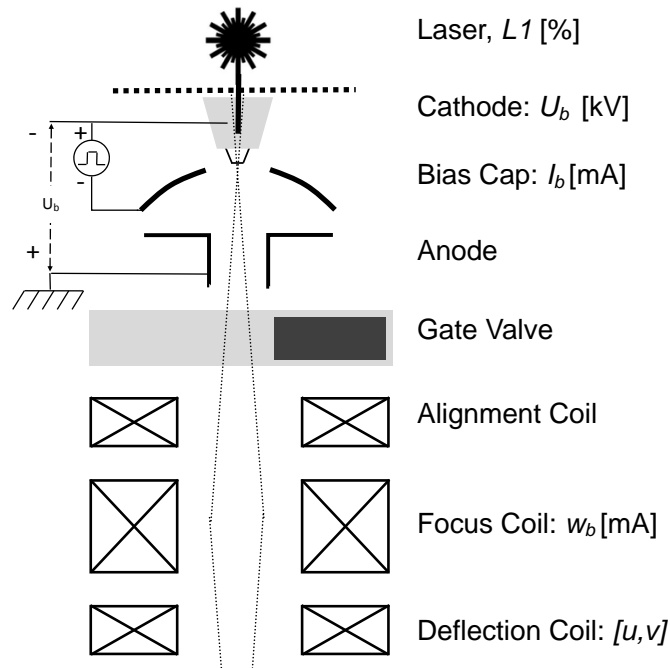


Figure 3–2: PAVAC electron beam column. User-defined beam parameters are shown in italic

The user controlled parameters of the gun are:

- $L1$: Laser power
- U_b : Accelerating voltage
- I_b : Beam current
- w_b : Focus current
- $[u, v]$: Deflection coil signals

Each sub-component will be briefly presented, as it pertains to the electron beam generation process.

3.2.1 Laser Heating and Cathode Emission

In order to generate electrons from a solid body, a cathode must be heated to a very high temperature. Tungsten cathodes are used for most thermal e^- beam processes because of their durability in poor vacuums, emission characteristics and high melting temperature.

When tungsten is heated to approximately 2500°C , electrons are emitted and form a cloud in front of the cathode surface. With no applied electric field, image charges prevent the electrons from escaping the cathode surface. As the electric field strength in front of the cathode is increased, electrons are swept from the cathode surface, forming an electron beam. Under the condition that a beam is formed while maintaining a reservoir of electrons, the gun is said to be operating in the space-charge limited regime. This is the normal operation mode of the PAVAC gun.

With increasing \mathbf{E} field, the current density will plateau as the electrons are swept out as rapidly as they are produced (ie no electron cloud). This is referred to as temperature-limited regime, and is rarely used in practice because of the challenges of regulating temperature. Finally, if the field strength is increased beyond 10^6 W cm^{-1} , electrons will be torn from the cathode surface in a process called field emission. These three operating regimes are shown in Fig. 3-3.

Generally, the current density of a tungsten cathode is $1\text{-}10 \text{ A cm}^{-2}$, and is a function of the accelerating voltage, surface temperature, and surface state. Fig. 3-3 shows that for a given \mathbf{E} field, the current density increases with increasing temperature.

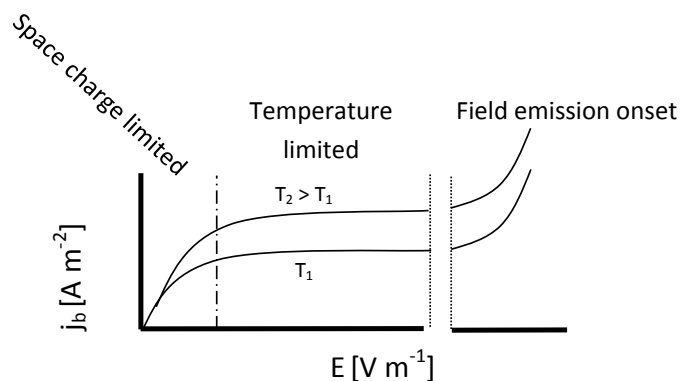


Figure 3-3: Current density regimes for electron emission from a solid as a function of accelerating field and temperature.

The concept of beam current as a function of surface temperature and surface state is demonstrated with a simple experiment. A new cathode was installed and the beam current was set to a theoretical 50mA, while the laser power $L1$ was varied. This current setting was chosen such that all electrons are swept from the cathode surface, i.e. the temperature-limited regime of Fig. 3-3. Since the laser heats the same area for all powers, this experiment measures the beam current as a function of temperature.

The $L1$ vs I_b curve of a virgin cathode is shown as *Run 1* in Fig. 3-4. After running the beam for approximately 10 minutes at a series of currents, the measurement was repeated and is displayed as *Run 2*. Finally, after 5 atmospheric venting operations and approximately 60 minutes of beam time, the measurement was repeated and displayed as *Run3*. Each measurement was performed at both 60kV and 80kV.

For a given run, Fig. 3-4 demonstrates that the saturated beam current is not a function of U_b , and we are therefore operating in the temperature-limited regime.

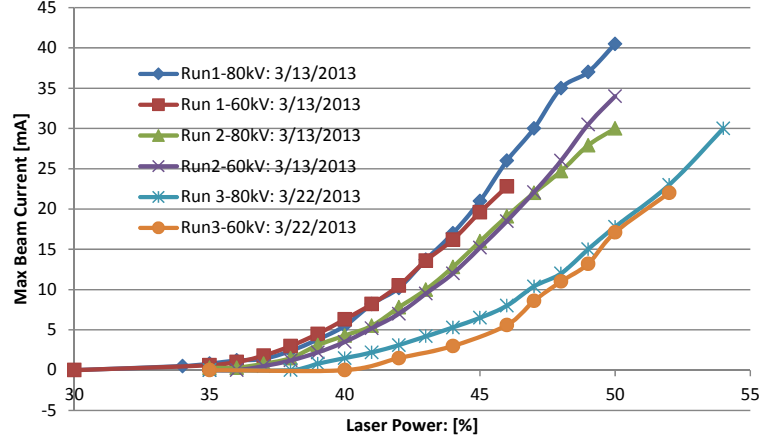


Figure 3–4: Saturated beam current as a function of $L1$ at 60/80kV

The most obvious trend of Fig. 3–4 is the expected increase in beam current with increasing laser power. Another interesting feature is the degradation of electron emission with time. This is especially apparent during *Run 3*, where we see that the beam current has significantly decreased for any given laser power.

The degradation is due to structural changes of the emission surface (sputtering) as well as chemical changes during atmospheric exposure (oxidation). [15] Also, the laser enters the vacuum via a window, which will become increasingly coated during EB-PVD. This coating will reflect and absorb laser power, reducing the cathode heating. Images of a used cathode and window are shown in Fig 3–5,3–6, demonstrating these effects.

Although not immediately obvious, the results of Fig 3–4 have important implications for the processing parameters during EB-PVD. Firstly, it can be shown that the minimum beam spot size, α goes according to:

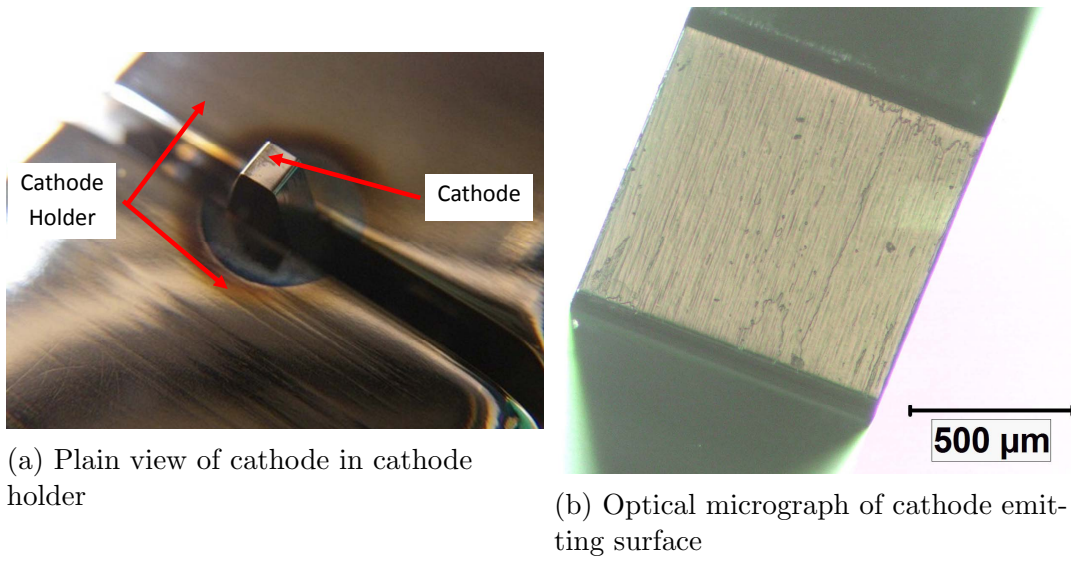


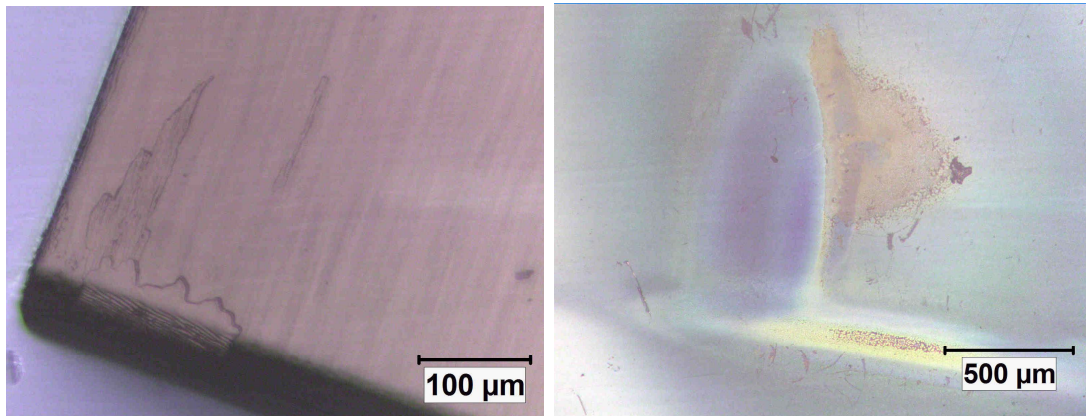
Figure 3-5: Cathode wear after approximately 60 minutes of emissions and 5 venting operations

$$\alpha \propto \left(\frac{T_{elec}}{U_b} \right)^{1/2} \quad (3.2)$$

where T_{elec} is the temperature of the emitting surface. Eq. 3.2 is a consequence of the Maxwellian velocity distribution of the electrons and the Liouville theorem of conserved phase space. [21] The implications of Eq. 3.2 is that minimum spot size (or maximum current density) is dependent on the temperature of the emitting surface. For a fixed bias cap voltage (and hence I_b), higher emitting temperatures result in a larger beam spot, and thus a lower current density. Therefore, the $L1$ setting should not be significantly higher than necessary.

A more subtle implication of Fig. 3-4 appears when examining the cathode surface. Fig. 3-5b shows localized regions of high sputter damage, especially near the corners which are subject to local \mathbf{E} field enhancement. The lower left corner

of Fig 3-5b is magnified and shown in Fig. 3-6a. Also, a magnified image of the window used to transmit the laser beam into the vacuum is shown in Fig. 3-6b. Although the orientation of the window and cathode was not maintained, it is believed that the damaged corners correspond with each other.



(a) Micrograph of cathode emitting surface

(b) Micrograph of laser transmission window

Figure 3-6: Cathode wear after approximately 60 minutes of emissions and 5 venting operations

Just as damage to the cathode will decrease the net current, local damage on the cathode will reduce the local electron emission. Since the purpose of the gun is to project an image of the electron emission onto the target surface, the damage shown in Fig. 3-6 will distort the power density at the target.

This demonstrates that the global and local power density of the electron spot will deteriorate with time until the emitting surface is completely eroded. This also highlights the importance of maintaining a good vacuum, as cathode and window damage is reduced with reduced pressure.

3.2.2 Current Regulation

In the space-charge limited regime, the beam current is a function of the electric field near the cathode surface. Thus, current regulation of the PAVAC gun is accomplished by the modifying the voltage of an intermediate electrode called the bias or Wehnelt cap.

Returning to the Fig. 3–2, we see that a negative voltage is applied between the grounded gun and the electrically isolated cathode, which is the accelerating voltage U_b . A bias cap voltage generator is connected in series with the negative terminal of the High Voltage Power Supply (HVPS). Thus, the beam current is regulated by modifying the \mathbf{E} field near the cathode surface via the bias cap voltage, as demonstrated in Fig 3–7.

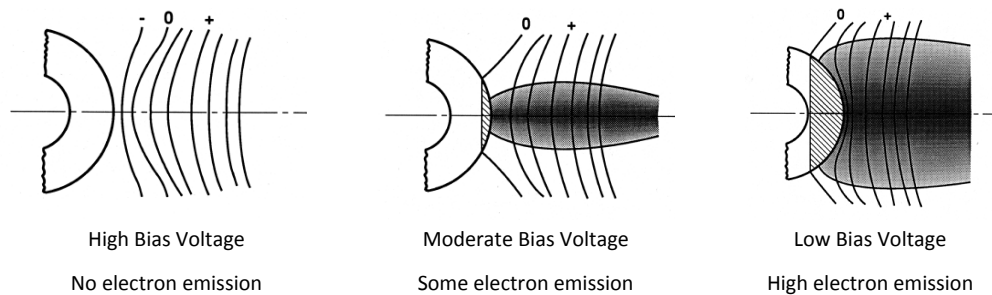


Figure 3–7: Current regulation using bias cap voltage. [22] The cathode is represented by the annular solid, while the field lines represent the \mathbf{E} field

As mentioned, a cloud of electrons forms in front of the hot cathode. By applying a bias voltage, the electric field near the cathode surface prevents the electrons from escaping, as shown in the leftmost image of Fig. 3–7. As the bias voltage is decreased, the zero point in the electric field is moved onto the cathode surface, allowing electrons to 'see' the accelerating field, as shown in the middle

image. With further decrease in the bias voltage, a larger \mathbf{E} field is applied to the cathode, further increasing the beam current. In the extreme case, whereby no bias voltage is applied, all the thermionic electrons will be swept from the cathode surface, and the gun will be operating in the temperature-limited regime.

In summary, changing the bias voltage changes the beam current, which is also the principle used in vacuum tube amplifiers. [21] It follows that pulsing the bias voltage will result in a pulsed electron beam.

In terms of operating the PAVAC machine in pulsed mode, a few words will be given to setting the machine parameters. During operation, the system samples the beam current, and adjusts the bias cap voltage to match the user requested beam current, I_b . The current feedback loop is shown in Fig. 3–8a.

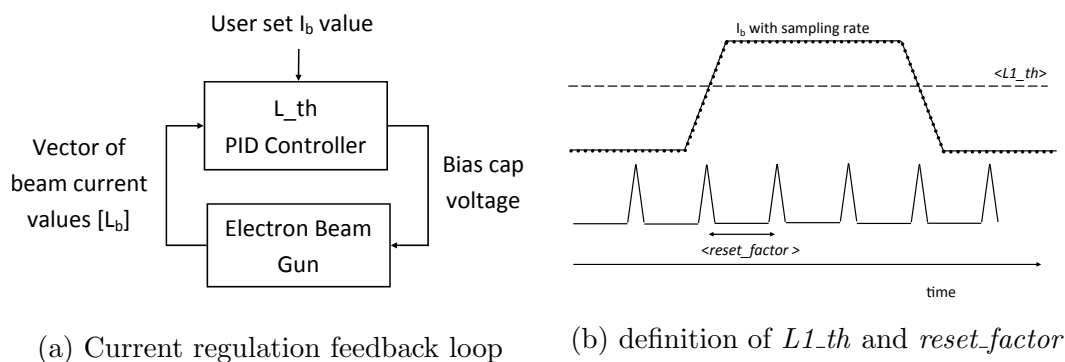


Figure 3–8: Current regulation algorithm used in the PAVAC gun

The controls accessible to the user are: $reset_factor$ [unitless] and $L1.th$ [mA]. $L1.th$ defines the threshold for activating the regulation algorithm, that is, regulation begins when the sampled current is greater than $L1.th$. This is shown in schematic of Fig. 3–8b, where the x-axis is time.

Although the beam current is constantly sampled, a vector of current samples is used during each regulation cycle, referred to as $[Lb]$. The difference between the set point (I_b) and the maximum value of $[Lb]$ is used as the error signal within the feedback loop. The number of samples included in $[Lb]$ is determined by the *reset_factor*, with small values of *reset_factor* resulting in short regulation cycles.

As an example, if $\max([Lb])$ is significantly different from I_b , having a small *reset_factor* will clear the artificially large error signal rapidly. If *reset_factor* is large, the period of inaccurate current regulation will be extended. For fast, accurate control of the beam current, it is recommended to start with a low value of *L1.th* and a long *reset_factor*. As the beam current stabilizes, the user should increase *L1.th* and decrease *reset_factor*.

3.2.3 Focus Coil

Electrons are focussed and deflected according to the Lorentz force:

$$\mathbf{F} = q[\mathbf{E} + \mathbf{v} \times \mathbf{B}] \quad (3.3)$$

In the PAVAC gun, a rotationally symmetric magnetic field is used to focus the electron beam onto the work plane. An image of a general focusing lens, as well as a description of the axial and tangential magnetic fields is given in Fig. 3–9. Electron focusing occurs due the coupled interaction with the B_r and B_z fields. When an electron of velocity v_z enters the lens along the optical axis, it interacts with the radial component of the magnetic field, B_r . According to the right hand rule, the vector product $-e(v_z \times B_r)$ produces a rotational force into the paper, F_{in} , giving the electron a rotational velocity v_{in} . This rotational velocity then

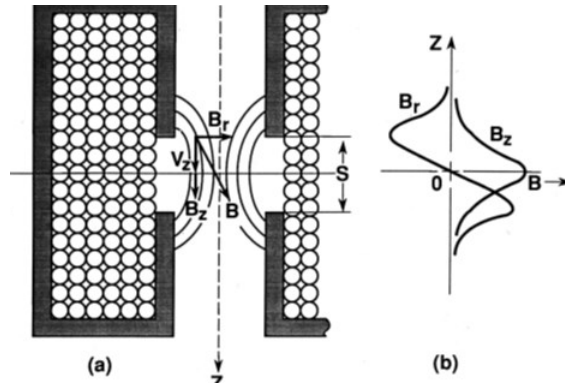


Figure 3-9: Focus coil geometry [22]

interacts with the axial component of the field (B_z), producing a radial force $F_r = -e(v_{in} \times B_z)$. This radial force causes the electron trajectory to curve toward the optic axis, steering the peripheral electrons towards the center, thus focusing the beam. The focusing action is described by the focal length of the lens, f_L given by:

$$f_L = G \frac{U_r}{(N * w_b)^2} \quad (3.4)$$

where G is an geometrical constant characteristic of the lens, N is the number of magnetic winding, w_b is the lens current, and U_r is the relativistically corrected acceleration voltage of the electrons. ($U_r = U_b(1 + 0.98 * 10^{-6} * U_b)$).[15]

Due to space-charge effects, the focal length of an e^- -beam gun is dependent on the beam current, I_b . To determine this dependency, a new cathode was installed in the gun. The focal length f_L was then varied via w_b in order to match the focal plane with the work plane. Focus was determined according to the w_b value which gave the optically brightest beam spot at the target. The resulting w_b vs. I_b curve is shown in Fig. 3-10.

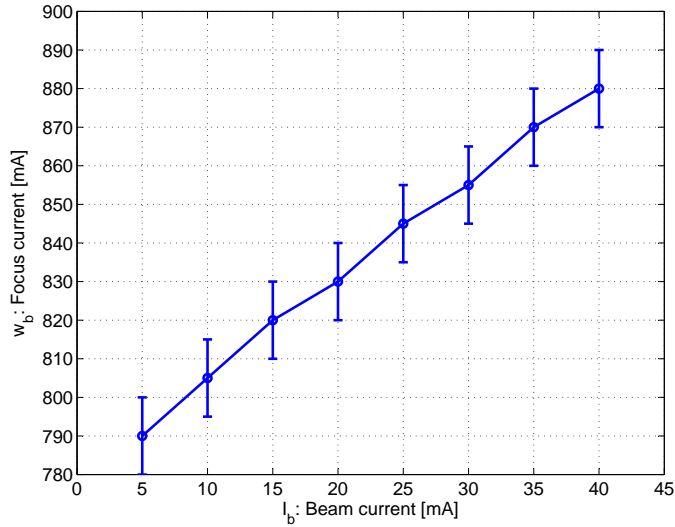
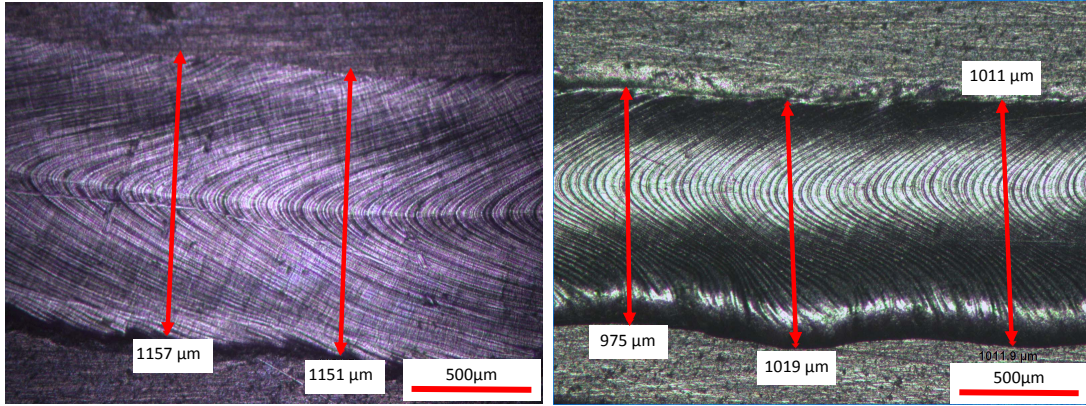


Figure 3–10: Focus current at 60kV with L1 = 55%

Another method used to examine beam focus is to perform bead-on-plate welds for a series of w_b values and then examine the solidified target region. According to Fig. 3–10, at $I_b = 10\text{mA}$, the optimal focus coil current is 810 mA. An image of the solidified weld region using this w_b value is shown in Fig. 3–11a.

Surprisingly, it was found that the optimal w_b is pulse length dependent for pulses less than 1 mS. As an example, the solidified weld region for a 10mA/60kV beam pulsed at $250\mu\text{S}/50\%$ duty at $w_b = 860\text{mA}$ is given in Fig. 3–11b. A Continuous Wave (CW) beam at this focus setting does not reach the energy density necessary to melt the stainless steel.

Considering the beam speed of 6 cm s^{-1} and the pulse length of $250\mu\text{S}$, the expected beam sweep length is $15\mu\text{m}$ ($v * t$). Considering the 50% duty cycle, the expected separation between pulse tails is $30\mu\text{m}$. A magnified image of Fig 3–11b,



(a) Continuous beam at $w_b = 810\text{mA}$ (b) $\tau = 250\mu\text{S}/50\%$ duty at $w_b = 860\text{mA}$

Figure 3-11: Optical micrograph of solidified welds as a function of focus current and pulse length. The beam scan speed was 6 cm s^{-1} with $I_b = 10\text{mA}$ and $U_b = 60\text{kV}$

shown in Fig. 3-12, demonstrates that this value is accurate considering heat transfer effects such as convection and solidification.

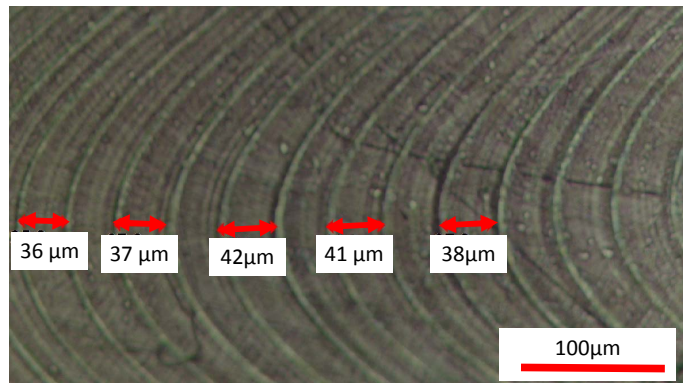


Figure 3-12: Optical micrograph of solidified laps during pulsed beam operation with $10\text{mA}/60\text{kV}$, $w_b = 860\text{mA}$ and $\tau = 250\mu\text{s}/50\%$ duty

At this point, the pulse length dependency of optimal focus is not understood. Possibilities include the space-charge effects of electron bunches, electromagnetic wake fields, transit-time effects, capacitance between the bias cap and cathode,

or some combination of the above. Further investigation was not pursued in lieu of experiments focussing on evaporation. Also, since a new gun was installed in November 2013, a thorough investigation was postponed. Future work should examine the interplay between accelerating voltage, beam current, focus current, pulse length and duty cycle with the objective of teasing out the mechanisms which make the focal length pulse dependent.

Electron Beam geometry

The focus coil manipulates the focal plane relative to the Working Distance (WD). In the current configuration, the distance between the target and the focus coil is 609 mm. Other relevant geometrical parameters of the current PAVAC setup are shown in Fig. 3–13.

Fig. 3–13 defines the beam axis $[u, v]$ as well as the target axes $[x, y]$. The beam current density is assumed to have a Gaussian distribution due to the Maxwellian velocity distribution of the emitted electrons. [15] Thus, along the beam axis, the power density will assume the following form:

$$f(u, v) = \frac{U_b I_b}{2\pi\sigma_v\sigma_u} * \exp\left(-\left[\frac{u^2}{2\sigma_u^2} + \frac{v^2}{2\sigma_v^2}\right]\right) \quad (3.5)$$

where $f(u, v)$ has units of $[\text{W m}^{-2}]$ and $\int_{-\infty}^{\infty} \int_{-\infty}^{\infty} f(u, v) dudv = U_b * I_b$. The extent of beam spreading is defined according to $\sigma_i[\text{m}]$, with a corresponding Full Width Half Maximum (FWHM) of $2\sqrt{2\ln 2}\sigma_i \approx 2.355\sigma_i$. Therefore, the beam energy density is defined according to σ_i .

The energy density in the $[x, y]$ plane will take a similar form to to Eq. 3.5. The beam projection onto the y axis will be unaffected, thus $\sigma_u = \sigma_y$. But since

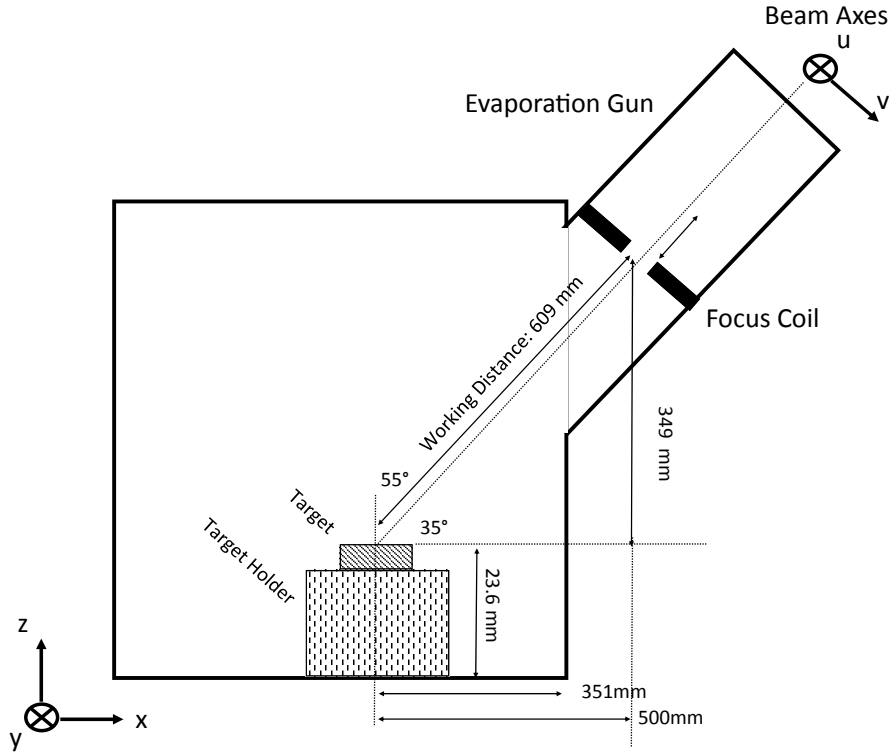
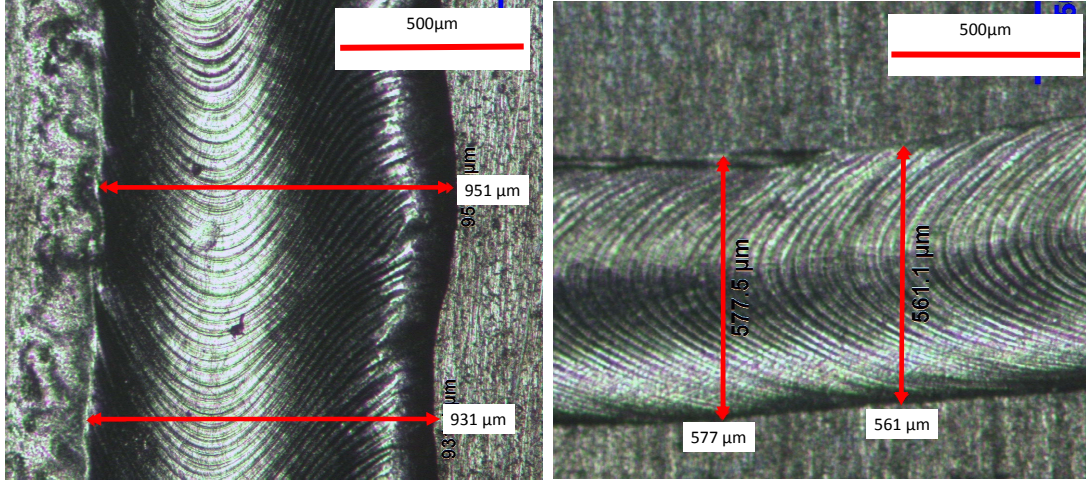


Figure 3–13: PAVAC chamber geometry. The chamber axes are defined in the lower left hand corner, with the positive y-axis going into the page. The beam axes are defined in the upper right corner

the beam is inclined 55° from the z axis, the beam will be elongated along the x direction, resulting in $\sigma_x = \sigma_v \cdot \cos(55^\circ)^{-1} \approx 1.74\sigma_v$.

The ellipsoidal beam spot can be observed experimentally by examining the solidified regions during pulsed melting. As discussed, $250\mu\text{s}$ pulses at $w_b=860\text{mA}$ and $60\text{kV}/10\text{mA}$ were single pass scanned in a circular pattern onto a stainless steel target. The resulting re-solidified regions are shown in Fig. 3–14.

From Fig. 3–14a, we see that the width of the melted region is approximately $950\mu\text{m}$, which is a function of σ_x . Similarly, Fig. 3–14b gives a melted region of



(a) Beam Moving along y direction

(b) Beam Moving along x direction

Figure 3–14: Optical micrograph of solidified welds using a scan speed of 6 cm s^{-1} with $\tau=250\mu\text{s}$ with $w_b=860\text{mA}$ at $60\text{kV}/10\text{mA}$

$575\mu\text{m}$ which is a function of σ_y . The ratio of these widths gives 1.65, which is close to the calculated ratio of 1.72, assuming $\sigma_u = \sigma_v$. Deviations are most likely due to variable working distance and astigmatism.

Assuming that the width of the melted regions of Fig. 3–14 represent the beam FWHM, σ_x and σ_y can be calculated, and for the beam parameters given (10mA/60kV), the estimated energy distribution is:

$$f(x, y) = 9.7 * 10^8 * \exp\left(-\left[\frac{x^2}{3.2 * 10^{-7}} + \frac{y^2}{1.3 * 10^{-7}}\right]\right) [Wm^{-2}] \quad (3.6)$$

A 2D shaded plot demonstrating the energy distribution estimation of Eq. 3.6 is shown in Fig. 3–15. The values used to generate this plot (σ_x, σ_y) should be thoroughly validated using inverse modelling of the heat transfer as well as Faraday cup tomography. [23]

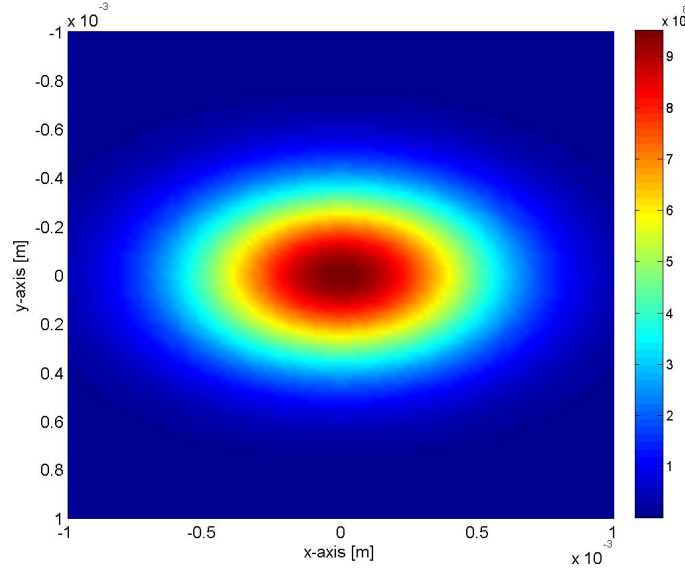


Figure 3–15: Shaded plot of beam projection according to Eq. 3.6

As the beam is rastered over the target, the geometry of Fig. 3–13 shows that the Working Distance (WD) will change as a function of position. Using the axes defined in Fig. 3–13, a translation of Δx [cm] at the target results in a new WD_x' [cm] of:

$$WD'_x = \sqrt{(50 - \Delta x)^2 + 34.9^2} \quad (3.7)$$

Similarly, a translation of Δy results in a modified working distance, WD_y' of:

$$WD'_y = 60.9 * \sqrt{1 + (\Delta y/60.9)^2} \quad (3.8)$$

A plot of the change in WD is given in Fig. 3–16, showing a pronounced effect along the x axis. Future bead-on-plate experiments should account for this effect when determining optimal focus.

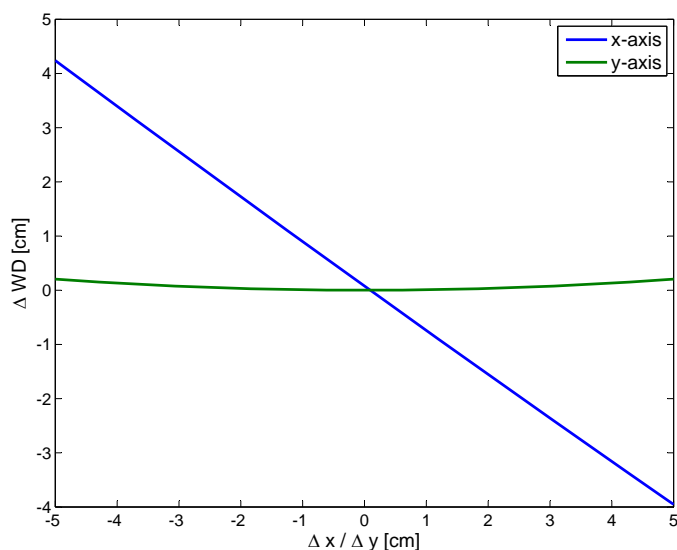


Figure 3–16: Effect of translation on work distance for current chamber geometry

3.2.4 Deflection Coils

The above section focused on defining and understanding the power density of the beam spot. The importance of this parameter in conventional and pulsed EB-PVD is apparent when recognizing that the target temperature increase depends on the energy absorbed during beam impingement, which is the product of power density and dwell time, τ . In conventional CW processing, the dwell time is the quotient of spot size over velocity. In pulsed processing, the dwell time and pulse length are equivalent. As an example, FEM simulations of the molten Ti surface temperature as a function of beam speed is shown in Fig. 3–17.

The difference in the temperature contours of Fig. 3–17 are a result of the energy deposited as well as solutions to the heat conduction and the Navier-Stokes

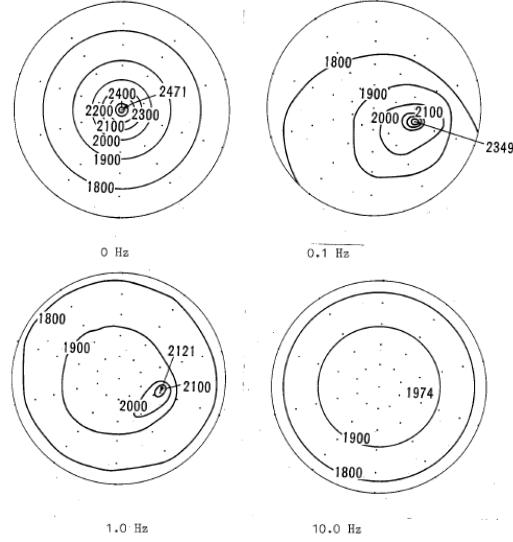


Figure 3-17: Effect of beam deflection on temperature profile of Ti surface. [24]
The beam is scanned in a circular pattern of fixed radius, therefore the frequency is proportional to the beam speed

equation.[24] Since the evaporation rate is defined by surface temperature, Fig. 3-17 demonstrates that beam velocity is a critical processing parameter during EB-PVD.

Beam deflection is achieved by generating a homogeneous \mathbf{B} field normal to the beam axis, resulting in a Lorentz force according to Eq. 3.3. For 2-axis deflection at the work plane, the PAVAC machine uses crossed dipole magnets that deflect the beam by adjusting the current in each element. The beam is deflected in the beam axis plane, $[u, v]$, which is then projected onto the $[x, y]$ working plane. The deflection angle, ϕ is defined according to:

$$\sin(\phi) = k \frac{B}{U_r^{1/2}} \quad (3.9)$$

where k is a function of the coil design, B is the magnetic field strength and U_r is the relativistically corrected accelerating voltage. The deflection pattern is determined by the amplifier/coil/magnetic coupling circuit shown in Fig. 3–18.

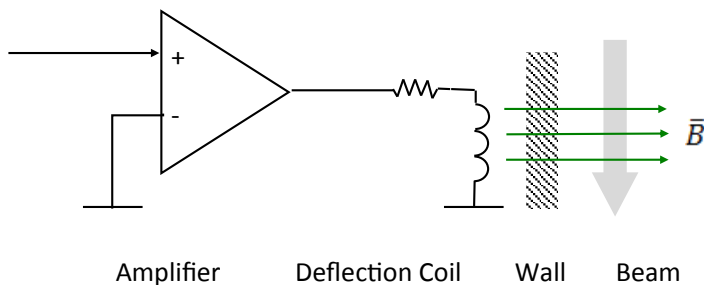


Figure 3–18: Electrical and magnetic circuit used for beam deflection

Fig. 3–18 shows that the deflection pattern is generated according to the current driven into the magnetic windings. In order to estimate these circuit parameters, an experiment was undertaken whereby a sine wave of known frequency was used to drive the coils. The amplitude of the sine wave [V] was adjusted at each frequency such that the length of the deflection pattern matched to a pre-defined length at the target. Therefore, we obtain a value of length per volt at each frequency, with the results shown in Fig. 3–19.

As expected, the circuit of Fig. 3–18 behaves like a low pass filter. Therefore, a fit was performed in order to determine DC gain, κ [cm V⁻¹] and cut off frequency, f_c [Hz]. The fitting function is the amplitude response of an amplified, single pole low pass filter:

$$|H(f)| = \frac{\kappa}{\sqrt{1 + (f/f_c)^2}} \quad (3.10)$$

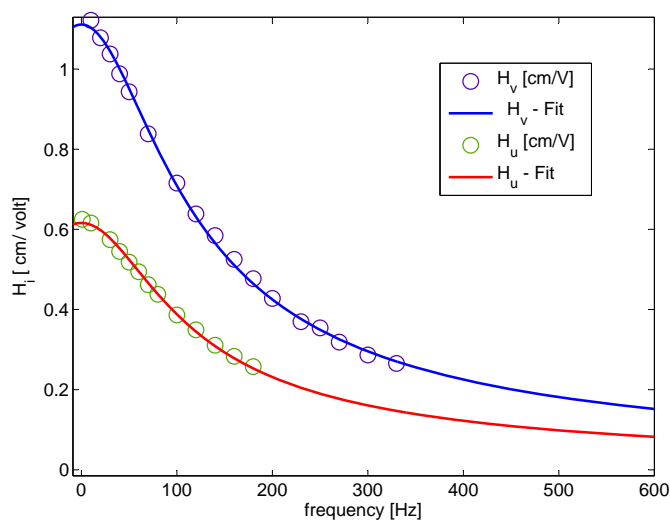


Figure 3–19: Deflection coil transfer function

The resulting fit parameters are shown in Table 3–2, which are good when considering the χ^2 values and fit curve of Fig. 3–19.

	κ [cm/V]	f_c [Hz]	χ^2
H_v	1.11	83	0.9988
H_u	0.61	81	0.9983

Table 3–2: Fit parameters of Eq. 3.10 for data shown in Fig. 3–19

Returning to Eq. 3.10, we see that when the coils are driven at frequencies near f_c , the deflection pattern will be compressed. The frequency dependent phase lag, which is a outcome of the low-pass transfer function, will distort the deflection shape. This phase distortion is especially apparent when using signals which have high harmonic content, ie square waves.

In order to utilize the results of Table 3–2, a deflection coil emulator was developed in MATLAB[®] to assist in defining the drive signals. For deflection,

the user defines the signal type (sine, triangle, sawtooth, square), phase offset, signal amplitude (-10:10 V), signal frequency (1:1000Hz) and DC offset (-10:10 V). The resulting signal drives the amplifier, which energizes the deflection coils and deflects the beam. An equivalent flow diagram of the circuit is shown in Fig. 3–20, where $[u, v]$ represent drive signal and $[x(t), y(t)]$ is the time-dependent beam position.

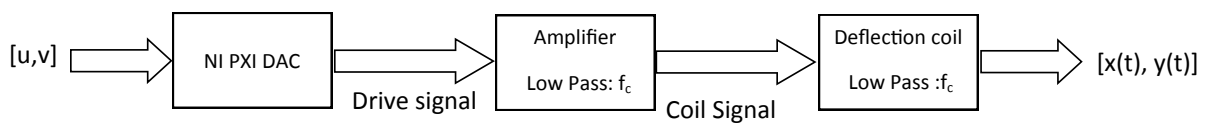


Figure 3–20: Flow diagram of deflection coil subsystem

Assuming the deflection coils are not inductively or capacitively coupled, we can model the deflection pattern transfer function using the MATLAB[®] functions `butter` and `filter`. Since the highest operating frequency is 1 kHz, the amplifier cut-off is assumed to be 2 kHz, while the coil parameters are given in Table 3–2. Thus, the MATLAB emulator generates the true deflection pattern at the work plane for a given set of $[u, v]$ parameters.

As an extreme example, consider the $[u, v]$ parameters given in Table 3–3. These signals are considered extreme since the driving frequency is far above cut-off and square waves have a large amount of harmonic content which will be suppressed by the inductor.

The idealized ($H(f)=1 \text{ cm V}^{-1}$) and true deflection patterns are shown in Fig. 3–21. These patterns clearly demonstrate the difference between the idealized and true deflection patterns incurred by the coil inductance.

Axis	u	v
Type	Square	Square
Amplitude [V]	2	5
Phase [°]	0	90
f [Hz]	500	500

Table 3–3: Simulated deflection coil signals

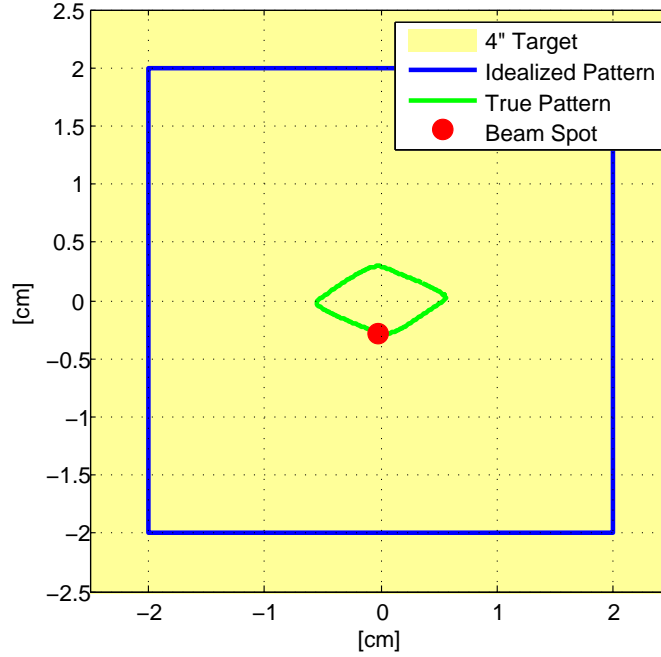


Figure 3–21: Deflection distortion for $[u, v]$ signal defined in Table 3–3. The simulation shown is after 10 cycles, thus settling any transients

As expected, the output of the magnetic windings (ie \mathbf{B} field) is smoothed and compressed compared to the idealized form. Fig. 3–21 also shows the expected 90° rotation due to the single pole low pass filter being above cut-off. Since the code calculates the position of the beam as a function of time, the pattern of Fig. 3–21 has been animated to assist in visualization. Most importantly, the emulator calculates the beam speed, with the results shown in Fig. 3–22.

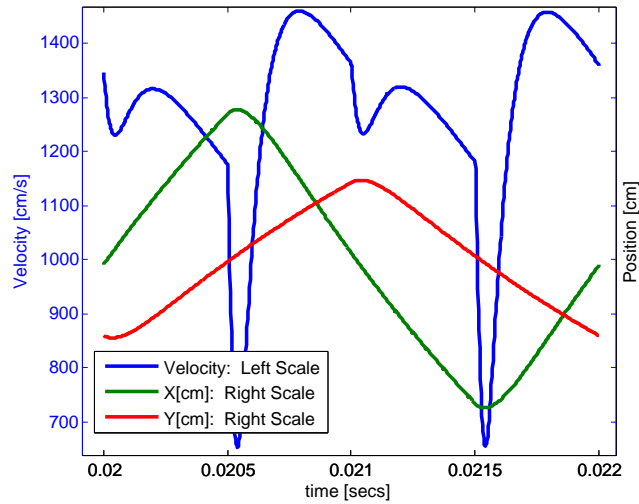


Figure 3–22: Beam spot position and velocity for $[u, v]$ parameters of Table 3–3

During a change in the x direction, Fig. 3–22 shows the beam slowing down. As discussed at the beginning, this reduced speed will result in a great deal of local heating. Physically, speed reduction occurs because of dissipation of stored magnetic energy in the coil, which cannot occur instantaneously.

Beam pattern distortion similar to Fig. 3–21 has been observed experimentally. The size and shape of the re-solidified regions have been examined, and match the predicted pattern very well. Therefore, the deflection coil emulator is an invaluable tool for analysing and modifying a given set of deflection patterns.

Deflection speed and heat deposition

Although it is obvious that the beam speed and spot size will define the energy deposition, a thorough consideration of the geometry shows that the energy deposition is in fact velocity dependent. As an example, consider the point $[0,0]$

in the $[x, y]$ plane which is scanned along the beam center line with velocity v_x .

Manipulation of Eq. 3.5 yields:

$$f(0, 0) = \frac{U_b I_b}{2\pi\sigma_x\sigma_y} * \exp\left(-\left[\frac{[v_x * (t - t_0)]^2}{2\sigma_x^2}\right]\right) \quad (3.11)$$

where t_0 represents the time when the beam is centered on $[0,0]$. In this case, the FWHM is $2.355\sigma_x/v_x$, which has units of time, and represents a more exact definition of dwell time. The total energy deposited at $[0,0]$ then becomes

$$\int_{-\infty}^{\infty} \frac{U_b I_b}{2\pi\sigma_x\sigma_y} * \exp\left(-\left[\frac{[v_x * (t - t_0)]^2}{2\sigma_x^2}\right]\right) dt = \frac{U_b I_b}{\sqrt{2\pi} * \sigma_y v_x} \quad (3.12)$$

which has units of energy flux, $[J m^{-2}]$. Eq. 3.12 demonstrates that energy deposited at any given point will decrease with increasing beam speed.

Similar results will be obtained for a beam scanned in the v_y direction.

Assuming that the power distribution along the beam axis is uniform ($\sigma_u = \sigma_v$), the geometry of Fig. 3-13 dictates that $\sigma_x = 1.74\sigma_y$. Therefore, for identical velocities ($v_x = v_y$), we expect a 42% reduction in energy flux when traversing in the v_y direction compared to the v_x direction. Similarly, we expect a 74% increase in dwell time when traversing in the x direction compared to the y direction. This result shows that the energy deposition rate is a function of the beam speed and direction, ie velocity. This can have important implications for evaporation, as will be seen when examining oxide evaporation in Section 5.3.4.

3.3 PAVAC Electronics

Having described the electrical and magnetic elements along the electron beam axis, a brief discussion of the electronic systems will be given.

3.3.1 High Voltage Power Supplies

Specially designed High Voltage Power Supply (HVPS) are essential components of any electron beam system. The HVPS must fulfill the following requirements:

1. The beam position must remain static in the fixed magnetic field, ie low voltage ripple
2. Protect the e^- beam gun during arcing
3. Control the current delivered to the heated cathode

From a reliability and safety perspective, the possibility of arcing is a major concern. If the gun chamber pressure of the PAVAC gun exceeds $\approx 5 \cdot 10^{-3}$ mbar, gas ionization will short the anode and cathode. If the arc is not extinguished rapidly, either the HVPS or the electrodes will fail. Therefore, the HVPS must have a current detection and suppression mechanism in place for safe operation. [14]

3.3.2 Control System Architecture

In the PAVAC machine, a centralized Real-Time Operating System (RTOS) controls the entire EB-PVD process. Once energized, the RTOS places the entire system in a known, passive state. After the user PC is powered and the executable is run, a connection is established between the RTOS engine and the graphical user interface.

The RTOS represents a separate computer, which accepts inputs and defines outputs according to the code loaded into memory. Inputs may include machine values (current sample vector $[Lb]$) as well as user commands (set $I_b = 5\text{mA}$). The

advantage of this architecture is deterministic processing on a dedicated processor. As an example, if the user PC slows(program loading) or crashes, the RTOS is unaffected. Understanding this operating premise can greatly assist in debugging and modifying system parameters.

CHAPTER 4 Electron Beam Heating

4.1 Electron/Matter Interactions

Regardless of application, electron beams interact with matter according to a set of well-understood parameters. For our purposes, the electron beam represents a focused heat source with parasitic effects such as backscatter electrons and x-rays. In some instances, electron beams are chosen specifically for these secondary effects, with heat being the undesired by-product. Considering the fundamental nature electron/matter interactions with regards to EB-PVD, a brief description of the phenomenon will be given.

Whether travelling through a rarefied or dense medium, electrons will interact with matter via discrete scattering events. The average distance between scattering events is defined by the electron mean free path:

$$\lambda = \frac{1}{n\sigma} \tag{4.1}$$

where λ [cm] is the mean free path, n is the density [molecules cm^{-3}] and σ is the scattering cross section [cm^2]. The mean free path, λ determines the number of electrons, N , which have not collided in a transit distance x , according to: [21]

$$N = N_o e^{-x/\lambda} \tag{4.2}$$

Eq. 4.2 demonstrates the importance of a vacuum during electron beam processes: the mean free path must be longer than the working distance for beam transmission. As electrons transition from vacuum (10^{-5} mbar) to solid matter, the density changes by approximately 10^{11} , with a corresponding decrease in λ .

Fundamentally, the negatively charged electrons interact with matter via the Coulomb potential surrounding the atom or molecule. The brief interaction result in one of two possible scattering events. Elastic scattering occurs as the free electron interacts with the positively charged nucleus, resulting in negligible energy exchange and a large electron recoil deflection. Inelastic scattering occurs as the free electron interacts with the negatively charged electron cloud, resulting in energy exchange between particles with negligible deflection. Thus, the total cross section will include both events:

$$\sigma = \sigma_{elas} + \sigma_{inelas} \tag{4.3}$$

where σ_i is a function of the electron energy as well as the medium. For the purposes of EB-PVD, we are interested in heat generation via inelastic scattering, but Eq. 4.3 demonstrates that both events occur simultaneously. As will be shown, the interplay between these combined events has significant implications on the depth of interaction as well as secondary losses such as Back-Scattered Electrons (BSE).

4.2 Electron Beam Transit

Immediately after free electrons are emitted from the cathode, they are capable of interacting with the rarefied gas medium. Although the expected number of

collisions is low, gas/electron interactions can have significant implications on the process parameters. In some instances, a high number of collisions are desired in order to enhance the chemical reactions at the substrate (i.e. plasma processes). In other cases, collisions will be detrimental or even catastrophic to the electron beam hardware. Thus, a brief discussion regarding the electron beam in the vacuum will be given.

4.2.1 Elastic Collisions: Transit Losses

Electrons are emitted from the cathode and accelerated within the electric field generated between the anode and cathode. Some electrons will have an emission angle which prevents passage through the anode aperture. Other electrons will elastically collide with residual molecules within the chamber, resulting in a large deflection angle. In both cases, these electrons are considered lost with respect to electron beam heating, despite registering as current delivered by the High Voltage Power Supply (HVPS).

Under ideal conditions, the transit losses have been measured to be less than 1% in the PAVAC electron beam gun. [25] As the pressure increases or the voltage decreases, the probability of elastic collision increases. But considering the significantly larger losses that will be considered, the transit losses will be neglected assuming the acceleration voltage is high ($U_b \geq 60\text{kV}$) and the pressure is low ($P_{chamber}, P_{gun} \leq 1\text{E-}4$ mbar)

In some applications, water cooled constrictions are introduced along the beam path in order to decouple the gun and process vacuums. The water temperature of the constriction is monitored as a process parameter, as it gives an indication of the transit losses and beam focusing.[26]

4.2.2 Inelastic Collisions: Ionization

For the purposes of transporting beam power, inelastic collision losses are a negligible fraction of the total beam energy, even in the relatively poor vacuums used during electron beam melting. [27] If the electron undergoes numerous inelastic collisions, the energy lost to each collision ($\sim 10\text{eV}$) is negligible compared to the net energy ($\sim 10\text{s keV}$). Also, the cross section for inelastic collisions is small considering the high accelerating voltages used ($\geq 60\text{kV}$), as shown in Fig. 4-1.

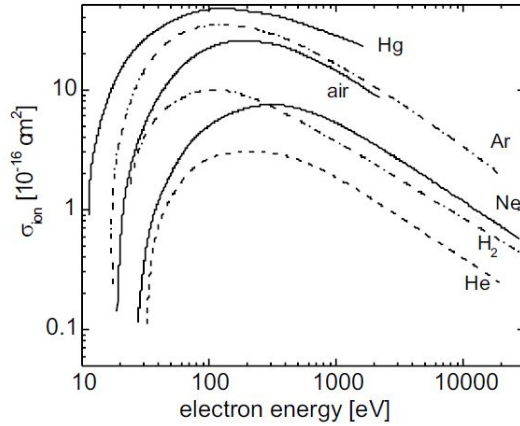


Figure 4-1: Cross section for inelastic collision by electron impact for various gases. [28]

During inelastic collisions, internal energy levels of the atom are excited. For electron impact with a gas, the most important reactions are: [28]

- Excitation: $e^- + A_2 \rightarrow e^- + A_2^*$
- Dissociation : $e^- + A_2 \rightarrow e^- + 2A^*$
- Ionization: $e^- + A_2 \rightarrow 2e^- + A_2^+$

Variations of the gas/electron reactions exist depending on the nature and complexity of the gas molecules, i.e. Ar vs NH_3 . The metal vapour generated near the beam spot is also subject to these processes. For electrons, the ionization cross section is zero for energies below the ionization energy, and peaks at ~ 2 -5 times the ionization energy, and then decreases hyperbolically. Roughly, metals have a ionization energy between 5-10 eV, while gas has a ionization energy between 10-25 eV.

For each process, an energy-dependent cross section can be defined for each possible inelastic reaction. For example, the individual contributions of the total scattering cross section of O_2 is shown in Fig. 4-2.

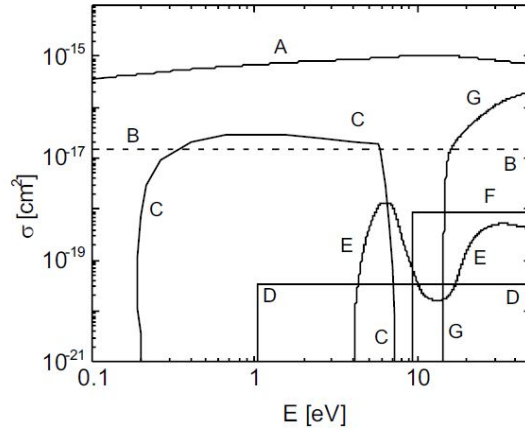


Figure 4-2: Individual contributions of the scattering cross section for electronic impact of O_2 . The letters denote the contributions as follows: A: elastic scattering, B: rotatory excitation, C: oscillatory excitation, D: excitation to singlet-oxygen, E: dissociative attachment F: excitation to upper electronic states, G: ionization. [28]

Inelastic collisions result in the characteristic radiation (excitation), highly reactive species (dissociation), and positively charged ions (ionization). Despite the negligible power loss, the positively charged ions can have a considerable influence on the beam focus, especially if a process gas is admitted into the vacuum chamber (ie reactive evaporation) or at high evaporation rates, which result in high local vapour density and large Secondary Electrons (SE) currents.

When formed, positive ions move towards the beam axis, which represents a region of lower electric potential. Consequently, these ions compensate for some of the negative intrinsic space charge of the electron beam and effectively focus the beam. Thus, the degree of gas focusing will depend on the number of ions formed. As shown in Eq. 4.3, elastic collisions will increase along with ion current, eventually reaching a point whereby the beam defocuses. [29, 30] Thus, gas can have the simultaneous effect of broadening the beam (elastic collisions) and focusing the beam (inelastic collisions), depending on the energy, species and densities involved. [15]

Gas focusing is especially important when evaporating ceramics, as a large number of ions can be formed due to the retarding effect of the charged insulator, and the higher ionization potential of the vaporized anion. This can result in a runaway condition called beam tunneling, whereby gas focusing results in increased evaporation rates, which results in increased ion formation which increases gas focusing. [31] It is imperative that the beam is rastered during ceramic evaporation.

Ionization & Electron Beam Guns

Ionization has important implications for the operation of electron beam guns. As electrons are emitted from the cathode, they are accelerated from 0 to U_b , passing through the peak ionization cross section. This results in the formation of ions within the accelerating field. Because of their positive charge, ions will be accelerated *towards* the cathode, imparting kinetic energy from the field to the cathode in a process called sputtering. As discussed, sputtering destroys the emitting surface and has negative consequences on the beam parameters.[15]

A much more catastrophic possibility for ions is the formation of an arc discharge between the cathode and anode. As ions impact the cathode, additional electrons will be emitted because of the increased surface temperature as well as secondary electron emission. The increased electron current will increase the ion current, resulting in runaway heating of the cathode in a process called arc discharges. As mentioned in Chapter 2, arcs are extinguished by an appropriately designed High Voltage Power Supply (HVPS).

4.3 Backscatter and Secondary Electrons

As electrons enter a solid, the concept of in/elastic scattering remains unchanged despite the drastic increase in density. Also, as the evaporant transitions from solid to vapour, the scattering cross section for electrons does not change as it does for photons, demonstrating another distinction between electron beams and lasers. [32]

Electrons will undergo many scattering events, and the interplay between elastic and inelastic collisions defines the profile and amount of heat deposition.

Specifically, as energy is lost to inelastic collisions, the probability of elastic scattering increases faster than inelastic scattering according to: [22]

$$\frac{\sigma_{inelas}}{\sigma_{elas}} = \frac{20}{Z} \quad (4.4)$$

where Z is the atomic number. This demonstrates that the depth and the shape of the heating volume is a strong function of atomic number. Specifically, with increasing Z , the depth of interaction volume decreases, and the shape transitions from a pear to a hemispherical shape. In our experiments, the beam spot size is larger than the depth of interaction, thus shape effects should not be significant.

Back-Scattered Electrons (BSE) enter the material and undergo a series of elastic scattering events, which direct the electron *out* of the target surface. These electrons can leave with a significant fraction of their incident energy, and represent a major loss of heating power, sometimes in excess of 50% of the incident beam power. [15]

Secondary Electrons (SE) are loosely bound outer shell electrons which are kicked out of the solid due to the inelastic energy transfer. SE are only emitted within a few nanometers of the target surface. SE will not be discussed any further as they form a small portion of the net power loss (< 1%). It is worth noting that these low energy electrons are important when considering ionization as they have a high ionization cross section. Roughly, SE are defined as having energy less than 50eV, while BSE have energies from 50eV up to eU_b .

The fact that BSE and SE are emitted from the target suggests that any ungrounded surface within the chamber can become charged, including non-conductive coatings. The isolated charge will create an electric field which can disturb the beam focus. When possible, components installed within the vacuum chamber should be conductive and grounded.

4.3.1 BSE Losses & CASINO

Considering that electron collisions are discrete, probabilistic events, the Monte Carlo method is well suited for simulating electron/matter interactions. Specifically, the software CASINO (monte CARlo SIMulation of electroN trajectory in sOlids), written by McGill professor Raynald Gauvin, was designed to calculate the electron beam interactions encountered during electron microscopy. [33] In our application, the software is only used to calculate the BSE losses but it can also calculate the interaction volume for a given set of electron beam parameters.

When calculating the power loss due to backscattered electrons, the initial assumption is to examine the BSE current, according to:

$$\eta_{BSE} = \frac{I_{BSE}}{I_b} \quad (4.5)$$

Unfortunately, this number does not accurately capture the BSE power, as the BSE will exit with a spectrum of energies. An example of the BSE energy spectrum calculated in CASINO is shown in Fig 4-3.

From the perspective of power transfer, η_{BSE} will be an overestimate since the tail distribution (low eV) represents electrons which have transferred a large

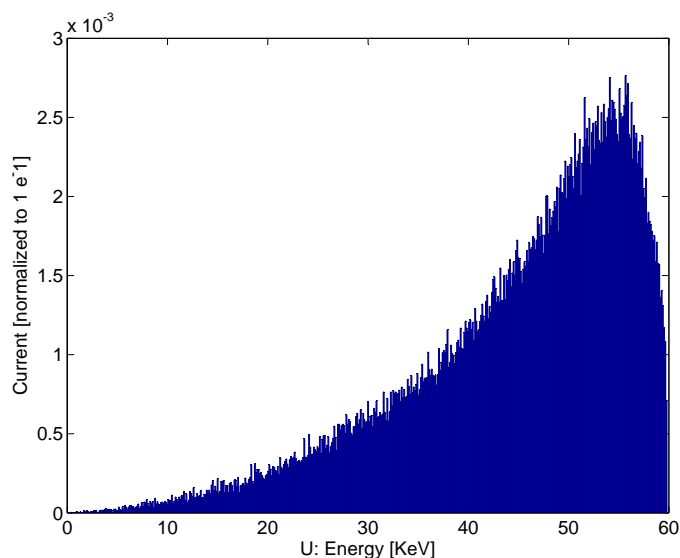


Figure 4-3: Normalized backscattered electron energy distribution for nickel calculated using 250,000 electrons in CASINO at 60kV and 55° incidence

portion of their energy to the target. Thus, the true power loss due to BSE is calculated according to:

$$\eta_{power} = \frac{\int_0^{U_b} U * I_{BSE}(U) dU}{U_b * I_b} \quad (4.6)$$

In the case of the normalized ($I_b = 1e^-$), discrete data produced by CASINO, η_{power} approximates to:

$$\eta_{power} = \frac{\sum_i \langle hits_{BSE} \rangle * U_{BSE}}{U_b} \quad (4.7)$$

where $\langle hits_{BSE} \rangle$ is the fraction of electrons leaving the target with energy U_{BSE} . As an example, for a Ni target struck with a 60kV e^- beam at a 55° incidence angle, $\eta_{BSE} = 0.435$ while $\eta_{power} = 0.327$, a difference of nearly 25%.

Thus, the net power delivered to the target minus the BSE losses becomes:

$$Q_{target} = (1 - \eta_{power})I_bU_b \quad (4.8)$$

where Q_{target} represents the beam power which is transformed into evaporation, x-rays, conduction, radiation, etc.

Considering the flexibility of CASINO, these calculations can be rapidly performed for multi-layered or porous targets, as well as compounds and alloys. It should also be possible to use this software to determine matter/beam interactions of metallic powders.

CASINO Convergence

Considering the statistical nature of CASINO, sufficient electron trajectories are needed in order to converge upon an accurate solution. As Fig. 4–4 demonstrates, 200,000 electrons accurately captures η_{power} .

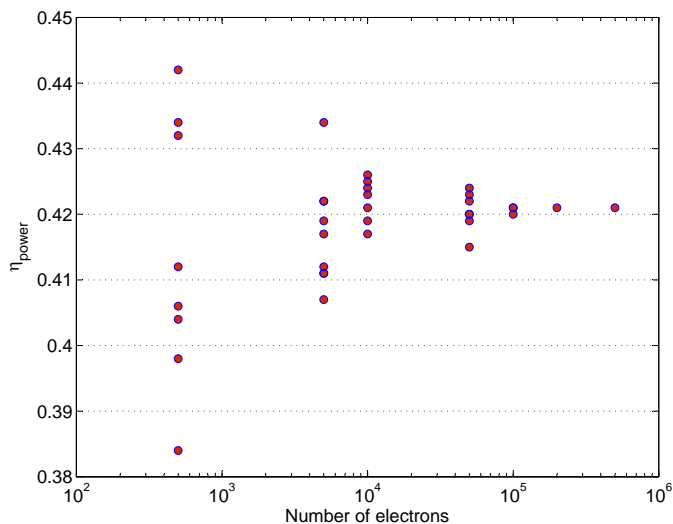


Figure 4–4: Convergence of η_{power} for e^- beam incident on Ni at 60kV with $\theta = 55^\circ$

4.3.2 Electron Beam Heat deposition

The interplay between in/elastic collisions will define the depth and profile of the electron beam heat deposition. The depth of interaction, referred to as the electron range S [cm], is given by:

$$S \approx 2.1 * 10^{-12} \frac{U_b^2}{\rho} \cos(\theta) \quad (4.9)$$

where U_b [V] is the accelerating voltage, ρ [g cm⁻³] is the density and θ [°] is the angle between the surface normal and the e⁻beam. More advanced equations for the electron range (e.g. the Kanaya-Okayama equation), are within 15% of Eq. 4.9.[22]

Assuming the beam cross section, σ is larger than S , the 1^D heat deposition profile, $P_b(z)$ can be written in a normalized form according to: [15]

$$P(z) = P_o \left(1 - \frac{9}{4} \left(\frac{z}{S} - \frac{1}{3} \right)^2 \right) \quad (4.10)$$

where $P_o = 1.6(1 - \eta_{power})U_b J_b$ [W m⁻²] is the incident power flux minus BSE losses. Fig 4-5a is a plot of Eq. 4.10, which demonstrates that $P_b(z)$ peaks at $z = S/3$ and thus S represents the length scale in which heat is deposited within the material. The electron range S is plotted for different materials in Fig 4-5b and is shown to be within 500nm-100 μ m for all practical materials using an accelerating voltage of 20-80kV.

The profile shown in Fig 4-5a should be contrasted to the heating profile achieved during laser irradiation, which goes as $I_o e^{-z/\alpha}$, where α is the material

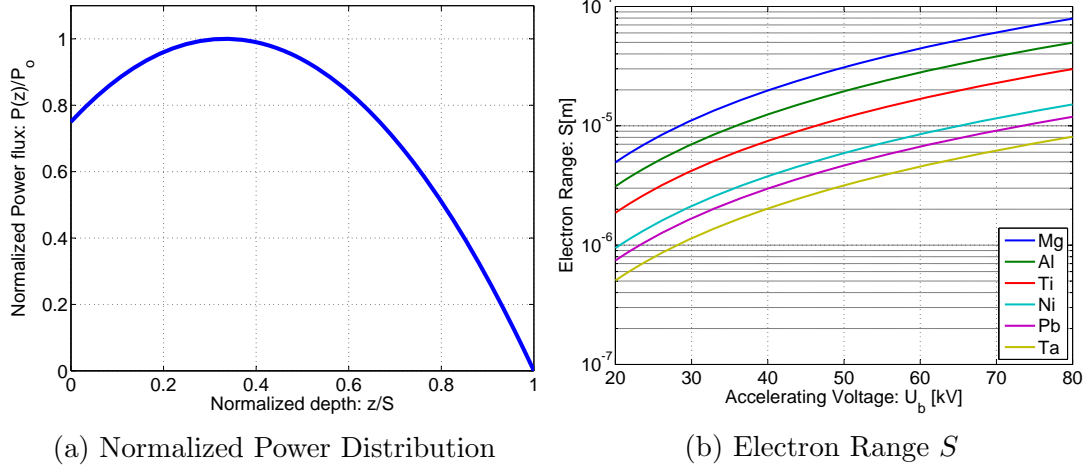


Figure 4-5: Power distribution and electron Range as defined in Schiller [15]

dependent optical absorption length. Roughly, α is in the 10s nm range [34], thus electron beams will tend to have deeper heat distribution compared to lasers.

Heat Profile and CASINO

If the beam cross section is comparable to the electron range, a full 3^D model of the heat deposition profile is required. Simulations of these profiles are possible using the CASINO software. Fig. 4-6 shows the calculated heat deposition profile for a $50\mu\text{m}$ beam at 55° projected onto the XZ plane.

4.4 X-Ray Generation

As the electron beam interacts with the solid target, biologically harmful x-rays are generated. The fraction of beam power converted into x-ray power is given by: [15]

$$Q_x \approx Q_o * 10^{-9} U_b Z \quad (4.11)$$

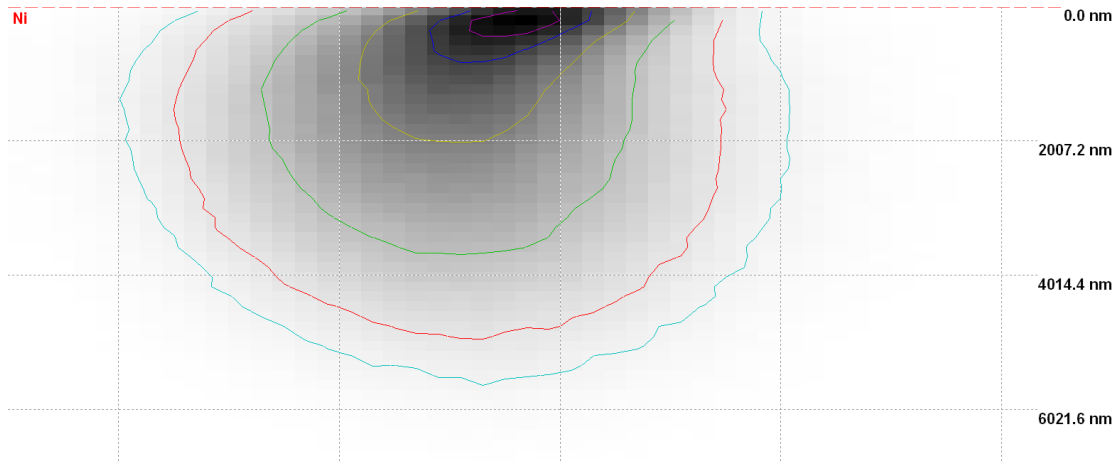


Figure 4-6: Simulated heat deposition profile generated in CASINO using a $50\mu\text{m}$ beam on Ni at 60kV with $\theta = 55^\circ$ projected onto the XZ plane.

where $Q_o[\text{W}]$ is the incident power, $U_b[\text{V}]$ is the accelerating voltage and Z is the atomic number. In the worst case, energy losses at the work site are less than 1% and can be neglected for the purposes of thermal accounting. [15] But considering the operator proximity to the x-ray source, a short discussion regarding x-ray generation and shielding will be given.

Two types of x-rays will be emitted during electron impact: bremsstrahlung and characteristic x-rays. Bremsstrahlung, which is German for "braking radiation", is electromagnetic radiation produced by the deceleration of charged particles. Characteristic x-rays result from the ionization and relaxation of the inner electron shells of the target atoms, emitted at discrete wavelengths. A qualitative x-ray spectrum is given in Fig. 4-7.

Bremsstrahlung generates a broad spectrum of x-rays, which have a peak intensity at approximately 60% of the incident electron energy. The total

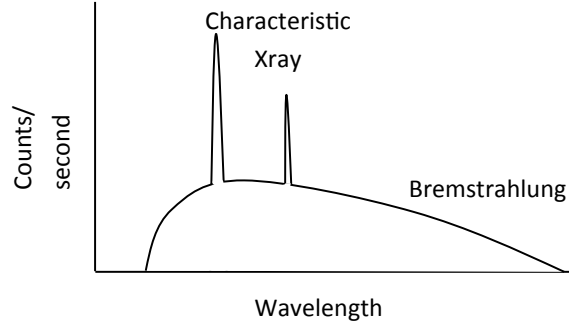


Figure 4-7: X-Ray spectrum generated during electron impact. Note that shorter wavelengths represent higher energies via the de Broglie equation

Bremsstrahlung power emitted goes as: [35]

$$P_{Bremsstrahlung} \propto A Z I_b U_b^2 \quad (4.12)$$

where A is a proportionality constant, Z is the atomic number, I_b is the beam current, U_b is the accelerating voltage.

Characteristic x-ray emission occurs at discrete ionization energies, referred to as K, L and M lines. The intensity of any characteristic line depends on the current and the voltage excess above the critical excitation voltage, V_{ion} . For the K line, the intensity is roughly: [35]

$$P_{k-line} \propto B I_b (U_b - V_k)^{3/2} \quad (4.13)$$

where B is a proportionality constant and V_k is the K-line excitation voltage.

The x-ray power is absorbed by the chamber walls according to the Beer-Lambert law $I = I_0 e^{-\mu x}$, where μ is the linear absorption coefficient. Usually, the attenuation of a material is stated as the mass absorption coefficient, μ/ρ , which is

independent on physical state, and defined as: [35]

$$\frac{\mu}{\rho} = k \lambda^3 Z^3 \propto \frac{Z^3}{U_b^3} \quad (4.14)$$

where λ is the wavelength.

Roughly, Eqs. 4.12-4.14 show that as the U_b increases, the $P_{Bremsstrahlung}$ intensity increases as the square of the voltage, P_{k-line} increases to the power of 1.5 and the x-ray absorption decreases to the power of -3. Thus for any new evaporation process (material, I_b , U_b), it is highly recommended that the x-ray dose is measured. If the dosage is found to be unacceptable, the simplest solution is to decrease the accelerating voltage.

Measurements of the PAVAC machine using a copper target have shown that the x-ray dose rate at 80 kV/15 mA was above the recommended 2.5 mRem h⁻¹. A reduced U_b of 60 kV/15 mA gave a reading below the resolution limit of the calibrated Technical Associates TBM-3 Geiger Counter. For perspective, the average annual x-ray dosage is 186 mRem year⁻¹ while the maximum allowable limit for nuclear energy workers is 10,000 mRem over 5 years.

4.5 Electron Beam Heating

Having described the fundamental e⁻beam interactions, which generate heat along with the parasitic power losses, the stage is set to examine the thermal response of the target as it pertains to evaporation. As will be shown, evaporation is defined by the surface temperature, which is a function of beam and thermo-physical material parameters. In a sense, the material and beam interactions are coupled to the evaporation rate via the heat equation. Thus, the generation

of vapour requires an understanding of how beam power is transformed into temperature in a process referred to as thermal accounting.

When the beam strikes the target material, beam power is transformed into a series of secondary phenomena which are graphically demonstrated in Fig. 4–8.

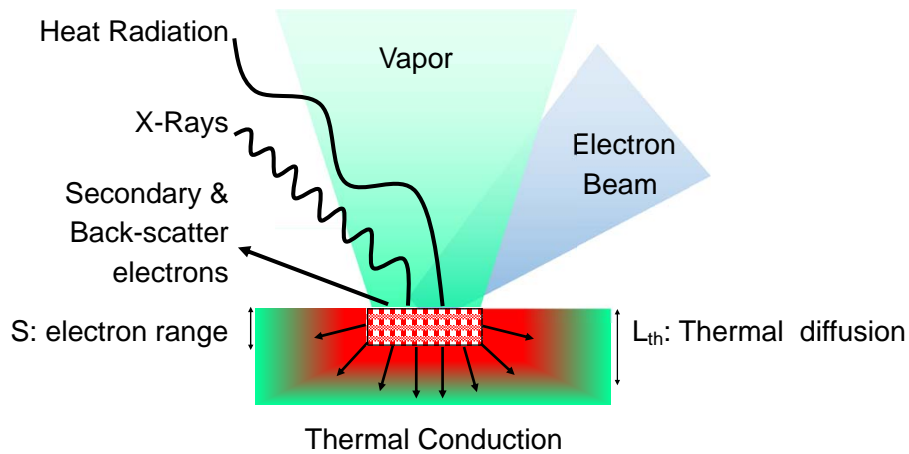


Figure 4–8: e^- beam/matter interaction with sources of energy loss[15]

Many of the phenomena shown in Fig. 4–8 have been described, and do not significantly factor into the thermal response of the material. Qualitatively, the e^- beam parameters are transformed according to:

$$Q_{HVPS} = Q_{trans} + Q_{x-ray} + Q_{BSE} + Q_{SE} + Q_{rad} + Q_{vap} + Q_{cond} \quad (4.15)$$

where

- Q_{HVPS} : Power delivered by High Voltage Power Supply (HVPS); $U_b * I$
- Q_{trans} : Beam transit losses; less than 1% under normal operating conditions
- Q_{x-ray} : X-ray generation; less than 1%, (Eq. 4.11),
- Q_{BSE} : BSE loss; material dependent, (Sec. 4.3.1)

- Q_{SE} : Secondary Electrons (SE) power loss; material dependent, negligible
- Q_{rad} : Radiative heating
- Q_{vap} : Latent heat of evaporation
- Q_{cond} : Thermal conduction

Neglecting the small beam losses (Q_{trans} , Q_{x-ray} , Q_{SE}) and incorporating the BSE losses into the incident heat, Eq. 4.15 can be redefined to examine the thermal response according to:

$$Q_{beam} = (1 - \eta_{power})Q_{HVPS} = Q_{rad} + Q_{vap} + Q_{cond} \quad (4.16)$$

Eq. 4.16 states that the power absorbed by the target is transferred out via BSE, radiation, conduction and vaporization. In the following sections, each heat loss mechanism will be briefly addressed, with the purpose of analysing the net e^- -beam heating process. It is important to remember that electron beam heating does not result in a steady state temperature profile, since the heat source itself is not stationary. Thus, understanding the interplay between spot size, power density and deflection pattern is critical for linking the local evaporation rate to the global thermal response.

Thermal Radiation

Thermal radiation is broad spectrum electromagnetic radiation generated by all matter above absolute zero. Radiative heat transfer is unique amongst the fundamental heat transfer mechanisms since it does not require a propagation medium. In the case of a small, hot surface within a cold enclosure, the local radiative heat transfer can be described according to the Stefan-Boltzmann law for

grey-bodies:[36]

$$q_{rad} = \epsilon\sigma(T^4 - T_a^4) \quad (4.17)$$

where $q_{rad}[\text{W cm}^{-2}]$ is the local radiative heat transfer, ϵ is the emissivity, σ is the Stefan-Boltzmann constant, $T[^\circ\text{K}]$ is the temperature of the hot surface, and $T_a[^\circ\text{K}]$ is the ambient temperature.(Note: in the following sections, q_i will refer to the local heat, while Q_i is the global heat) Emissivity represents the radiative ability of a real surface in comparison to an ideal blackbody, i.e. a perfect radiator. It takes a value between 0 and 1, depending on the surface state, and will be higher for rough, oxidized and/or diffuse surfaces. [1]

In the case of EB-PVD thermal accounting, Eq. 4.17 defines the heat loss as a function of the local temperature $T(\mathbf{x})$. In order to calculate the net radiative heat loss, Q_{rad} as described in Eq. 4.16, we must integrate Eq. 4.17 over the entire surface:

$$Q_{rad} = \int_{A_e} q_{rad}(T(\mathbf{x})) dA_e \quad (4.18)$$

where A_e is the evaporant surface and $T(\mathbf{x})$ is the evaporant surface temperature at location \mathbf{x} . Finally, radiative heating will increase the substrate temperature, thus influencing the coating chemistry and microstructure.

Thermal Conduction

Thermal conduction is a fundamental heat transfer mechanism which occurs due to the diffusion of electrons and phonons in the presence of a temperature gradient. Thermal conduction is defined by Fourier's law:

$$q_{cond} = -\kappa\nabla T \quad (4.19)$$

where q_{cond} [W cm^{-2}] is the local conduction rate, κ [$\text{W cm}^{-1} \text{K}^{-1}$] is the thermal conductivity, and ∇T [K cm^{-1}] is the temperature gradient.

When two bodies are in contact, a temperature drop is observed at the interface between the surfaces. This discontinuity is the result of the thermal contact resistance, and in terms of heat transfer is defined according to:

$$q_{contact} = -\alpha_c(T_{hot} - T_{cold}) \quad (4.20)$$

where $q_{contact}$ [W cm^{-2}] is the contact heat transfer and α_c [$\text{W cm}^{-2} \text{K}^{-1}$] is the contact conductance. The contact conductance depends on the contact pressure, junction temperature, as well as the material properties (thermophysical and mechanical), surface finish and interstitial medium. [36] High junction loads and high temperatures result in high contact conductance, whereas light loads and low temperatures lead to low conductance. The concept of contact conductance is important in the context of EB-PVD, since the hot target is mechanically supported, and contact conductance will factor into the heat drawn out of the target.

Convective Heat Transfer

Convection is defined as the diffusion and bulk motion of a fluid which leads to the transfer of heat. [36] In the case of EB-PVD, convection between the evaporating surface and the environment is negligible because of the vacuum. Yet, within the target, convection between the liquid and solid zones can have a marked effect on the material thermal response. Also, the ability of the liquid to transport heat away from the beam spot will define the local evaporation rate, which is

exponentially dependent on the superheating temperature. In a sense, convection results in an enhanced thermal conduction between the solid and molten regions within the target. [37]

There are two main drivers for convective heat transfer within the target:

- Buoyancy: variations in fluid density due to temperature and composition gradients [38]
- Marangoni/Tension: surface tension gradients due to temperature gradients

Large temperature gradients are often observed in rod-feed, high rate evaporation, as the beam spot(2000-4000 K) is within a few centimetres of the water-cooled copper crucible(300-500 K).

In order to briefly examine the effect of convection, previous work on modelling high-rate EB-PVD of Ti64 from a 3" diameter crucible will be presented. [39] The simulated pool shape, isotherms and fluid flow profiles of the model are shown in Fig 4–9.

As shown, the flow patterns of the liquid metal are counter-rotating cells, while the surface dynamics are strongly related to the temperature gradients along the surface. The liquid flow speed is high due to the low viscosity of the liquid metal and large temperature gradients, demonstrated by the close spacing of the isotherms near the beam impact. As the maximum surface temperature increases, the buoyancy forces increase the circulation rate, increasing conduction between the target and crucible. In the model of Fig. 4–9, simulations predicted that the evaporation rate would *decrease* above a threshold of increasing beam power. [39] This counter-intuitive result is due to the dimple formed by the recoil force of the

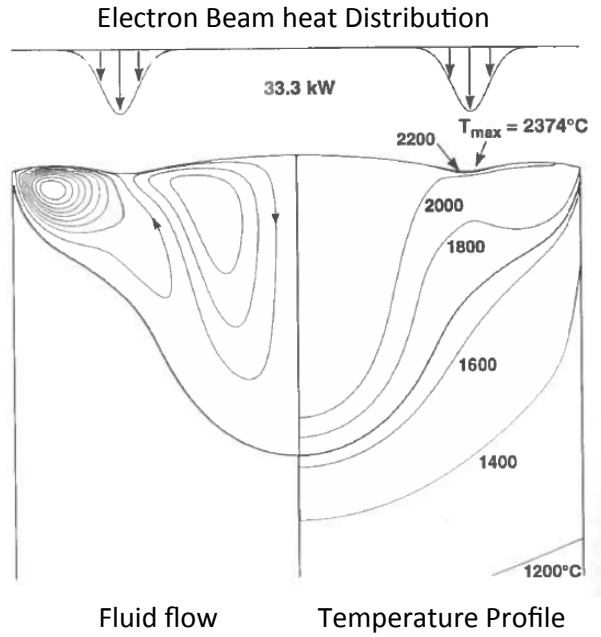


Figure 4-9: Simulated pool shape(right), fluid flow(right) and temperature contours(left) for rod-fed EB-PVD of Ti[39]

emitted vapour, which shortens the conduction path between the beam spot and crucible.

A great deal of research has been conducted on Marangoni convection in electron beam melting as it can be used as a dam to sweep low density inclusions against the hearth flow direction, extending their transit time and minimizing their incorporation into the finished ingot. [27] The Marangoni shear force is based on the surface tension gradient, which for a horizontal surface is: [6]

$$\tau_{xi} = \frac{d\sigma}{dT} \nabla_s T \quad (4.21)$$

where σ is the surface tension and ∇_s is the surface gradient. The sign of $d\sigma/dT$ dictates the direction of Marangoni flow, with negative values dragging the surface down the temperature gradient from the beam hot spot to the liquid/solid interface. The coefficient is also dependent on the impurity content of the melt, and the possible formation of slag/oxidation layer.

The Marangoni shear force will establish high local flow velocities near the e⁻beam spot. The velocity field is confined to the surface and results in a small amount of momentum transfer into the bulk. [27] As shown by Powell, [6] the maximum velocity of the fluid along the beam trace, u_x can be higher or lower than the beam scan speed, v_{beam} . If $u_x > v_{beam}$ the molten metal surrounding the beam spot is capable of following the scan pattern, resulting in high superheating and high evaporation. In this regime, the maximum velocity is achieved in front of the beam. Conversely, when $u_x < v_{beam}$, the molten region is shed as the beam traces the deflection pattern, and thus the maximum temperature and total evaporation rate fall rapidly. In this case, the highest velocities are found in the beam wake.

These examples demonstrates the complexity associated with modelling any electron beam heating process, especially considering the precision and accuracy of convection parameters at elevated temperatures, i.e. surface tension, density and viscosity temperature dependence. [27] In simple models, the effect of convective heat transfer is accounted for by enhancing the thermal conductivity at the surface and within the liquid and also introducing a contact resistance between the solid/liquid interface. [37]

Latent Heat of Vaporization

As materials transition to vapour phase, heat delivered by the beam is consumed as latent heat of evaporation, and is locally defined as:

$$q_{vap} = L_{vap}J_{vap} \quad (4.22)$$

where L_{vap} [J g^{-1}] is the specific latent heat of vaporization, and J_{vap} [$\text{g cm}^{-2} \text{s}^{-1}$] is the evaporant flux. The evaporant flux will not be discussed any further in this section, as a more thorough discussion is presented in Chapter 5. For the purposes of the thermal accounting, J_{vap} depends exponentially on temperature and normally does not become appreciable for temperatures below the melting temperature.

The latent heat of condensation, which is the reverse of vaporization, is capable of transferring heat to the substrate in conjunction with radiative heat transfer. Thus high evaporation rates will result in high substrate temperature via radiative and condensation heat transfer.

4.5.1 Nickel Evaporations C3-C7: Global Heat Transfer

A series of nickel evaporations were performed in order to measure and understand the heat transfer mechanisms during evaporation. In other words, these experiments attempt to explain the net heat into and out of the target, as per Eq. 4.16. The experiment consisted of five evaporations, referred to by the stainless steel substrates used in each run: C3, C4, C5, C6, C7. It should be stated that many rough assumptions are made, yet the results offer a great deal of insight into interplay between machine inputs and evaporative outputs.

During each experiment, the beam power and deflection pattern were kept constant, while the center of the small deflection pattern relative to the large Ni target was varied. The beam focus during each run was modified in real-time, with the results documented in the appropriate lab notebooks. The effects of beam focus were not the initial motivation for the experiments, but the final results demonstrate the importance of this processing parameter.

A ZrO_2 thermal spacer was inserted between a 4" OD Ni target and the Al target holder, with the exception of C7, which used an Al_2O_3 insulator of the same diameter and thickness. Images of the target geometry and thermocouple configuration are shown in the Solidworks model of Fig. 4–10 below.

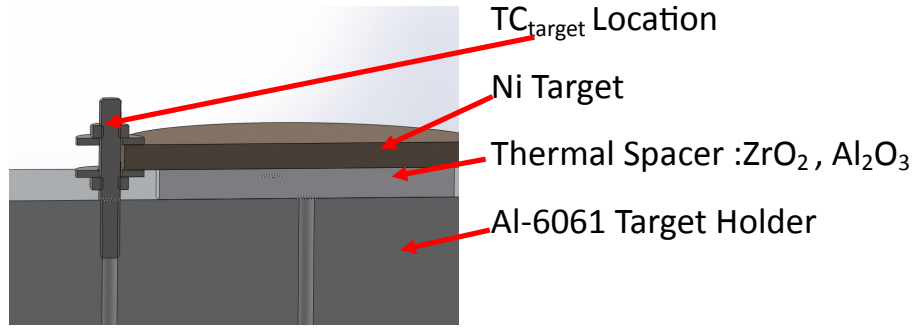


Figure 4–10: Target cross section demonstrating position of TC_{target} and thermal insulator

The net heat transferred into the target was calculated by time integration of the voltage-current product and subtracting the BSE losses according to Sec. 4.3.1. For reference, the deposition time was 20 minutes, with a steady state HVPS power ramped up to 60 kV*20 mA. CASINO was used to calculate $\eta_{power} = 0.327$

assuming an incidence angle of 55° , but does not capture the observed deformation of the molten surface during evaporation.

The deflection pattern used was defined according to the deflection coil signals of Table 4–1. The resulting beam pattern and velocity profile was simulated according to Section 3.2.4, with the results shown in Fig. 4–11. Prior to each evaporation, a scribe mark was placed on the target, with the purpose of aligning the raster pattern and substrate.

Axis	u	v
Type	Triangular	Square
Amplitude [V]	1	2
Phase [$^\circ$]	0	135
f [Hz]	50	500

Table 4–1: C3-C7 Deflection pattern signals [u, v]

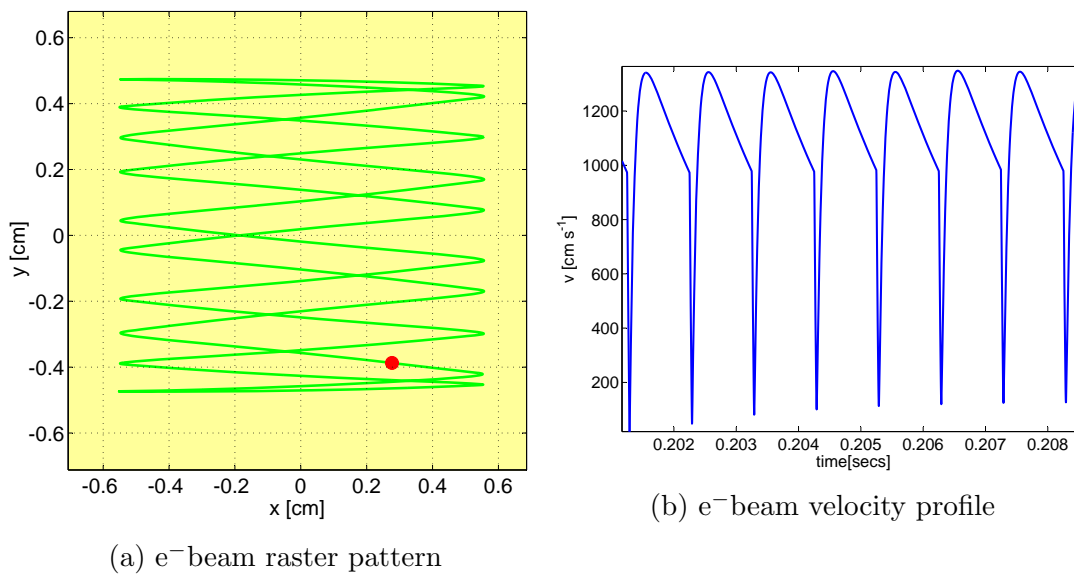


Figure 4–11: C3-C7 Deflection pattern and velocity profile. Beam is incident from right

K-Type thermocouples were spot welded onto the target and target holder in order to estimate the radiation and conduction heat loss mechanisms. The locations of the thermocouples was previously shown in Chapter 2, Fig. 2–5.

Vaporization Losses

After each evaporation, the step height under a shadow mask was measured using a profilometer in order to determine the Ni coating thickness. Visually, the coatings appeared identical, with the exception of condensed Ni droplets (i.e. spits) that were formed due to the over focusing of the beam. Considering the importance of evaporation rate, deposition rate, spitting and thermophysical parameters with regards to EB-PVD, an entire chapter has been dedicated towards the discussion (see: Chap. 2). The equations of that section will be used, and appropriately referenced.

A coarse estimate of the total evaporated mass can be made based on the thickness of the deposit directly above the vapour emitting surface. The vapour emitting surface was assumed to be a disk of radius $s = 0.6$ cm, matching the area of the square raster pattern in Fig. 4–11a. The substrate-target distance was $h = 8.1$ cm. Assuming the vapour emitting surface is isothermal, we can estimate the total evaporated mass of nickel by manipulating Eq. 5.9 to yield:

$$M_e = \pi \rho h^2 (1 + (s/h)^2) * d_0 \quad (4.23)$$

where ρ is the density [g cm^{-3}], h is the substrate height [cm] s [cm] is the pool radius and d_0 [cm] is the peak coating thickness. We can estimate the vapour flux

of the isothermal pool according to Eq. 5.4 to give:

$$J_{Ni}(T) = \frac{M_e}{A_{disk} * t_{evap}} \quad (4.24)$$

where $J_{Ni}(T)[g\text{ cm}^{-2}\text{s}^{-1}]$ is the vapour flux, $M_e[g]$ is the evaporant mass, $A_{disk}[\text{cm}^2]$ is the area of the isothermal pool and $t_{evap}[\text{s}]$ is the evaporation time. Using $J_{Ni}(T)$, the equivalent isothermal surface temperature can be determined from Fig. 4–12.

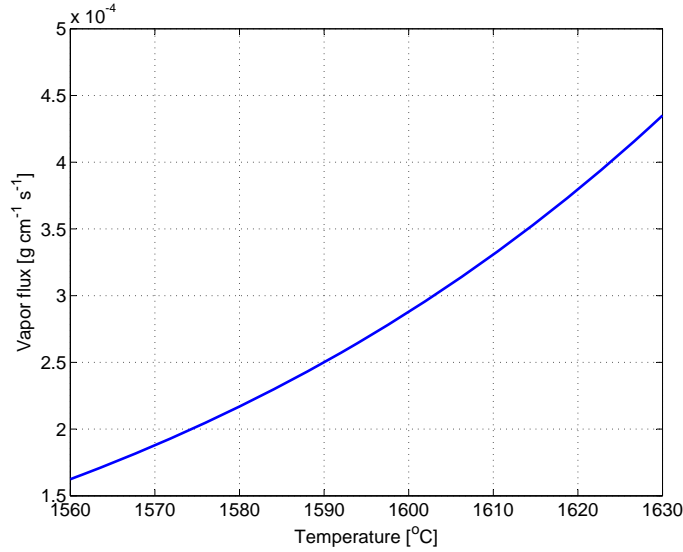


Figure 4–12: Vapour pressure of nickel, calculated according to Sec. 5.2.1

Finally, the heat loss due to the latent heat of evaporation can be calculated according to Eq. 4.22 given above using $L_{Ni} = 6433\text{ J g}^{-1}$. [1]

The resulting thickness, net evaporated mass, evaporation heat loss, vapour flux and isothermal surface temperature of each run is given in Table 4–2.

The above derivation assumes an isothermal melt pool of known diameter, which was approximated by using the high beam scan speeds($\bar{v} \approx 1100\text{ cm s}^{-1}$).

Substrate	d_0 : [μm]	Spits	M_e [g]	Q_{vap} [kJ]	J_{Ni} [$g\ cm^{-2}s^{-1}$]	$T_{surface}$ [$^{\circ}C$]
C3	2.2	Yes	0.40	2.6	3.0E-4	1605
C4	1.8	Yes	0.32	2.1	2.4E-4	1590
C5	1.7	Yes	0.31	2.0	2.3E-4	1585
C6	1.3	No	0.25	1.5	1.7E-4	1565
C7	2.0	No	0.37	2.3	2.7E-4	1595

Table 4–2: C3-C7 Coating thickness and presence of condensed spits.

Despite identical beam current and accelerating voltage, a significant spread in coating thickness was measured. As mentioned, the beam focus was adjusted in real-time, such that spitting was countered by reducing the beam focus. Thus, evaporations with little or no spitting will have lower evaporation rates, which explains why C6 has the lowest coating thickness and no spits. C3 had the most aggressive focusing schedule. In each case, the focusing schedule was pruned back as the depositions proceeded through C4,C5,C6. Interestingly, C7 had a focusing schedule similar to C3 yet not spits were observed. A detailed discussion of spitting is reserved for Sec. 5.3.3.

Finally, it is worth highlighting the effect of superheating on evaporation rate above the melting temperature of $1455^{\circ}C$. As Table 4–2 shows, a temperature difference of $1565^{\circ}C$ and $1605^{\circ}C$ results in a coating thickness difference 40%, highlighting the exponential nature of evaporation rate on temperature.

Conduction Losses

$TC_{holder2}$ measures the temperature increase of the massive Al substrate holder, giving an indication of the conduction losses. The net conduction loss can

be estimated using a calimetric approach according to:

$$Q_{cond} = c_p * M_{Al} * \Delta TC_{holder2} \quad (4.25)$$

where c_p is the heat capacity of 6061 aluminium ($0.87 \text{ J K}^{-1} \text{ g}^{-1}$), M_{Al} is the mass of the Al support ($16.08 \cdot 10^3 \text{ g}$) and $\Delta TC_{holder2}$ is the temperature increase of the Al block, measured with $TC_{holder2}$ and shown in Fig. 4–13. Conduction between the stainless steel chamber and the aluminium block is neglected for simplicity.

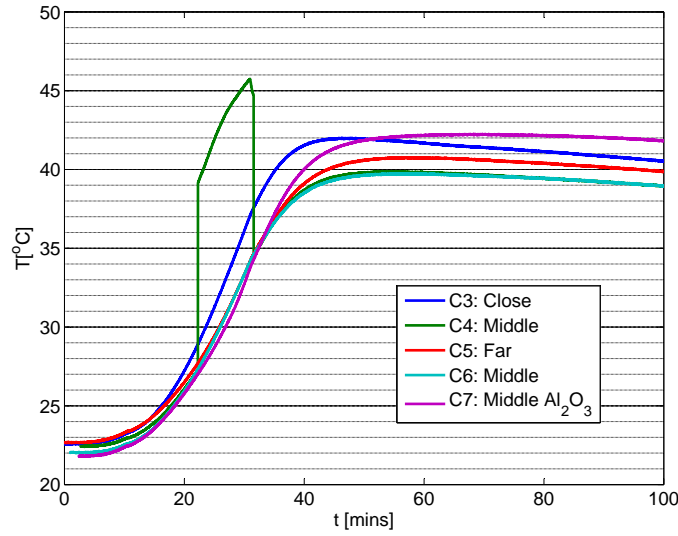


Figure 4–13: $TC_{Holder2}$ readout. In evaporation C6, the thermocouple reader inexplicitly failed, explaining the discontinuity.

The response of $TC_{holder2}$ demonstrates that the total heat transferred to the target holder decreases from C3-C6, suggesting a decreased conduction to the target holder. This is most likely due to thermophysical changes in thermal insulator. The conduction loss calculation for each run is given in Table 4–3.

Substrate	$\Delta TC_{holder2}$	Q_{cond} [kJ]
C3	20.3	283.9
C4	17.7	247.3
C5	18.1	253.2
C6	17.8	249.0
C7	20.5	286.7

Table 4-3: C3-C7 Conduction loss calculation

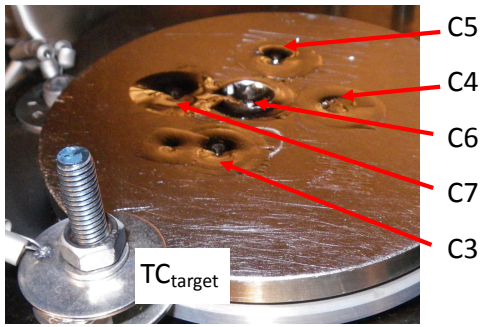
Surprisingly, the conduction losses between the ZrO_2 ($\kappa = 2 \text{ W m}^{-1} \text{ K}^{-1}$) and Al_2O_3 ($\kappa = 35 \text{ W m}^{-1} \text{ K}^{-1}$) are nearly identical. This is likely due to the contact conductance dominating the heat transfer between the target and the Al support.

Radiation Losses

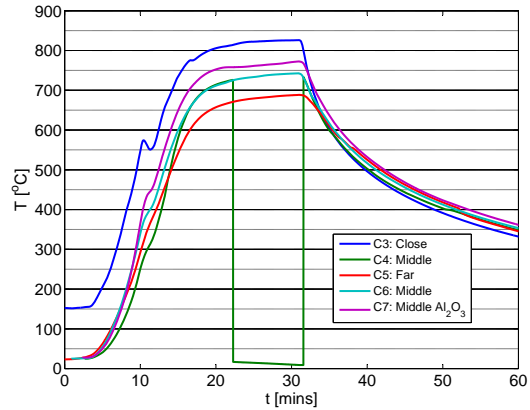
TC_{target} gives an indication of the temperature distribution over the nickel surface and can estimate the net radiative heat loss of the hot nickel surface. As shown in Fig. 4-14a, the distance between the evaporation spot and the thermocouple increases as we proceed from C3-C4-C5.

In the corresponding thermocouple response of Fig 4-14b, the steady state temperature decreases with increasing distance from the raster pattern, as expected. It is worth noting that C4 and C6 have similar distance from TC_{target} , which is captured by the nearly identical response of TC_{target} .

To estimate the radiation loss, assume that the temperature at the beam spot is given by the isothermal pool temperature determined from the vapour flux estimation (1565-1605°C). Now assume the target is radially symmetric about the beam spot and the temperature linearly decreases from the edge of the melt from T_{melt} to TC_{target} , as shown in Fig 4-15a.

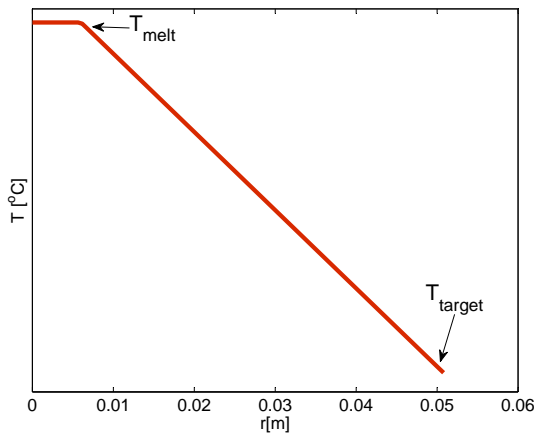


(a) Location of evaporation centers

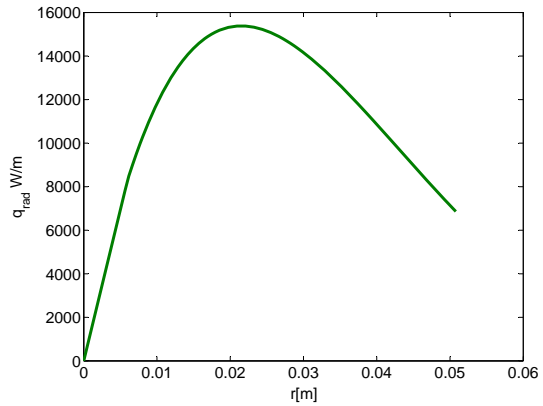


(b) TC_{target} response

Figure 4–14: C3-C7: TC_{target} location and response. In evaporation C6, the thermocouple reader inexplicitly failed, and was restarted at the end of the evaporation in order to capture the cool down.



(a) Assumed temperature profile



(b) Integrand of Eq 4.26

Figure 4–15: C3-C7: Assumed temperature profile and radial radiative power

The net radiative heat transfer can be estimated by integrating the local temperature, using appropriate substitutions of Eq. 4.17-4.18 and the appropriate radial symmetry substitution $dA_e = 2\pi r dr$:

$$Q_{rad} = \epsilon\sigma \int_0^R (T(r)^4 - 293^4) * 2\pi r dr \quad (4.26)$$

where R is the radius of the target (0.0508 m), ϵ is the emissivity of nickel ($\epsilon = 0.35$ at 1450°C [1]) and $T(r)[\text{K}]$ is the temperature profile given in Fig 4–15a. The integrand of Eq. 4.26 is shown in Fig 4–15b and the integration results for each run are given in Table 4–4.

Substrate	T_{melt} [$^\circ\text{C}$]	T_{edge} [$^\circ\text{C}$]	Q_{rad} [kJ]
C3	1605	825	755
C4	1590	733	654
C5	1585	688	611
C6	1565	742	638
C7	1595	772	694

Table 4–4: C3-C7 Radiative Energy based on Eq. 4.26 and temperature profile of Fig 4–15a

The values derived in Table 4–4 are based on gross assumptions motivated by intuition and simplicity. The assumption that the entire surface has a steady state temperature profile neglects the transient heating time of 5 minutes shown in Fig 4–14b. The linear temperature decrease was chosen for simplicity, and will not reflected the actual temperature profile, which requires coupling the radiation and conduction within the Ni. Also, only deposition C6 was centered on the target, with other runs being off-center. Most importantly, ϵ is dependent on the temperature and surface state, and can only be seen as an estimation. For instance, an oxidized Ni surface at 1000°C has an ϵ value of 0.84, which results in a 240% increase in the radiative heat loss compared to $\epsilon = 0.34$ used in this calculation. [1]

Despite these shortcomings, many of the salient features can be discussed. The excessive target area results in large radiative losses. Changing the integration limits of Eq. 4.26, we find that only about 5% of the radiative losses are due to the melt pool area. This highlights the importance of optimizing the crucible design for particular application and material. Radiative heat is transferred to the vacuum chamber, motivating the need for water-cooled chambers in high power applications (>50kW). If deposition shields are used, careful thought must be given to their design as they will heat up significantly depending on their construction and the deposit surface state (oxidation, reflectivity, etc.).

Nickel Evaporation: Summary

Having roughly calculated each global heat mechanism as per Eq. 4.16, we can now compare the results for each run, which are shown in Table 4-5.

Substrate	Q_{vap} [kJ]	Q_{cond} [kJ]	Q_{rad} [kJ]	Sum [kJ]	Q_{HVPS} [kJ]	Q_{BSE} [kJ]	Q_{beam} [kJ]
C3	2.6	283	755	1040	1412	461	950
C4	2.1	247	654	903	N/A	N/A	N/A
C5	2.0	253	611	866	1379	450	928
C6	1.5	249	638	888	1439	470	968
C7	2.3	286	694	982	1432	468	963

Table 4-5: C3-C7 Net thermal accounting

The values derived from the thickness and thermocouples is given in the right section of the table, while the beam values calculated from the equipment datalogger and CASINO are given in the left hand section. The most surprising feature of Table 4-5 is the agreement between the sum of Q_{vap} , Q_{cond} , Q_{rad} in

comparison to Q_{beam} . It is believed that that the agreement must be due to chance, as many simplifying (and admittedly erroneous) assumptions were made.

Another interesting feature is the efficiency of the conversion of the High Voltage Power Supply (HVPS) output to evaporation, which is around 0.15%. Although the values calculated for Q_{rad} are rough, Fig. 4–15b suggests that reducing the target diameter would be beneficial. The 4” target was chosen because of availability.

The machine parameters chosen during the experiment were motivated by previous experience and future work should carefully consider the interplay between raster pattern, beam focus and beam power. Specifically, experimental improvements would require a water-cooled copper crucible, whereby the real-time conduction loss can be measured via the water temperature. Using pre-weighted Ni charges for each run would stabilize the changes to the target geometry from run to run.

Finally, the beam deflection pattern should be improved, as it is now apparent that the frequency response of the deflection coils results in undesirable spread in velocities, as shown in Fig 4–11b. The moments when the beam is moving slowly (i.e. changing direction) results in long dwell times. These slow moments result in high superheating, and thus increased probability of spitting.

A deflection pattern which accounts for the frequency response of the coils might be the product of a high and low frequency signal, e.g. $A\sin(\omega_o t)\sin(10\omega_o t)$ and would require operating software modifications. The output pattern and velocity profile on one such signal, whereby $\omega_o = 2\pi*50$, is shown in Fig. 4–16.

The advantage of this proposed signal is large area coverage area and a relatively constant velocity while operating within the frequency response of the coils.

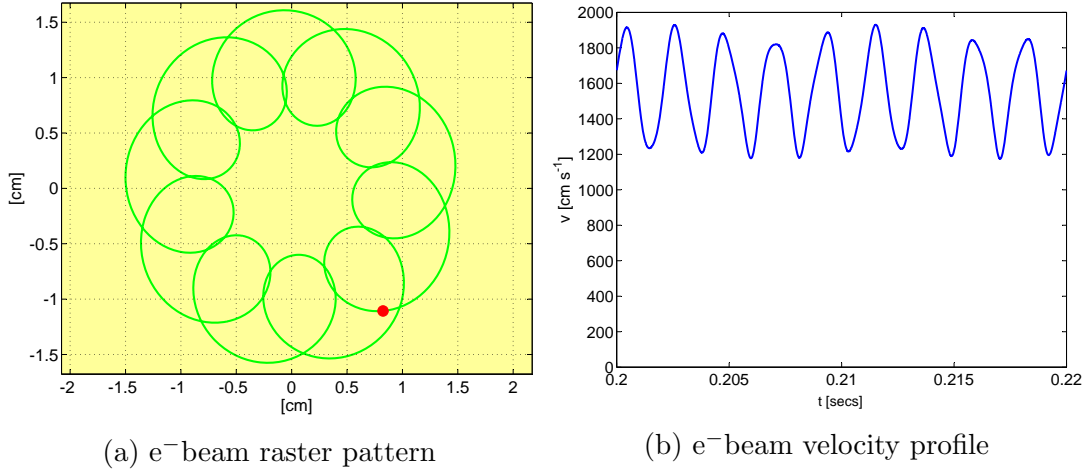


Figure 4-16: Proposed deflection pattern for improved evaporation behavior

4.5.2 Heat Transfer Discussion

The arguments presented above demonstrate some of the interplay between the material and beam parameters. Specifically, over focusing results in high deposition rates, but also in spitting. Large area targets will have a large radiative heat loss if the thermal conduction is high ($\kappa_{Ni} = 90 \text{ W m}^{-2} \text{ K}^{-1}$).

During evaporation, operators should strive for a surface temperatures corresponding to a vapour flux of $J_{vap} = 10^{-4} \text{ g cm}^{-2} \text{ s}^{-1}$. [8] This value corresponds to appreciable evaporations rates, while not being so high that the vapour recoil force causes spitting.

As shown, a target evaporation rate implies an approximate surface temperature, T_{evap} , defined by the thermophysical material parameters. Thus, for a given material, if T_{evap} is low, the heat loss associated of first power temperature

dependence of conduction dominate(see Eq. 4.19). As materials with higher evaporating temperatures are used, radiation heat loss, which is proportional to the 4th power of T , eventually overtake conduction. Axial EB-PVD is specifically tailored for evaporating refractory materials such as Ta and YSZ, thus large amounts of radiative heating should be expected. In either case,, the exponential temperature dependence of vaporization heat loss(Eq. 4.22) will limit the maximum surface temperature rate, while also causing significant melt pool spitting and liquid circulation.

In conclusion, temperature gradients will have significant effects on the net evaporation rate as well as the local convection. Temperature gradients will be a function of beam parameters such as beam spot size, energy density, deflection pattern and deflection speed. Thus, for any given material, the beam power($U_b * I_b$), focus(w_b) and scanning pattern ($[u, v]$) must be adjusted according to the target geometry, BSE losses and thermophysical material parameters, often requiring repeated experiments in order to determine a set of acceptable inputs. Finally, for high productivity and repeatability, the target holder should be optimized for a particular target material and gun power.

4.6 Heat Equation

At the most basic level, the e^- beam power is converted to heat at or near the surface of the evaporant. The heat input raises the surface temperature, establishing a local evaporation rate. For the Ni evaporations, it was observed that the beam focus has a significant effect on the evaporation rate, and thus, in the following section, we will examine the effect of energy density and dwell time.

As previously mentioned, the heat equation couples the beam parameters to the evaporation equation. Conservation of energy is mathematically described according to the three dimensional heat equation, which is a parabolic Partial Differential Equation (PDE) given by:

$$\nabla(\kappa\nabla T(\mathbf{x})) + \mathbf{Q}(\mathbf{x}, t) = \rho c_p \frac{dT(\mathbf{x})}{dt} \quad (4.27)$$

where ∇ is the vector differential operator, κ is the thermal conductivity, $T(\mathbf{x})$ is the temperature at position \mathbf{x} , $\mathbf{Q}(\mathbf{x}, t)$ is a distributed heat source/sink term, ρ is the density, and c_p is the heat capacity. The first term in Eq. 4.27 refers to the conduction losses, while the right hand side represents the transient temperature response. Boundary conditions are used in order to determine the radiation, conduction and evaporation losses, according to the heat transfer mechanisms given in Eq. 4.16.

Since an electron-beam heated target will depart significantly from room temperature, solving Eq. 4.27 requires numerical methods to account for the non-linear thermophysical material parameters, (κ, ρ, c_p) as well as the non-linear losses (q_{rad}, q_{vap}) . In the case of 1^D heat conduction with isotropic thermal conductivity, Eq. 4.27 becomes:

$$\frac{\partial^2 T(z, t)}{\partial z^2} + \frac{Q(z, t)}{\kappa} = \frac{1}{\alpha} \frac{\partial T(z, t)}{\partial t} \quad (4.28)$$

where $\alpha = \kappa/\rho c_p$ [$\text{m}^2 \text{s}^{-1}$] is the thermal diffusivity, and represents the heat propagation speed. In other words, α represents the ability of material to conduct

thermal energy relative to its ability to store the energy. In the case of metals, variations in α will manifest themselves mostly via thermal conductivity.

In the following sections, Eq. 4.28 will be solved using numerical methods and compared to appropriate numerical solutions.

4.6.1 Semi-infinite Solid with Surface Flux

In the case of a semi-infinite solid with a constant surface heat flux, Eq. 4.28 has a analytical solution for $T(z, t)$. The initial conditions assume $T(z, 0) = T_o$ while the mixed boundary conditions are given by: $T(\infty, t) = T_o$ and $-\kappa T'(0, t) = q_o$. (Note: T' represents the spatial derivative of temperature, while \dot{T} is the time derivative) The resulting temperature distribution is given according to:[36]

$$\Delta T = T(z, t) - T_0 = \frac{L_{th}q_o}{\kappa\sqrt{\pi}} \left(\exp(-u^2) - \sqrt{\pi}u * \text{erfc}(u) \right) \quad (4.29)$$

where the u is a non-dimensionalization factor, $u = z/L_{th}$, $\text{erfc}(x)$ is the complementary error function and $L_{th} = 2\sqrt{\alpha t}$. L_{th} is referred to as the thermal diffusion length and represents the natural length constant of the temperature profile at time t after the heat source is activated. A non-dimensionalized plot of Eq. 4.29 is given in Fig 4–17.

Fig. 4–17 shows the temperature variation, and the corresponding heat, will be confined within layer of thickness L_{th} , which grows as \sqrt{t} . This length scale is a critical parameter in any transient heating mechanism. As an example, materials with large α such as Cu ($\alpha_{Cu} = 116*10^{-6} \text{ m}^2 \text{ s}^{-1}$)[1] will quickly diffuse the heat flux while materials with low α such as grade 5 titanium ($\alpha_{Ti64} = 8*10^{-6} \text{ m}^2$

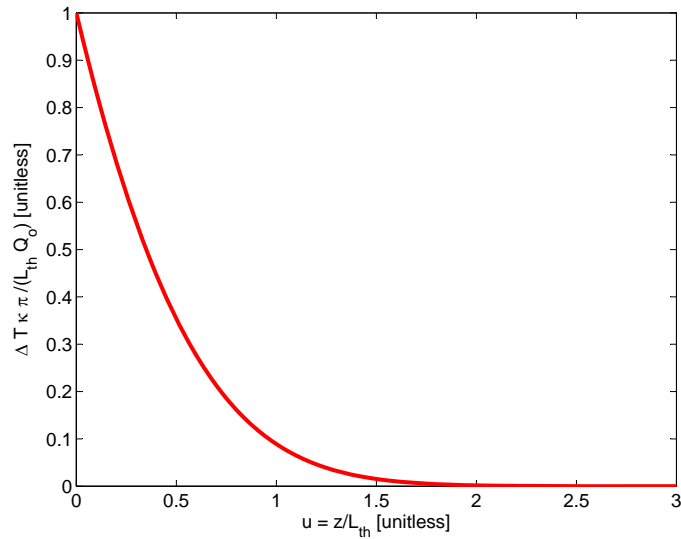


Figure 4–17: Normalized temperature distribution for surface flux on semi-infinite solid with conduction only. u is the non-dimensionalization factor $u = z/L_{th}$

s^{-1}][1] will sluggishly transport heat, resulting in higher surface temperatures for a given heat flux.

To compute an equivalent numerical solution to Eq. 4.29, the MATLAB[®] function `pdepe` was chosen. [40] `pdepe` solves parabolic and elliptic PDEs by approximating the first and second order derivatives with respect to the spatial variable z . The resulting Ordinary Differential Equation (ODE) is integrated using the MATLAB solver `ode15s`, which is an implicit solver for numerically stiff problems using the variable order method. Stiff problems refer to systems with widely different eigenvalue magnitudes, which cause transient solutions to become unstable for large time steps.

In order to benchmark **pdepe**, the numerical solution is compared against the analytical result of Eq. 4.29. Using Ni as the target, the problem was defined as follows:

- Initial Temperature: $T(z, 0) = T_o = 293^\circ\text{C}$
- Surface Heat flux: $-\kappa T'(0, t) = 4 \cdot 10^4 \text{ W cm}^{-2}$. This value approximates the e⁻beam energy density assuming the FWHM of $1000 \mu\text{m}$ at 60kV/10mA, while subtracting the BSE losses for Ni.
- Simulation time: $t_{final} = 1\text{mS}$
- Boundary Condition $T(10L_{th}, t) = T_o$, which approximates the semi-infinite solid during time $[0, t_f]$, whereby L_{th} is the thermal diffusion length according to the simulation time t_f

The thermophysical material parameters of Ni are given in Table 4-6:

ρ [g cm ⁻³]	L_{vap} [kJ g ⁻¹]	c_p [J K ⁻¹ g ⁻¹]	κ [W cm ⁻¹ K ⁻¹]	ϵ
8.90	6.433	0.426	0.9	0.33

Table 4-6: Thermophysical material parameters of Nickel target [1]-[2]

The time evolution of temperature is given in the 2^D plot of Fig. 4.16, where the x, y plane represents time and depth, and the z axis is temperature. The semi-infinite solid approximation, $T(10L_{th}, t) = T_o$ is validated considering that $\Delta T(5L_{th}, t_{final}) = 0.1^\circ\text{C}$, proving that negligible heat is conducted into the lower boundary.

The absolute error between the numerical and analytical solutions is given in Fig 4-18b. Except for the beginning of the heating cycle, we see that the error between the analytical and numerical solution is negligible.

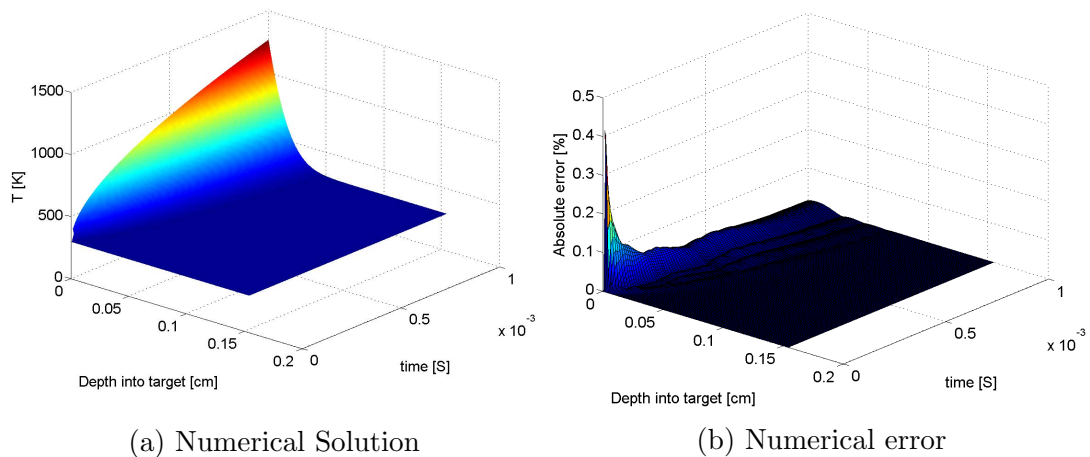


Figure 4–18: Comparison of analytical and numerical solution for 1^D constant surface flux using Ni and pdepe

4.6.2 Electron Beam Evaporation: 1^D Solver

Having established pdepe as a 1^D PDE solver, we can now incorporate the non-linear mechanisms of Electron-Beam Physical Vapor Deposition (EB-PVD), namely: transient beam heating, evaporation and radiation. These terms are incorporated as surface fluxes:

$$-\kappa T'(z = 0, t) = q_{beam} - q_{rad} - q_{vap} \quad (4.30)$$

where q_{rad} is defined according to Eq. 4.17 and q_{vap} is defined according to Eq. 4.22. For each term in Eq. 4.30, special care must be taken to ensure unit consistency.

In Chapter 3, we defined the heat flux along the center line of a electron beam with cross sections σ_x, σ_y , moving at velocity v_x in Eq. 3.11. We can now incorporate the effect of BSE losses such that the absorbed power (= incident -

reflected) is defined according to Eq. 4.31.

$$q_{beam} = (1 - \eta_{power}) \frac{U_b I_b}{2\pi\sigma_x\sigma_y} * \exp\left(-\left[\frac{v * (t - t_0)}{2\sigma_x}\right]^2\right) \quad (4.31)$$

For a focused beam with parameters defined in Table 4-7 incident on Ni ($\eta_{power}=0.32$), we can plot the transient beam flux, q_{beam} for a series of beam velocities, shown in Fig. 4-19, where $t_0 = 2$ mS.

I_b [mA]	U_b [kV]	σ_x [cm]	σ_y [cm]
10	60	0.040	0.0244

Table 4-7: Beam parameters for q_{beam} defined in Fig. 4-19

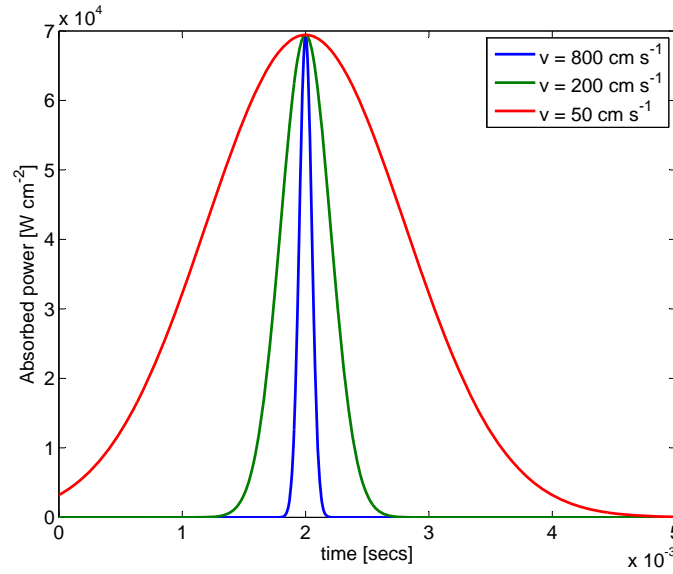


Figure 4-19: Incident power absorption of Ni as a function of beam velocities for beam defined in Table 4-7

The area under the curves of Fig. 4-19 represents the net absorbed energy flux during beam translation, which is 8.3, 33.3, 132.4 J cm⁻² for 800, 200, 50 cm s⁻¹ respectively.

Similar to the case of the semi-infinite solid, we can define the thermal diffusion length as $L_{th} = 2\sqrt{\alpha\tau}$, where α is the thermal diffusivity and τ is the dwell time, equal to $\tau = FWHM/v_x = 2.355\sigma_x/v_x$. The simulation domain for z is chosen to be $[0, 10L_{th}]$, which was shown to approximate a semi-infinite slab. Considering the high thermal gradients in $[0, L_{th}]$, the grid spacing within that region was split up into 1000 nodes, and the domain $[L_{th}, 9L_{th}]$ was split up into 500 nodes. Similarly, the time domain is split into 1000 nodes over the span of 12τ with $t_o = 3\tau$. This approach non-dimensionalizes the simulation mesh with respect to the beam and material parameters.

We can now examine the 1^D thermal response of a material as a function of beam speed, while incorporating the non-linear effects of vaporization and radiation. The temperature independent thermophysical material parameters of Ni in Table 4–6 were used. The values ignore the temperature dependence of κ and c_p as well as the latent heat of melting and magnetization.

In order to demonstrate the effects of non-linear heat loss, simulation results of the surface temperature for the beam of Table 4–7 on Ni at $v = 50, 200, 800$ cm s⁻¹ with $T_o = 300$ K are shown in Fig 4-20. The x-axis is normalized according to $(t - t_0)/\tau$, while the y-axis represents the surface temperature, T_{surf} .

At $T_o = 300$ K, the temperature response is linear, despite the inclusion of the non-linear terms. Specifically, if we examine $\Delta T = \max(T_{surf}) - T_o$, we see that the temperature increases by a factor of two for a fourfold increase in v ($\Delta T = 366, 731, 1457$ K for $v = 800, 200, 50$ cm s⁻¹). This can be explained by returning to the solution for a constant heat flux on a semi-infinite solid, Eq 4.29. The solution

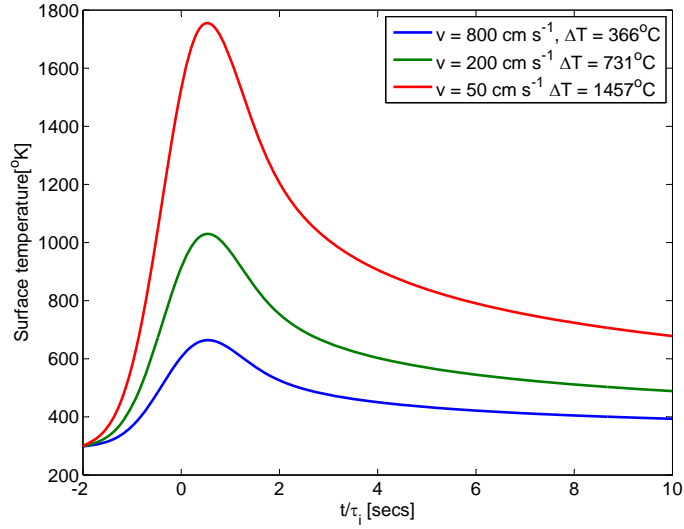


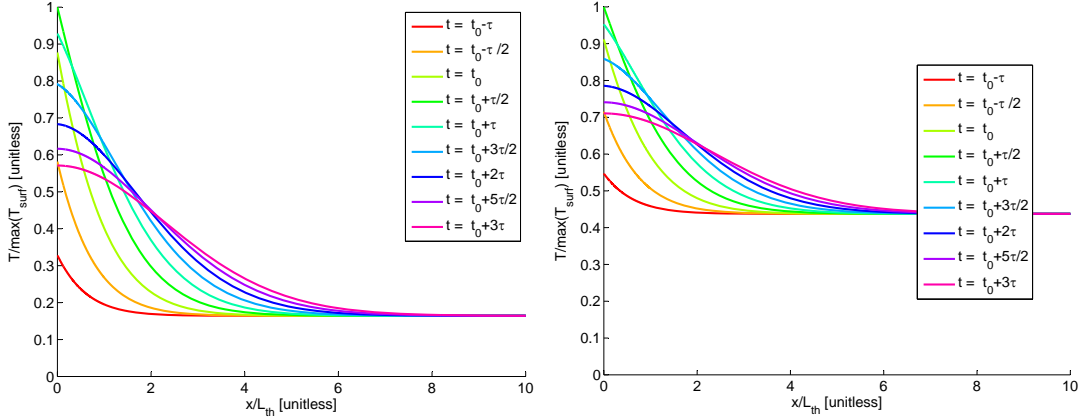
Figure 4-20: Surface temperature of Ni with $T_o = 300$ K . The x-axis is normalized against the speed dependent dwell time, $(t - t_0)/\tau$

shows that ΔT increases with the L_{th} , according to $\Delta T \propto L_{th} \propto \sqrt{\tau} \propto (\sqrt{v})^{-1}$, thus explaining the decrease of ΔT with increasing v .

If we plot the temperature as a function of depth, while normalizing the temperature according to $T/\max(T_{surf})$ and the depth according to z/L_{th} , we can clearly understand what is meant by linear response. Plots for $v = 50$ and 800 cm s^{-1} at $t=\tau/2$ increments are shown in Fig. 4-21, demonstrating similar temperature profiles.

Although simulations for $T_o = 300$ K incorporate non-linear effects, the response of the material appears linear. More importantly, we see that the parameters τ and L_{th} are the relevant thermal scaling factors.

The linear response breaks down when we perform the simulations using $T_o = 1673$ K, . The time-normalized surface temperature plots for $v = 800, 200$



(a) $v = 50 \text{ cm s}^{-1}$, $\max(T_{surf}) = 1755 \text{ K}$ (b) $v = 800 \text{ cm s}^{-1}$, $\max(T_{surf}) = 664 \text{ K}$

Figure 4–21: Normalized temperature-depth profiles for $\tau/2$ time increments, demonstrating linear response of material for $T_o = 300 \text{ K}$

and 50 cm s^{-1} are shown in Fig. 4–22, demonstrating that ΔT no longer scales according to \sqrt{v} , and the temperature plateaus around 2000 K. This temperature value can be explained if we examine q_{vap} , q_{rad} versus $\max(q_{beam})$, as shown in Fig. 4–23.

The logarithmic plot shows that the q_{beam} approaches the q_{vap} around 2000 K, thus explaining the plateau in T_{surf} . In other words, for $T_o = 1673 \text{ K}$, the surface temperature is high enough to induce a measurable amount of evaporative loss, thus making the thermal response non-linear.

Fig. 4–23 also shows that q_{rad} is significantly smaller than $\max(q_{beam})$. Yet, in Section 4.5.1, it was shown that radiation dominates the heat transfer at the global scale. Thus, Fig. 4–23 demonstrates the distinction between local and global heat transfer, with q_{rad} being negligible at the local level. Since q_{rad} is negligible at the

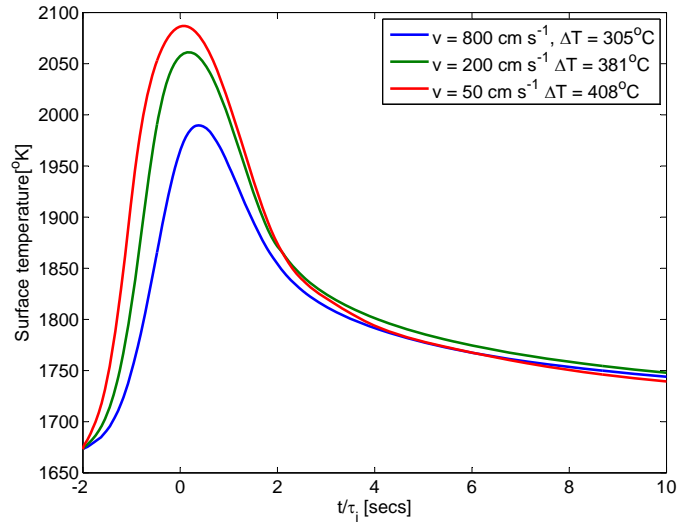


Figure 4-22: Thermal Response of Ni with $T_o = 1673$ K . The x-axis is normalized against the speed dependent dwell time, τ

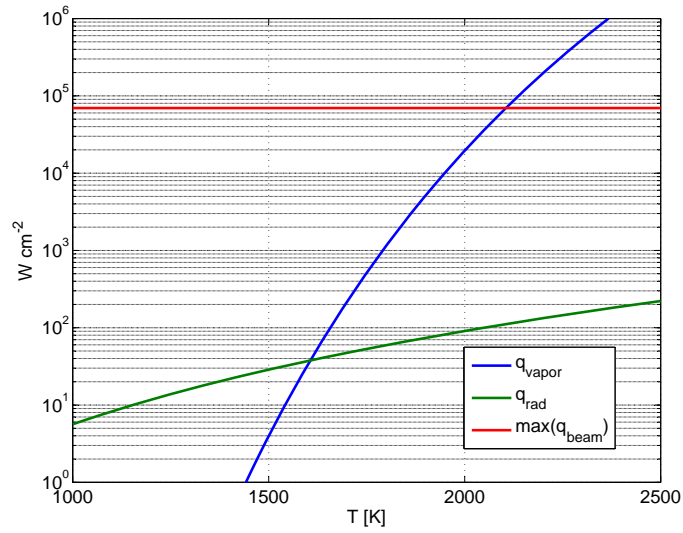


Figure 4-23: Beam, radiation and evaporative flux of nickel. [1]

local scale, it will no longer be discussed, despite being incorporated in the PDE solver.

Since the electron beam is assumed to be a surface flux, we can analyse the heat leaving the surface via conduction and evaporation. In order to estimate the flux via conduction, MATLAB calculates the following approximation:

$$q_{cond} = -\kappa T'(z = 0, t_i) \approx -\kappa \frac{T(z_1, t_i) - T(z_2, t_i)}{(z_1 - z_2)} \quad (4.32)$$

where t_i is time increment i and z_i represents a mesh point, with z_1 at the surface. A plot of q_{beam} , q_{cond} and q_{vap} for $v = 800 \text{ cm s}^{-1}$ at $T_o = 1673 \text{ K}$ is shown in Fig. 4–24.

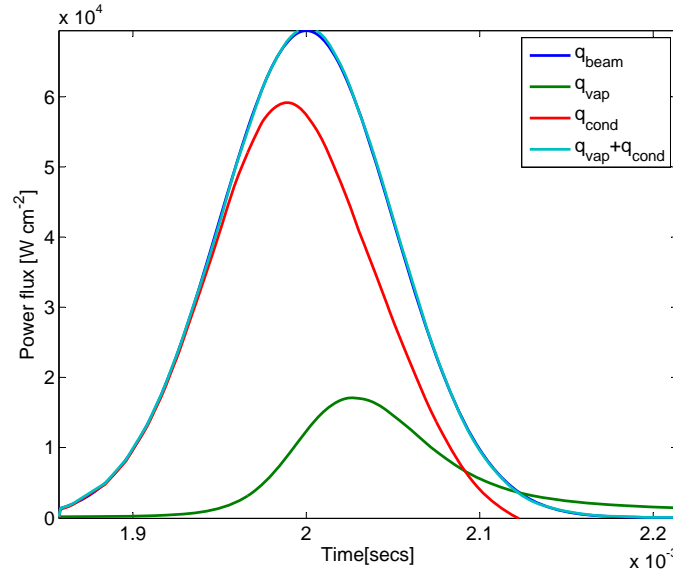


Figure 4–24: Transient surface heat flux for Ni evaporation at $v = 800 \text{ cm s}^{-1}$ at $T_o = 1673 \text{ K}$

The agreement between q_{beam} and $q_{cond} + q_{vap}$ shown in Fig 4–24 demonstrates that Eq. 4.32 accurately captures the conductive heat loss. Also, by integrating the area under q_{vap} and q_{beam} , we can calculate energy flux [J cm^{-2}] delivered to the

target as well as the energy flux consumed by evaporation, thus giving a metric for the evaporation. This metric, referred to as ψ , is calculated by taking the Riemann sum approximation of:

$$\psi = \frac{\int_{t_o}^{t_f} q_{vap} dt}{\int_{t_o}^{t_f} q_{beam} dt} \approx \frac{\sum_{t_o}^{t_f} q_{vap}(t_i) \Delta t}{\sum_{t_o}^{t_f} q_{beam}(t_i) \Delta t} \quad (4.33)$$

where t_i and t_f are the initial and final simulation times. For Fig 4–24, $\psi = 0.24$, which implies that 24% of the beam energy is transformed into Ni vapour.

Considering that $\psi > 0$ implies evaporation, we can use it as a measure of the evaporation for a given set of beam and material parameters. As a first example, we can calculate ψ as a function of T_o for different beam focus, ($[\sigma_x, \sigma_x/1.74]$).

Fig. 4–25 plots ψ for a fixed speed, $v = 800 \text{ cm s}^{-1}$ at FWHMs of 237.5, 475, 950, 1900, 3800 μm .

Understanding Fig. 4–25 is crucial to understanding EB-PVD as it links material and beam parameters to evaporation. First, note that the the beam power is the same in all cases and only the focus changes. At first glance, Fig. 4–25 shows that for a given beam focus, ψ is a function of the initial temperature, T_o . From an operational perspective, this demonstrates the importance of thermal conduction stability. In other words, if the target hasn't reached a global steady-state temperature profile (represented by T_o), the evaporation rate will evolve as the target heats.

Another important consideration is that as the beam is defocused, the net energy flux decreases as $1/\sigma_x$ (ie $\int q_{beam}(237 \mu\text{m}) dt = 2^4 * \int q_{beam}(2^4 *$

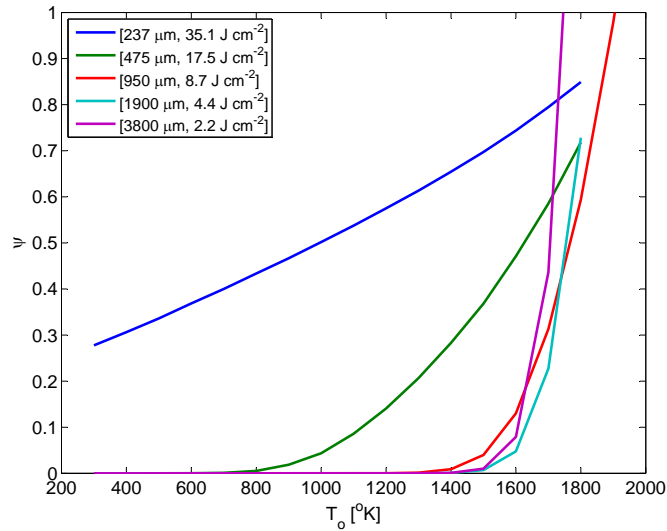


Figure 4-25: ψ as a function of T_o and beam FWHM for $v = 800 \text{ cm s}^{-1}$. The legend represent $[FWHM, Q_{beam}]$

$237 \mu\text{m})dt$). We have already seen that for Ni, T_{surf} peaks at around 2000 K due to evaporative losses, thus T_o will be a function of how often the beam passes (deflection pattern) and how the heat is transferred *out* of the target (crucible design). Thus, evaporation can be optimized via the deflection pattern and beam focus, since a high T_o and large σ results in evaporation with low energy flux. Remember, the net energy deposited into the target is fixed, thus the focus and deflection will determine the local energy flux. Achieving evaporation with a low energy flux will allow for a larger evaporating surface, and thus higher deposition rates.

At the experimental level, Fig. 4-25 explains the discrepancies in Ni thickness measured in Sec. 4.5.1. Specifically, the focus schedule for each deposition was

adjusted in situ, therefore moving between the different curves of Fig. 4–25, resulting in a change in evaporation rate.

Returning to Fig. 4–25, we see that a FWHM = 950 μm beam deposits 8.7 J cm^{-2} , independent of T_o . The plot shows that if the temperature gradients are such that $T_o < 1400 \text{ K}$, we will have little or no evaporation, since all beam heat is converted into conduction. This is demonstrated by the plots of T_{surf}, q_{beam} , vs t in Fig. 4–26a and q_{vap}, q_{cond} vs t shown in Fig. 4–26b. Since the amount of energy deposited does not raise the surface temperature $> 1900 \text{ K}$, evaporation does not occur and the beam energy is transported away via conduction.

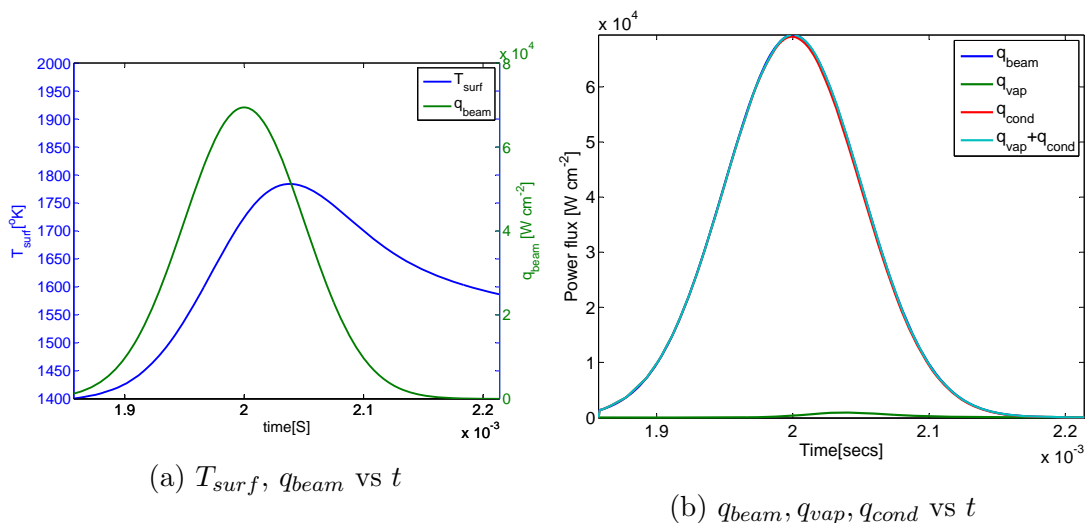


Figure 4-26: Power and temperature profiles for $v = 800 \text{ cm s}^{-1}$ at $T_o = 1400 \text{ K}$

Conversely, for $T_o = 1600 \text{ K}$, the thermal gradient between the surface and the bulk is reduced, and more beam energy will be converted to vapour generation. This effect is shown in Fig 4–27b, where $q_{vap} > 0$ at the tail end of the beam translation.

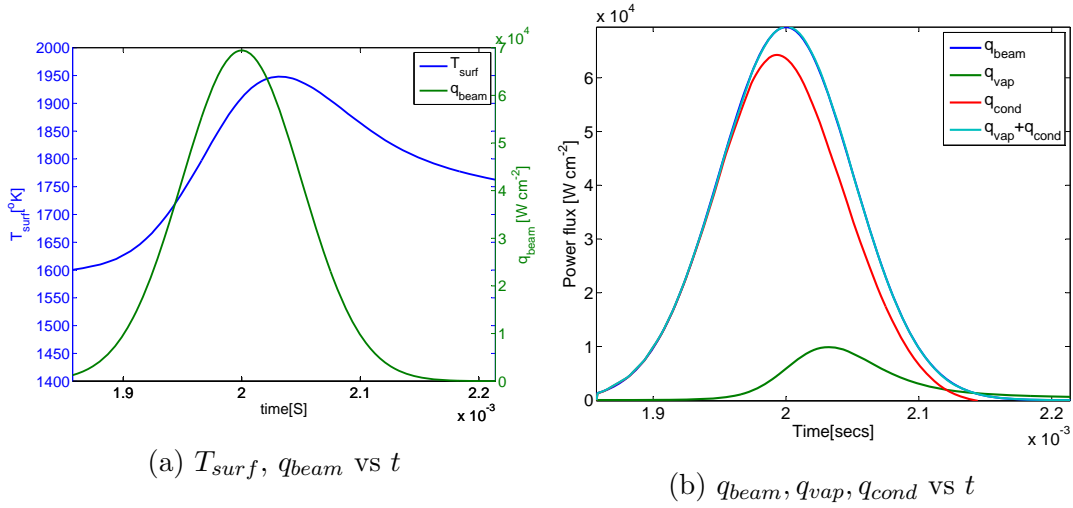


Figure 4-27: Power and temperature profiles for $v = 800 \text{ cm s}^{-1}$ at $T_o = 1600 \text{ K}$

Similar results occur as we vary the beam speed for a fix set of beam parameters (σ, I_b, U_b). Fig 4-28 is a plot of ψ versus T_o for $v = 50, 100, 200, 400, 800 \text{ cm s}^{-1}$ using a FWHM of $950 \mu\text{m}$.

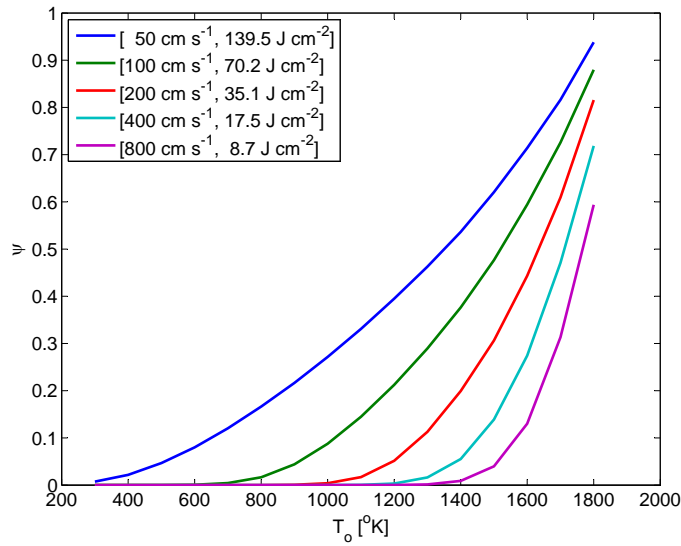


Figure 4-28: ψ as a function of T_o and beam speed for FWHM = $950 \mu\text{m}$. The legend represent $[v, \int q_{beam} dt]$

Again, Fig. 4–28 demonstrates a critical component of the EB-PVD process: deflection speed. We see that for a given T_o , the local evaporation will decrease with increasing speed, until a limit whereby the energy deposited is insufficient to achieve any evaporation. This demonstrates why a deflection pattern with a fast, stable beam velocity (such as Fig. 4–16a) is desirable, as it will approximate a uniform T_o over the target surface.

We also see that ψ converges towards a limit, which represents the interaction between heat deposition and heat transport. This can be explained by returning to the analytical solution for a semi-infinite solid, where Fig. 4–17 shows that the heat is contained within a layer of thickness $L_{th} \propto v^{-1/2}$. Similarly, in Sec. 3.2.4, we saw that the amount of heat deposited during beam translation is $(1 - \eta_{power})U_b I_b / (\sqrt{2\pi}\sigma_y v_x)$. This shows that with increasing v , the volume of heated material decreases according to $v^{-1/2}$ while the amount of deposited heat decreases as v^{-1} . Therefore, despite the small amount of energy deposited at $v = 800 \text{ cm s}^{-1}$, if T_o is high enough, we can achieve appreciable evaporation since the thermal mass which is heated is small.

From an operations perspective, imagine we require a $\psi = 0.1$ for the beam parameters of Fig 4–28. At $v = 50 \text{ cm s}^{-1}$, this occurs at $\approx 650 \text{ K}$, requiring an energy flux of 139.5 J cm^{-2} . Since the net power into the target is fixed, the deflection pattern must cover a small area.

Conversely, if the deflection pattern and crucible are designed such that $T_o = 1570 \text{ K}$, we can achieve $\psi = 0.1$ by depositing 8.7 J cm^{-1} at $v = 800 \text{ cm s}^{-1}$. This allows for a much larger evaporating area, and thus a higher net evaporation

rates. In both cases, the proportion of beam energy lost to local conduction is the same ($0.9*q_{beam}$), but we are gaining in *net* evaporation since the periodically heated thermal mass is much smaller due to L_{th} .

The analysis presented is a simplification of true EB-PVD, as it only considers 1^D heat conduction with temperature-independent thermophysical material parameters. Despite the simplification, it does demonstrate the interplay between beam speed, power density, and material parameters at the local level. Also, by analysing the evaporation rate as a function of T_o , we can appreciate the effects of crucible design and deflection pattern in establishing pseudo steady-state temperature profiles within the target. The dependence of evaporation on T_o demonstrates the importance of both global and local heat transfer mechanisms.

Despite over-simplifying the heating processes, we can make some general statements regarding EB-PVD. First, the maximum surface temperature will reach a ceiling as q_{beam} approaches q_{vap} . Prior to that, conduction and radiation will dominate, resulting in no evaporation. This demonstrates why high power density axial electron beam guns are preferred when evaporating refractory materials such as YSZ, which require an evaporation temperature of 3500 K. [6]

We also see that the local evaporation rate is a function of the global temperature, T_o and thus constant evaporation rates require constant temperature profiles within the target. This point will be re-visited when we examine the multi-target evaporation process called co-evaporation. The strong interdependence between T_o , deflection speed and beam focus demonstrate that the evaporation process must

consider the global (crucible and deflection pattern) as well as the local (beam focus, deflection speed) system parameters.

Finally, for a given material, the transient thermal conduction properties can be roughly understood by examining L_{th} , as it will capture the material parameters via $\alpha = \kappa/(\rho c_p)$ and the beam parameters via $\tau = 2.355\sigma/v$. The importance of σ and v at the local scale should be considered in the context of total deposited energy flux against the depth of heat propagation.

Although the analysis concerned an electron beam scanned over the target surface, a similar analysis can be performed for a pulsed beam as they both concern transient heating. In that case, the depth of electron penetration S should be considered as well as the radial power density distribution, requiring a 2^D solver.

Future Modelling work

Although the results of the preceding section were illustrative, they do not capture the entire EB-PVD process. Firstly, a 1^D heat profile was chosen, despite the Gaussian power density distribution in the $x - y$ plane. Also, it was shown that the electron beam heat is distributed over a volume defined by the electron range, S . For a beam at 60kV on Ni, $S \approx 9 \mu m$. As a comparison, for $v = 800 \text{ cm s}^{-1}$ and FWHM = 950 μm , $L_{th} = 41 \mu m$. Thus, the 1^D results neglect the full 3^D beam power density distribution.

Most importantly, the assumption that thermal conductivity and heat capacity are constant functions of temperature is incorrect. Specifically, as the target undergoes a phase change from solid to liquid, the material will absorb

the latent heat of melting. More importantly, as the material transforms into a liquid, local convective heat transfer will be activated according to buoyancy and Marangoni forces. This will increase the effective thermal conductivity, [37] and heat transport away from the beam spot will be greater. In turn, this will reduce the surface temperature and evaporation rate. These class of problems are generally referred to as Stefans problem, as they include discontinuities in κ , c_p and the absorption of latent heat.

Although further development of the e^- -beam heating model was not pursued, the analysis of scanned electron beam falls into the same class as a pulsed electron beam, which can both be defined as transient heating problems. In either case, `pdepe` can be used for analysis, as it can be expanded to 2^D and permits discontinuities at interfaces provided that a mesh point is placed at each interface. [40]

CHAPTER 5 Vapour Generation

5.1 Electron Beam Evaporation

As we trace the EB-PVD coating process from vacuum generation to electron beam emission to electron beam heating, we arrive at the final destination: vapour generation and condensation. In the previous section, evaporation was analysed as a heat loss mechanism, but this section will assume evaporation is occurring and analyse the resulting coating dynamics.

EB-PVD is used to deposit coatings of a wide variety of materials, from metals to ceramics to semiconductors. Axial EB-PVD is unique amongst coating technologies because of the combined high power density and high net power compared to other Physical Vapor Deposition (PVD) techniques such as resistive boat heating, induction evaporation, sputtering, transverse EB-PVD and Pulsed Laser Deposition (PLD). With the addition of high voltage power supplies, X-Ray shielding, electron optics and multiple high vacuum sub-chambers, axial EB-PVD is a capital intensive coating process occupying a unique space in the PVD domain. Because of the high net power, commonly in excess of 60kW, axial EB-PVD can achieve the highest possible deposition rates of any PVD process. [8]

Because of the high power density, axial EB-PVD is the preferred method for evaporating refractory materials such as YSZ since the process energy is delivered directly onto the evaporating surface. This allows the evaporating surface to

be contained within an autogenous molten skull. This self-contained geometry minimizes crucible contamination as the vapour emitting surface of YSZ will reach temperatures in excess of 3,000 °C for appreciable evaporation rates.

In the following section, the equations and considerations governing the evaporation and deposition rate of an evaporation source will be presented. The evaporation rate, commonly defined in units of $[\text{g cm}^{-2} \text{ s}^{-1}]$ is a function of the surface temperature and thermophysical material properties and represents the amount of vapour leaving the target. Conversely, the deposition rate $[\text{cm s}^{-1}]$ represents the condensation rate at the substrate and is a function of the evaporation rate as well as geometry. Additional sections discuss the phenomenon of melt spitting and oxide evaporation as they pertain to axial EB-PVD. This section ignores how the surface has achieved its temperature, as those issues are addressed in the previous chapter.

5.2 Vapour Generation

The evaporation rate is exponentially dependent on temperature, which was shown to not be single-valued over the target surface during focused e^- beam evaporation. Thus, the following section serves as a basic introduction to the process of evaporation, demonstrating key parameters, but does not profess to predict the evaporation rate for a given set of operating parameters. Even when these predictions are made, sophisticated numerical models are limited by the accuracy of the material and beam parameters, which are extremely difficult to predict given the extreme temperature and heat involved.

5.2.1 Evaporation Theory

The evaporation rate, or Langmuir equation, is derived under the following assumptions, which are the foundations of the kinetic theory of gases:[13]

- Large assembly of atoms/molecules treated as elastic spheres with separation much greater than diameter
- Random motion of spheres
- No interaction forces between molecules except during collisions
- Particles assume Maxwell-Boltzman energy distribution

Thus, the theory developed below does not account for the ionization effects (i.e. plasma processes). The complete multi-component evaporation rate, or Langmuir equation, is given by:

$$\begin{aligned}
 J_i &= \alpha^{Lang} \sqrt{\frac{M_i}{2\pi RT}} (\gamma_i X_i) (p_i(T) - p_i^*) \\
 &= \alpha^{Lang} * 5.834 * 10^{-2} \sqrt{\frac{M_i}{T}} (\gamma_i X_i) (p_i(T) - p_i^*)
 \end{aligned}
 \tag{5.1}$$

where J_i [g cm⁻² s⁻¹] is the i^{th} component evaporation flux, α_i^{Lang} is the evaporation coefficient, M_i [g mol⁻¹] is the molar mass, T [K] is the absolute temperature, γ_i is the activity coefficient, X_i is the mole fraction, $p_i(T)$ [Torr] is the equilibrium vapour pressure and p_i^* [Torr] is the hydrostatic vapour pressure.

The difference between the equilibrium and hydrostatic pressure results from the return flux of particles which elastically collide near the evaporating surface and reintegrate back into the liquid. Thus, this factor will become prominent

in regions of high evaporation rate, such as near the beam spot. This difference sometimes motivates increasing the background pressure, ($P_{chamber} > 10^{-2}$ Torr) in order to suppress the volatilization of alloy components (e.g. Al, Cr) during melting of multi-component superalloys. [41]

The evaporation coefficient, α^{Lang} represents the ratio between the observed and theoretical maximum evaporation rate, with a value between 0 and 1. It depends on the internal degrees of freedom and symmetry of the evaporant molecules, with metallic species having a theoretical maximum of 1, while water has a value of 0.045. [41] α^{Lang} is also a function of the cleanliness of the evaporant surface, as an impurity film will modify the surface kinetics. For example, it has been observed that during Be evaporation, a chemisorbed layer of oxygen will reduce α^{Lang} from 1 to 0.02 with a corresponding reduction in evaporation rate. [13]

Pure Element Evaporation

As the simplest evaporation scenario, consider the following:

- Pure Element: $\gamma_i X_i = 1$
- Negligible hydrostatic pressure: implying high vacuum and low evaporation rates.
- Clean, monotomic vapor, $\alpha = 1$

Under the above assumptions, Eq. 5.1 reduces to:

$$J = 5.834 * 10^{-2} \sqrt{\frac{M}{T}} p(T) \tag{5.2}$$

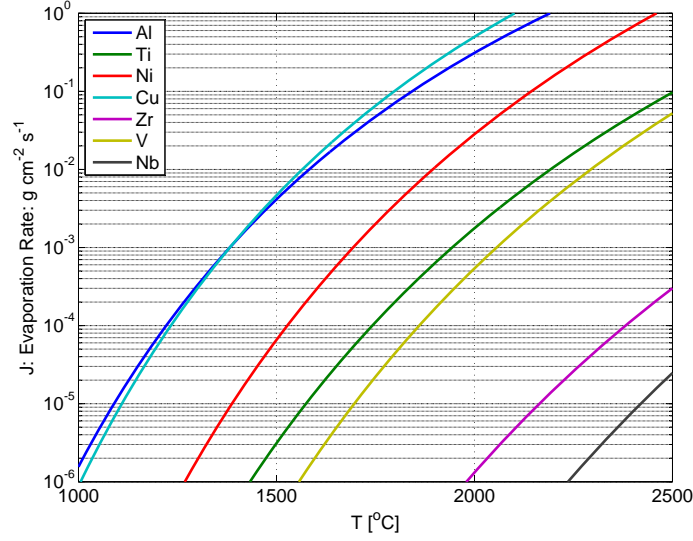


Figure 5–1: Evaporation Rate for common elements, calculated according to Eq. 5.2, 5.3 and material parameters from Smithells [1]

The temperature-dependent vapour pressure can be calculated using the Clausius-Clapyron relationship:

$$\log(p) = -\frac{A}{T} + B + C\log(T) + 10^{-3}DT \quad (5.3)$$

Where A, B, C, D are thermophysical constants found in appropriate references. [1] When evaporating at $p \approx 10^{-2}$ mbar, $J \approx 10^{-4} \text{ g cm}^{-2}\text{s}^{-1}$ which is recognized as a evaporation rate which minimizes spitting. The evaporation rate of some common elements is shown in Fig. 5–1.

In all cases, the evaporation rate is *exponentially* dependent on temperature, via Eq. 5.3. As seen in Chapter 4, the interplay between thermal diffusivity, power density and vapour pressure will define the local superheating of the e^- beam spot. Also, the heat of vaporization will set an upper limit on the surface temperature.

Alloy Evaporation

As shown in the generalized Langmuir equation, components of an alloy evaporate similar to their pure state, with the addition of the chemical activity coefficient γ_i , which reflect deviations from Raoult's Law. Since the constituents of the alloy will not have identical vapour pressures, the composition of the target will not match the composition of the vapour.

Positive deviations from Raoult's Law ($\gamma_i > 1$) indicate a weaker attractive force between alloy components than in the pure phase, and thus the i^{th} component will evaporate more easily in the alloy. Conversely, $\gamma_i < 1$ indicates a stronger attractive force between alloy components and a reduced evaporation rate.

For example, consider the evaporation Grade 5 titanium alloy, with a composition of Ti- 6wt% Al- 4wt% V. As shown in Fig. 5-1, the vapour pressure of pure Al is significantly higher than both Ti and V. Experiments have shown that both Ti and V behaves as an ideal solution ($\gamma_{Ti,V} = 1$). [6] Because V has the lowest vapour pressure and is an ideal solute, it will behave similarly to Ti and will be ignored in the following example.

Using the thermochemical database software FactSage[®] [42], we can extrapolate γ_{Al} into the liquid phase for the Al-Ti system as a function of temperature and weight fraction. The discrete values of γ_{Al} have been combined with Eq. 5.1 and the resulting alloy evaporation rate curves for the Ti-Al system is shown in Fig: 5-2.

The evaporation rate of Ti in the alloy is nearly unaffected, which is expected considering the ideal solution assumption ($J_{Ti} = 1 * (1 - X_{Al})J_{Ti-pure}$). More

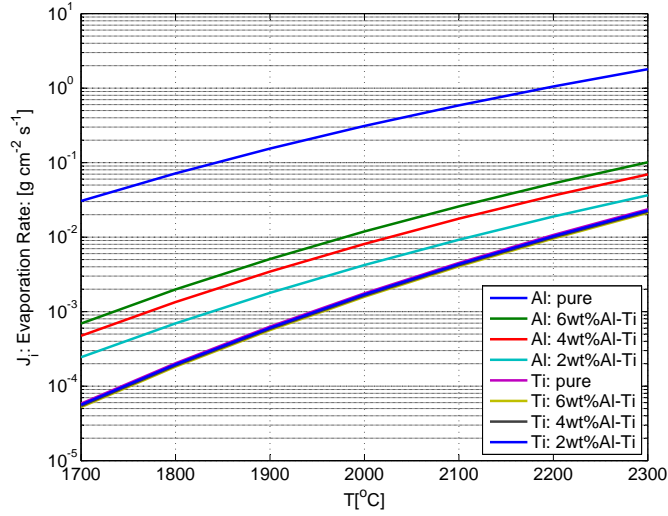


Figure 5-2: Evaporation rate of Ti-Al system at different Al concentrations. γ_{Al} was calculated using FactSage FTLite database [42]

interestingly, we see that $J_{Al-alloy} \ll J_{Al-pure}$, which implies an increased attractive forces between Ti and Al compared to pure Al. Also, J_{Al} decreases with decreasing Al content.

To better understand the alloy evaporation evolution, the vapour ratio (J_{Al}/J_{Ti}) and the net evaporation ($J_{Al} + J_{Ti}$) as a function of temperature are shown in Fig. 5-3.

Fig. 5-3 shows that, for any given temperature, J_{Al} dominates the vapour flux composition, proving that the target and vapour composition will not match. Fig. 5-3 also shows that the evaporation rate decreases as Al is depleted. This implies that the evaporation rate of alloys is coupled to the diffusion and convection kinetics within the target.

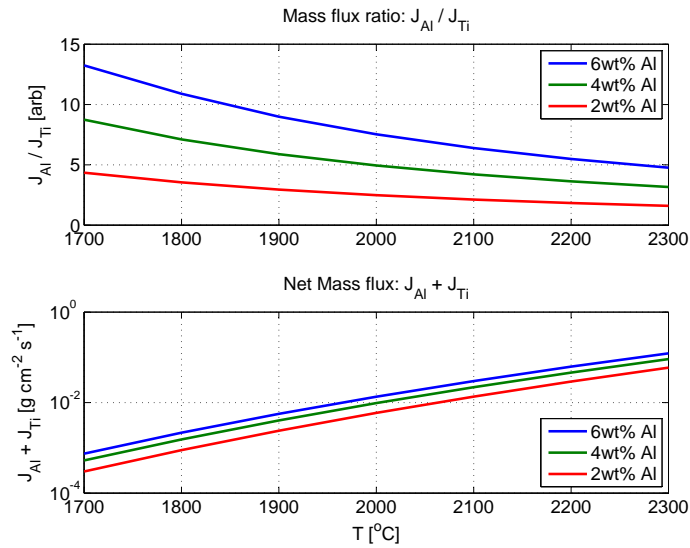


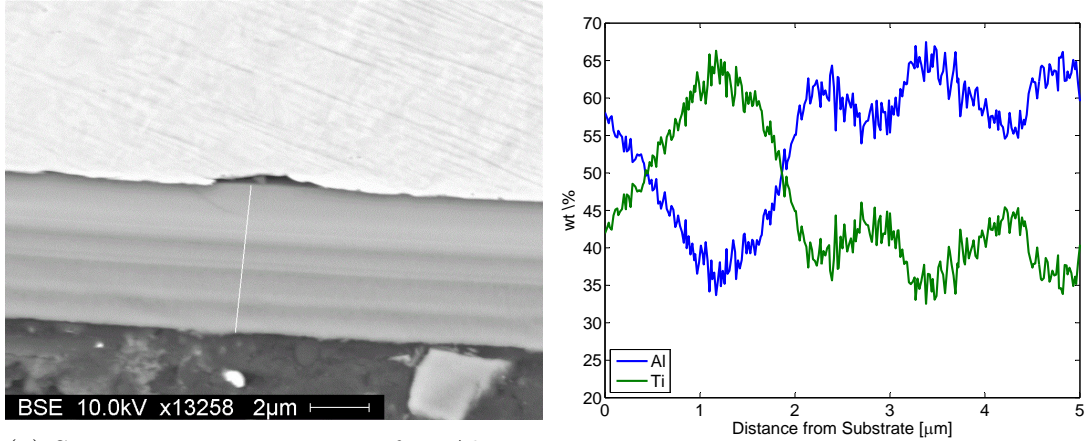
Figure 5-3: Evaporation ratio and net flux of Ti-Al System

Another implication of Fig. 5-3 is that with increased surface temperature, Al voltization is reduced. This is a well known fact within the Ti e-beam melting community, where spot size and scan speed are seen as critical processing parameters. [7]

As an example, a 20 minute EB-PVD was performed at McGill whereby the center of the scan pattern was moved four times. An SEM cross section and EDS line scan of the coating is presented in Fig. 5-4.

The EDS line scan shows that the Al content of the coating decreases as it is depleted from the melt pool. Moving the scan pattern center increases the Al content in the melt pool and the result is an increase Al flux which manifests itself as an Al enrichment in the film.

In large scale industrial applications, such as coating Ti64 on silicon carbide fibres [43] or YSZ thermal barrier coatings [44, 45] the source pool is constantly



(a) SEM cross-section image of Ti-Al coating on B5. Linescan begins at substrate

(b) weight % of Al and Ti through coating from SEM-EDS

Figure 5-4: SEM cross section of B5-Ti64 evaporation. The scan pattern center was moved during evaporation, resulting in modulation of Al and Ti content. Vanadium was not registered in the EDS linescan

fed with additional material. After a certain ‘run-in’ time, whereby the volatile components are depleted from the melt, a steady state is formed with the feed composition matching the vapour composition (via conservation of mass). [46] Often, a ‘starter button’ is used to minimize the run-in period and establish an appropriate melt pool composition.

Even with a continuous material feed, chemical inhomogeneity in the vapour can occur. While coating SiC fibres with Ti64, 3M researchers observed that the central portion of the vapour plume was depleted in Al via the Al gradient along the substrate width. [43] It was suggested that during vapour transport, the higher mobility of Al (compared to Ti and V) results in diffusion of the Al vapour molecules towards the edge of the vapour plume. Similarly, the temperature gradients on the surface causes titanium and vanadium to be evaporated over

smaller areas compared to aluminium. [43] This was compensated with careful process development, including feedstock artificially enriched in Al.

Forming alloy coatings using a feeding mechanism is referred to as single source evaporation. The advantages are better material usage efficiency (due to smaller substrate-evaporant distance) as well as better robustness against beam power fluctuations. [47] Unfortunately, single-source evaporation does not lend itself to materials exploration, since the above examples demonstrate that new compositions require significant target/ingot development and empirically derived evaporation routines.

Although single source evaporation is an important industrial process due to the the high productivity, stringent requirements exists on the coating equipment. For instance, in coating MCrAlY onto turbine blades, Lammerman defines the following equipment requirements: [48]

- Beam current variation $< 0.5\%$
- Accelerating voltage regulation $< 0.5\%$
- Beam power density regulation/focussing $< 0.1\%$
- Melt pool level regulation $< \pm 1\text{mm}$
- Material Feed regulation $< 0.05\text{mm}/\text{min}$

As well as equipment stability, the thermal conditions must be stabilized as well. Specifically, the crucible cooling water must reach steady state and the melt pool/crucible interface must be stabilized. This was seen in Sec. 4.6, where the evaporation was seen to be a strong function of T_o . Also, as condensates gather on the chamber walls, the thermal radiation system will evolve and will need to

be compensated. If the processing parameters are held within the tolerances listed above, the tolerances of the volatile components in the melt can be: Cr- $20\pm 2\%$, Al- $10\pm 2\%$ and Y- $0.2\pm 0.1\%$. [48]

An alternative method of forming alloyed coatings is using multiple vapour sources in a process called co-evaporation, which will be discussed in a later section.

In summary, whether evaporating from a single or multiple targets, alloy evaporation is more challenging than elemental evaporation. This is largely due to the exponential temperature-dependence of the evaporation rate and hardware stability.

5.3 Deposition Rate

The Langmuir equation determines the local evaporation rate at the target surface, while further manipulation is needed to determine the deposition rate at the substrate. First, it follows that the total evaporated mass, M_e is given by:

$$M_e = \int_{t_0} \int_{A_e} J_{vap}(\mathbf{x}, t) dA_e dt \quad (5.4)$$

where A_e is the evaporant surface, t is the deposition time and J_{vap} is the evaporation rate. In axial EB-PVD, J_e will *not* be single valued over the evaporant surface due to the focused nature of the e⁻ beam. Even with highly advanced numerical models, accurate prediction of the surface temperature (and thus evaporation rate) in axial EB-PVD is challenging because of 3^D thermo-fluid dynamics which include Maragoni and buoyancy convection, thermal contact resistances and vapor

recoil forces. [49] Nevertheless, understanding the vapour distribution of a uniform temperature vapour source will elucidate the factors at play.

Consider a planar substrate parallel to the vapor emitting surface, as shown in Fig. 5–5, where h is the evaporant/substrate height and l is radial distance along the substrate from the evaporant center.

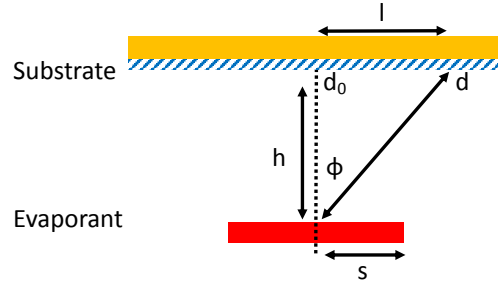


Figure 5–5: Configuration of source and substrate geometry and definitions

The thickness distribution from a small area vapor source dA_e is given by:[13]

$$d = \frac{M_e}{\pi\rho h^2} * \frac{1}{(1 + (l/h)^2)^2} \quad (5.5)$$

where d is the thickness and M_e is the evaporated mass defined by Eq. 5.4. We can define d_0 , which is the thickness directly above the evaporant (ie $l = 0$) such that, for the small-area source:

$$\frac{d}{d_0} = \frac{1}{(1 + (l/h)^2)^2} \quad (5.6)$$

By appropriate integration of Eq. 5.5, the thickness distribution of a thin ring-type source of radius s_{ring} , is given by

$$d = \frac{M_e}{\pi\rho h^2} * \frac{1 + (l/h)^2 + (s_{ring}/h)^2}{([(1 - (l/h)^2 + (s_{ring}/h)^2]^2 + 4(l/h)^2)^{3/2}} \quad (5.7)$$

Finally, if we consider a circular-disk source of radius s_{disk} , the thickness distribution is given by:

$$d = \frac{M_e}{\pi\rho h^2} * \frac{1}{2} * \left[1 - \frac{1 + (l/h)^2 - (s_{disk}/h)^2}{\sqrt{[(1 - (l/h)^2 + (s_{disk}/h)^2]^2 + 4(l/h)^2}} \right] \quad (5.8)$$

where the thickness directly above the source, and d_0 is given by:

$$d_0 = \frac{M_e}{\pi\rho h^2} * \frac{1}{1 + (s_{disk}/h)^2}. \quad (5.9)$$

The most uniform distribution of evaporated material is achieved with a ring-type source, where the ratio of the ring diameter s to the substrate height h is equal to $s/h \approx 0.75$. [13]

For a circular source, enlarging the source radius s does not significantly improve the vapour distribution. The advantage of using a large evaporation surface is high deposition rate, which manifests itself in the factor M_e .

In the case of axial EB-PVD, many deviations from the idealized emission laws given above occur, which are dependent on the beam parameters, such as deflection speed, power density and spot size. Thus, determining the coating rate in axial EB-PVD is significantly more challenging than resistively heated boats or effusion cells.

5.3.1 Co-Evaporation

Co-evaporation is a PVD technique whereby multiple vapour sources are operated simultaneously, using one or more electron beams, as shown in Fig 5–6.[50, 51, 52] The chemistry of the coating is defined by the individual deposition rates of each vapour source. [53, 51, 54] This technique is especially attractive

when prototyping new coating chemistries or depositing alloys which have constituent vapour pressure differences exceeding 1000. [15]

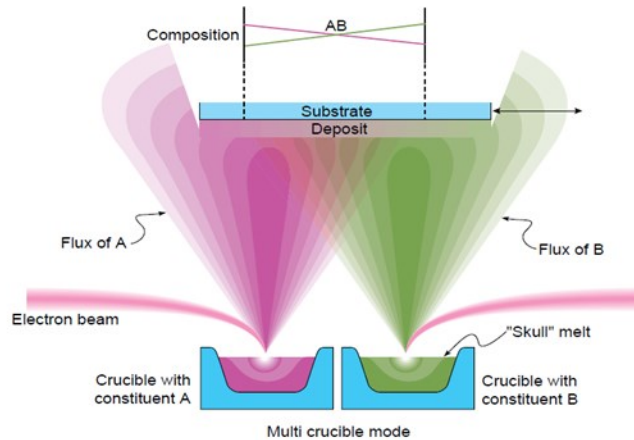


Figure 5–6: Alloy Deposition using co-evaporation [55]

In practice, co-evaporation is a challenging technological process. Firstly, due to the directionality of the vapour plumes ($\cos^n(\theta)$), only a small region of the condensation plane will have the target composition. Substrate translation or rotation can enhance the vapour mixing, extending the region of homogeneous chemistry. [55]

Co-evaporation requires stable vaporization rates of each source in order to produce coatings with adequate alloy constancy. [15, 47] This requirement can be difficult due to the exponential temperature dependence of the evaporation rate. For instance, when evaporating nickel for Fe-Ni films at $T_{surf} = 1900$ K, Eq. 5.1 can be used to show that:

$$\frac{\delta X_{Ni}}{X_{Ni}} = 20 \frac{\delta T_{surf-Ni}}{T_{surf-Ni}} \quad (5.10)$$

Thus, a temperature fluctuation of 10 K changes the nickel fraction by 10%. Accurate co-evaporation must possess temperature stability, implying that the heat losses (conduction and radiation) and heat sources (e^- beam power) are stable throughout deposition. The gun (or guns) must also have little or no arcing, as this will momentarily interrupt the emission of vapour from one of the sources.

As suggested by Fig. 5–6, the deposition gradient will result in compositional gradients. The slopes in composition can be reduced by placing the vapour sources in close proximity to each other, but measures must be taken to prevent vapour source cross contamination. The effect on the compositional gradient as a function of distance between vapour source d_s , is shown in Fig. 5–7a. This plot demonstrates that when the sources are placed in close proximity, the variation in composition (represented by the thickness gradient) will be small. If the vapour sources are placed far apart, the area of small gradient for one vapour source will result in high gradients in the other. Thus, comparative gradients in thickness is a measure of the chemical inhomogeneity of the co-evaporated coating.

Another practical solution is increasing the distance between the vapour sources and substrate (h), as shown in Fig. 5–7b. As was discussed in Section 5.3, increasing h reduces the deposition rate, increasing the specific collision rate ratio of gas and vapour molecules and introducing more residual contamination into the coating. The plots in Fig. 5–7 demonstrate a fundamental challenge surrounding co-evaporation: locations where one constituent deposition rate is flat will have a rapidly varying deposition rate of the other species.

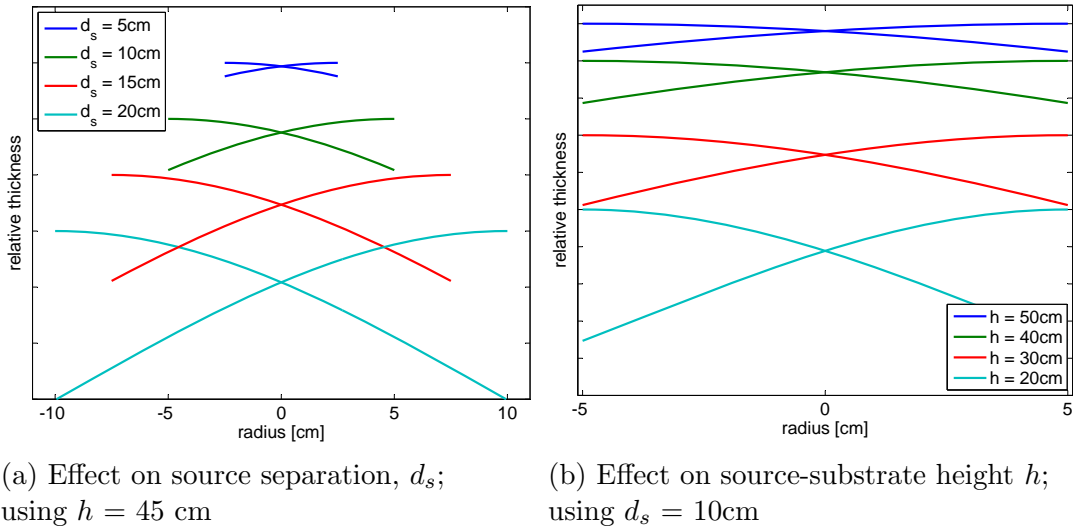


Figure 5-7: Effect of source separation d_s and source-substrate height h on the compositional gradient during co-evaporation, calculated using Eq. 5.8, using 2.5 cm source radii

Quartz deposition rate monitors focused on the individual vapour sources are often employed as a feedback signal to regulate beam power. Also, using high evaporation rates will tend to stabilize the evaporation rate. [56]

Cu and Ni Evaporation

In order to investigate the co-deposition technique, an experiment was performed whereby Cu and Ni were sequentially evaporated using the deflection coils and a continuous beam onto substrates D3, D4 and D5. Copper and nickel were chosen because of their availability, as well as their complete miscibility and similar vapour pressure curves. The 4" targets were cut in half, and placed next to each other above a ZrO_2 thermal insulator. Thermocouples were attached to each side of the targets, with the final configuration shown in Fig. 5-8.

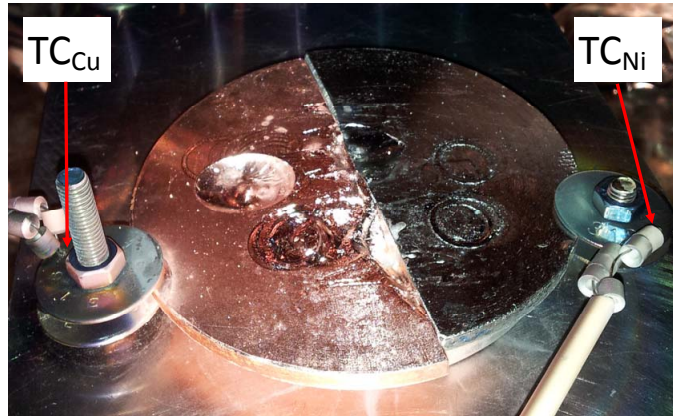


Figure 5–8: Plain view of 4” target configuration used during Cu-Ni Experiments, showing location and configuration of thermocouples

Prior to evaporation, the target was pre-heated for 10 minutes by ramping to a beam current of 20 mA using a defocused beam. When possible, the evaporation proceeded for 3 minutes, using a 20 mA/60 kV beam power, and a focused beam at $w_b = 840$ mA. The target-substrate separation was 96 mm, and the substrate was centred along the Cu/Ni interface.

The deflection pattern parameters are defined in Table 5–1. During evaporation, the center of the deflection circle was shifted 3.6 cm over a 200 mS period, such that the dwell time on the Ni and Cu could be varied. For instance, during the deposition onto substrate D3, 160 mS were spent on Ni and 40 mS were spent on Cu, resulting in a 20% Cu duty cycle.

The D5 evaporation was aborted after 2 minutes due to molten Ni flow exposing the ZrO_2 thermal insulator. The Cu duty cycle and the corresponding XPS atomic percentage results for D3, D4 and D5 are shown in Table 5–2.

Axis	u	v
Type	Sine	Sine
Amplitude [V]	1.4	0.6
Phase [$^\circ$]	0	90
f [Hz]	50	50

Table 5–1: Cu-Ni deflection pattern that was used during D3, D4, D5 evaporation.

	Cu Duty Cycle	Cu XPS atomic [%]
D3	20%	$95 \pm 5\%$
D4	10%	$90 \pm 5\%$
D5	5%	$70 \pm 5\%$

Table 5–2: Cu-Ni co-evaporation parameters during D3, D4, D5 evaporation. XPS results are uncalibrated, and represent the results after 10s ion milling in order to remove carbon and oxidation layer.

The results demonstrate the expected result that longer dwell times on Cu result in a higher Cu coating concentration. In all cases, the Ni content tended to increase with increasing ion milling depth, with the margin represented as an uncertainty in the XPS atomic percent.

Although the results of Table 5–2 meet qualitative expectations, they also demonstrate the importance of temperature stability. Fig 5–9 shows the thermocouple response of the Cu and Ni targets during each deposition.

As shown in Fig. 5–8, the thermocouples are far from the evaporation spot. The results of Fig. 5–9 show that only TC_{Ni} for D3 and D4 have stabilized, whereas the other measurements show increasing temperature with deposition time. This explains the variation of Cu and Ni with depth, as the relative evaporation rate of Cu and Ni will change as the deposition proceeds. The change is a function of the thermophysical material parameters and the heat transfer

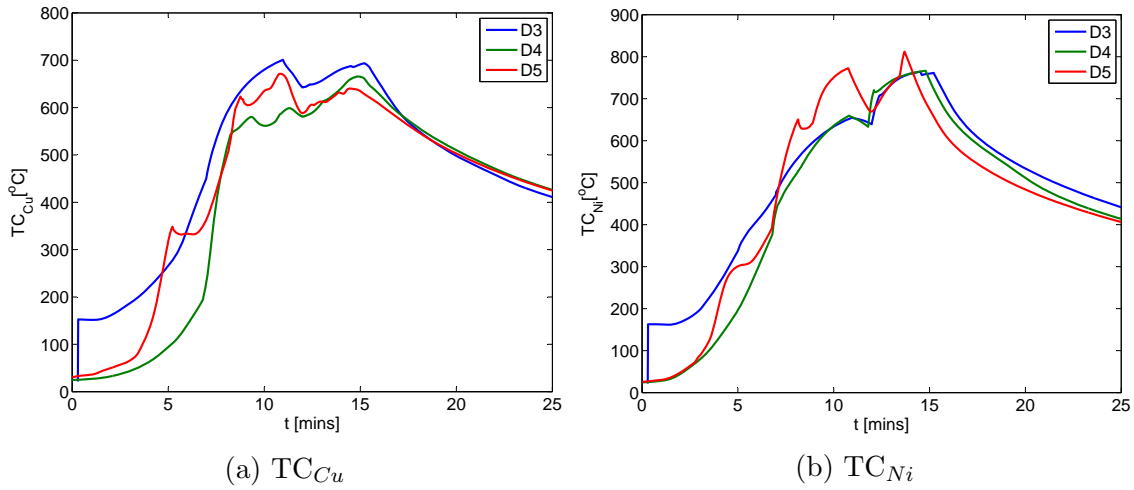


Figure 5-9: Thermocouple response during Cu-Ni Co-deposition. The dip at approximately 12 minutes represents the transition from pre-heat to evaporation

characteristics, which are not equivalent for Ni and Cu. Longer evaporation times were attempted in order to stabilize the temperature response, but in all cases, the deposition became unstable with significant liquid Cu flow, resulting in the destruction of a Cu/Ni target.

These results highlight the challenges associated with co-evaporation, namely, that coating chemistry is a function of the the heat transfer characteristics. The thermocouple response of Fig. 5-9 demonstrate that our crude target holder is not up to the task. The advantages of water cooled crucibles are thus apparent, as active cooling will established a *stabilized* temperature gradient between the evaporating surface and the target holder.

5.3.2 Non-ideal Deposition Rates and Distribution

In the previous section, equations for evaporation rate and distributions were described. Not surprisingly, these laws are idealized, and significant deviations

will occur with increasing evaporation rates. The first description of these non-idealities was given by Smith in 1969. [56]

One such deviation occurs near the evaporant surface, where the vapour density is high enough to depart from molecular flow conditions, i.e. a significant number of vapour-vapour collisions occur. The result is a viscous region extending some distance above the evaporant, as shown in Fig. 5–10.

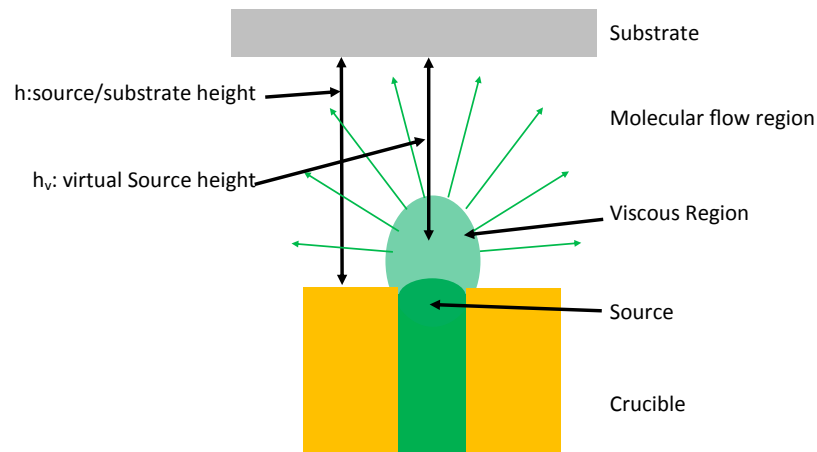


Figure 5–10: Viscous and molecular flow regions during high rate EB-PVD [56]

Molecules will travel collision-free from the edge of the viscous cloud, resulting in a modified vapour distribution. The condensing molecules will be ‘seen’ as coming from a source at an empirically calculated distance h_v , where $h_v < h$. [56] Also, areas within the chamber that do not have line-of-sight with the evaporating surface will become coated.

Since $h_v < h$, the viscous cloud essentially focus the vapour plume along the center line, as shown in Fig. 5–7b. The phenomenon can be understood as follows: an atom leaving the surface at a strongly off-normal angle will be more likely to

collide with another evaporant atom with upward velocity as the evaporation rate increases. The outcome is that the off-normal atoms acquire a more upward velocity, resulting in vapour cloud focusing, in a process called vapour beaming. [6] Discrete Monte-Carlo simulations of the vapour molecule paths have shown that the level of beaming is dependent on the mean free path of the vapour molecules and the evaporant surface area A_e . [55]

The vapour distribution can also be modified if residual chamber pressure is comparable to the vapour pressure of the evaporating species. [57] This is seen during reactive evaporation of materials such as YSZ in a O_2/Ar atmosphere. [55].

The formation of a viscous cloud has implications for the evaporation rate as well. When evaporating a low vapour-pressure material, such as aluminum, high rates can be achieved by defocusing the beam. This occurs since, at the beam hot-spot, the local vapour pressure becomes very high, the vapour flow turns from molecular(no collisions) to viscous(many collisions). A sizeable fraction of the vapour is re-condensed, thus reducing the net evaporation rate. As an example, consider Fig 5–11 which was taken from a transverse e^- beam gun operating manual. [14]

Fig. 5–11 shows that the use of pole extensions defocuses the beam. At low input powers, a focused beam has a higher evaporation rate than a defocused beam for a given input power. But as the power increases, the local re-condensation rate plateaus the deposition rate, while the defocused beam increases with increasing power, thus proving that the formation of the viscous cloud is a function of the *local* evaporation rate.

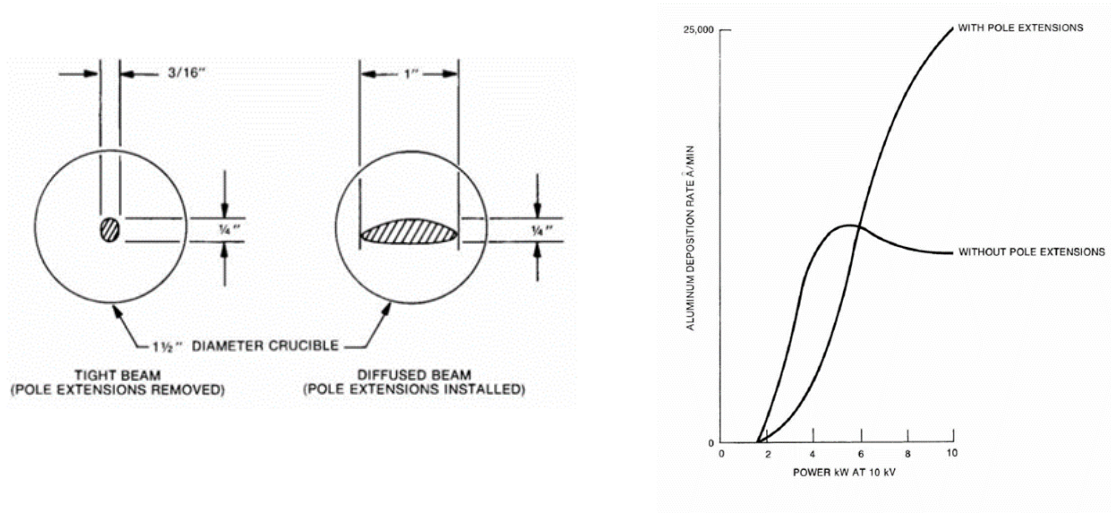


Figure 5-11: Evaporation rate of aluminium using 10kV transverse gun as function of beam focussing [14]

5.3.3 Spitting

With a focused axial e^- beam, high rates of local evaporation occur. In Sec 4.6, we saw that it is possible to transform nearly all the beam energy into vapour using a slow, focused beam. Although attractive, excessive evaporation can be detrimental to the coating process, as the vapour which emerges exerts a recoil force on the molten evaporant. This causes a bulge in the beam spot area, Δh which increases with increasing evaporation rate and decreasing density according to: [58]

$$\Delta h = 5 * 10^{-4} * \frac{p_s}{\rho} \quad (5.11)$$

where p_s [mbar] is the saturated vapour pressure, ρ [$g\ cm^{-3}$] is the density and Δh [mm] is the bulge depth. As the bulge grows inwards, a critical depth is reached

where the molten metal covers and uncovers the bulge, resulting in splashing. Splashing causes the ejection of molten droplets, which can impact the substrate, in a process called spitting. The result of condensed Ni spits on the substrate C3 is shown in Fig. 5–12.

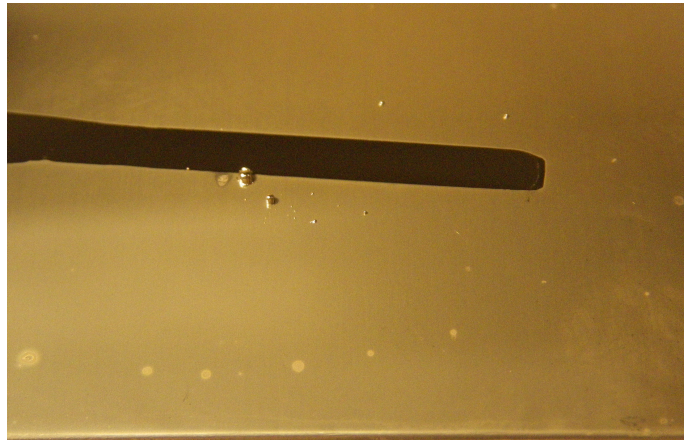


Figure 5–12: Plain view of molten particles condensed onto substrate C3 during nickel evaporation

Spitting depends on the shape of the bulge as well as the physical properties of the evaporant via surface tension. Typically, the propensity of a target to spit increases with increasing accelerating voltage, but can be offset by using higher deflection speeds as well as a defocused beam, both of which will reduce the temperature gradients. [58] In the case of evaporation of YSZ, the viscosity of the liquid is similar to water, requiring carefully chosen deflection patterns and beam focus. [59] Observations of the YSZ melt pool with a CCD camera at Lawrence Livermore National Lab showed that YSZ exhibits a very low viscosity, low density and exceptionally high surface tension, making the pool sensitive to spitting. [60] During rod fed, water-cooled high-rate axial EB-PVD (eg: EB-PVD of YSZ),

skilled operators vigilantly observe the melt pool through a stroboscope. The deflection pattern is modified in real time to ensure that the melt pool is wetting the crucible wall. [55, 50, 59] This is done such that the liquid/crucible interface stabilizes the thermal conduction, and thus the evaporation process.

Graper offers some excellent advice for evaporating new materials using transverse guns, with specific mention towards spitting: [31, 61]

- When evaporating dielectrics, slowly increase beam power to evaporation temperature in order to increase conductivity (electrical and thermal) to the point where the surface charge is small
- Select a vapour source with the largest possible volume to area ratio. Avoid evaporating granular or powdered materials
- Use the largest possible crucible volume
- Use largest beam spot while attaining desired deposition rate
- Increase spot size if increased beam power causes spitting or film pinholing.

Depending on crucible design and evaporant, the maximum power of the gun will be defined by what can be dissipated by conduction to the crucible. [31] Exceeding the maximum power at the target causes spitting. This can be seen by examining Table 5-3, which compares the crucible diameter, gun power and deposition rate for a series of axial EB-PVD YSZ coaters.

The correlation between deposition rate, gun power and target diameter should be apparent.

Spitting was experimentally observed during the evaporation of a 4" OD nickel target resting on a thermal spacer. During two separate evaporations (C3

Lab	Target	U_b [kV]	I_b [A]	Deposition Rate [$\mu\text{m min}^{-1}$]	Note
University of Virginia[50]	YSZ [70%] 13 mm OD	60	0.17	2	EB-DVD
Penn State Naval Research lab[16]	YSZ 60 mm OD	18	1.7	3.4	4 gun co-evap
DLR- German Aerospace Center[62]	YSZ 50 mm OD			6-7	
Von Ardenne Angalentechnik[63]	YSZ [60%] 63 mm OD	40	1.4	23	Commercial System
ALD	YSZ 63.5 mm OD	35-40	2.5-3	N/A	Multiple targets

Table 5-3: Technology comparison for different axial EB-PVD systems. [X%] values represent porosity of target

& C7) power, time, deflection pattern and focusing schedules were nominally identical. The difference was that C3 used a ZrO_2 thermal spacer ($\kappa = 2 \text{ W m}^{-1} \text{ K}^{-1}$) while C7 utilized a Al_2O_3 insulator ($\kappa = 35 \text{ W m}^{-1} \text{ K}^{-1}$). The thickness of the resulting coatings were 2.2 and 2.0 μm for C3 and C7 respectively.

After the deposition campaign, coating C3 had significant spits condensed onto the substrate, shown in Fig. 5-12, while C7 had no observable spits. It is suspected that the difference is due to the increased conduction of the Al_2O_3 spacer, which is better at dissipating temperature transients due to the increased conduction. This is corroborated by the larger re-solidified interface between the melt pool and thermal spacer, as shown in Fig. 5-13, implying greater conduction using the Al_2O_3 spacer.



Figure 5-13: Plain view of underside of Ni target post evaporation of substrates C3(ZrO_2 and C7 (Al_2O_3)

Because of the higher conductivity of Al_2O_3 , the molten Ni pool will dissipate heat vertically much better than ZrO_2 . The outcome is that the local temperature does not increase sufficiently to cause spitting, thus resulting in a spit-free deposition.

Although other factors are certainly at play when comparing C3 to C7, it does demonstrate that many considerations must be taken into account in order to prevent spitting.

Spitting can also occur due to voids in the target being heated, which are in a low viscosity environment, resulting in an explosive expansion into the vacuum environment. It can also occur when high-melting-point inclusions (carbides/oxides) acquire a large amount of energy from the beam, vaporizing explosively.[48, 46] Another possibility is ‘running hot’, whereby refractory materials collect on the evaporating surface, reducing the evaporation rate. These impurity related scenarios can be mitigated by using evaporation grade targets and

properly degassing the material before deposition. This was seen while evaporating mill-grade copper, whereby extensive spitting was observed using parameters that do not generally cause spitting for evaporation-grade copper. Thus, ultra-pure materials should be used, with electron beam overflow melting preferred over induction furnace melting.[48]

5.3.4 Oxide Evaporation

Many engineering coatings are ceramics, which require special considerations concerning the stoichiometric compound formation, as well as a beam of charged particles striking an electrical insulator.

Charging

When the electron beam strikes the target, the target becomes part of the the current loop between the cathode to the anode. Metallic targets have high electrical conductivity, resulting in a high conductance path for the return current. Oxides have a low electrical conductivity, making a low conductance path for the return current, with important implications for beam propagation.

As discussed, Back-Scattered Electrons (BSE) and Secondary Electrons (SE) are ejected from the surface of the target, the sum of which depends on the accelerating voltage and angle of incidence. Since electrons are entering and leaving the target surface, the surface can become electron deficient(positive charging) or excessive(negative charging) depending on the difference between the incident and exiting electrons. [22] In Sec. 4.3.1, this was calculated as $\eta_{BSE} = I_{bse}/I_b$. The secondary crossover point, which implies $\eta_{BSE} = 1$, is in the range

of 2-4keV for inorganic materials. Thus, EB-PVD of oxides generally involves negative charging.

Negative charging can result in the formation of a plasma above the insulating target, as electron are decelerated near the surface and their ionization yield increases. An image of a defocused, 60 kV/2 mA beam forming a plasma above Al_2O_3 is shown in Fig 5-14.



Figure 5-14: Plain view of plasma formation due to electron beam charging using a defocused beam on an Al_2O_3 target. The color shown does not match the true color due to CCD distortion.

The brightness of Fig. 5-14 is believed to be due to atomic excitation/relaxation and not blackbody emission since low power is used. The dominant discharge color of Al_2O_3 changes from blue to green above regions of the target that have been melted. It is believed that this change is due to the change in conductivity which occurs within the material, which changes the repulsive field generated from charging. This repulsive field is thus responsible for the mean energy of the ionizing electrons and will define the dominant discharge color.

The charging phenomenon is dynamic and is defined by the material RC time constant, which is related to surface resistivity, dwell time, beam energy, beam current, scan rate and raster pattern and SE/BSE coefficients. In an extreme case, the accumulated charge may cause local electrical breakdown, discharging to ground. In the case of Pulsed Electron-beam Deposition (PED), it has been observed that the electrical surface conductivity of the target is a key parameter during the electron beam ablation of insulating $\text{YBa}_2\text{Cu}_3\text{O}_{7-x}$. [64]

Fortunately, oxide conductivity follows an Arrhenius equation, $\sigma = A_o \exp(-E_{ox}/kT)$. The activation energy for conduction, E_{ox} , depends on defect density, thermal history and sample preparation and is thus rarely well defined. E_{ox} is generally defined as $E_{ox} = E_\mu + E_a$ where E_μ is the activation energy for carrier hopping and E_a is related to the carrier mobility. [65]

From an operational viewpoint, the target should be preheated prior to deposition. Heating will increase the conductivity, allowing for unimpeded beam propagation. Special consideration should be made regarding oxide thermal shock, which can induce cracking or shattering. During the deposition of YSZ, porous targets with 60-70% density are used. [50, 63] These sintered oxide compacts will have a large amount of adsorbed gas. Advanced rod-fed EB-PVD crucibles used for depositing YSZ incorporate a heater in the rod column in order to degas the evaporant prior to deposition.

Dissociation & Oxide growth

One of the challenges of oxide evaporation is dissociation, whereby the oxide will fragment into sub-oxides and primary elements. The products have a tendency

of reacting with the environment, thus making measurements difficult, and leading to wide disagreements in the vaporization characteristics. [66] As an example, consider the evaporation of Al_2O_3 , where the temperature-dependent partial pressures and relative vapour composition is shown in Fig. 5–15.

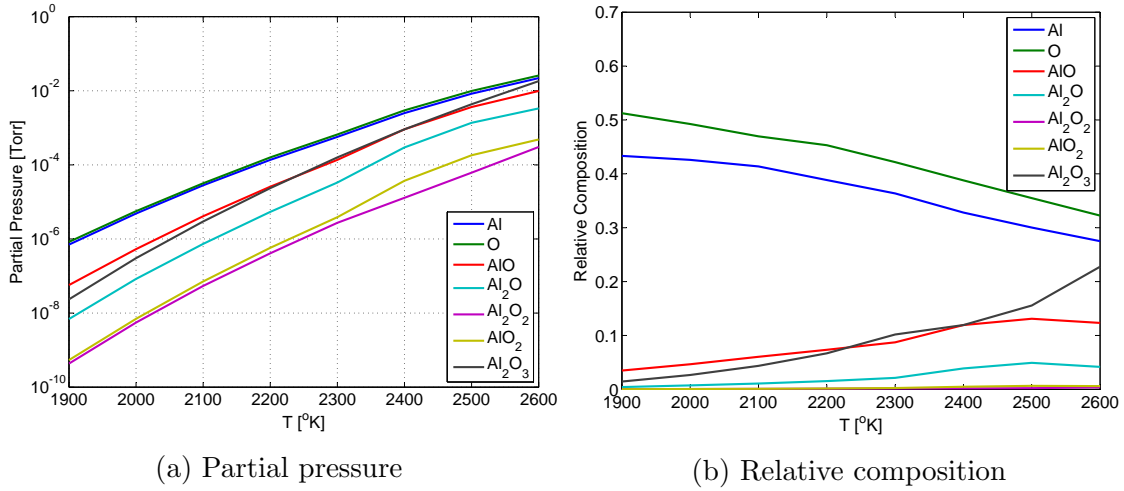


Figure 5–15: Partial pressure and relative composition of Al_2O_3 as a function of temperature [3]

Fig 5–15 thus shows that surface temperature is *one* factor in determining the stoichiometry of the oxide coating. Although Fig. 5–15b suggests that evaporation at a higher temperature enhances the Al_2O_3 emission, we have seen that enhanced evaporation rates can also bring non-idealities, such as the formation of a viscous cloud above the target. This simple example demonstrates the complexity associated with successful oxide deposition. Although the following will focus on oxides, the discussion presented below also applies to carbides, borides and nitrides as well.

A common solution to the dissociation problem is admitting O_2 gas into the vacuum chamber during deposition, in a process called Reactive Evaporation (RE). [67, 68] The oxide formation depends on the impingement rate of metal: oxygen molecules at the substrate surface (ν_{Me}/ν_{O_2}), which was shown in Chapter 2 be proportional to the deposition rate and the partial pressure of O_2 , respectively. [67, 69, 13]

After impinging on the substrate, some of the molecules will be adsorbed, while others will be reflected or desorbed. The ratio between permanently adsorbed molecules and the impingement rate is called the condensation coefficient, α_c , which is temperature dependent. For example, an O molecule evaporated from a Al_2O_3 target will have a temperature of $>2200^\circ K$. Thus, the condensation coefficient represents the ability to equilibrate with the substrate and thus condense. This is similar to the physics dictating the residence time of an adatom, as described in Chapter 2.

Also, if the pressure within the chamber is high, the hot molecules transfer their energy to the cold gas, thus changing the condensation coefficient. As we will see, the temperature (or more specifically energy, kT) of the condensing molecules can have a large effect on the resulting microstructure, thus proving again the importance of the vacuum system.

Generally, the impingement rate of oxygen must exceed that of the metal vapour, while keeping the net pressure low as to not be detrimental to the microstructure. Thus, RE will encounter a ceiling in deposition rate. This restriction

can be circumvented by increasing the metal/oxygen reaction probability by ionizing the gas/vapor mixture in a plasma-enhanced process called Activated Reactive Evaporation (ARE). [70] During deposition, a thin plasma sheath forms on top of the melt due to the high ionization cross-section of the secondary electrons, as shown in Fig. 5-14. Some of these electrons are pulled into the volume between the target and substrate using a biased grid(+20 to +100V), forming an extended plasma between the target and the grid. This plasma increases the yield of the metal: oxygen reaction, and allows for the compound formation and growth process to be separated. ARE allows for high deposition rates of compounds, as the plasma imparts additional energy to the condensing particles, thus increasing the compound reaction rate. In the microelectronics industry, plasma-activated deposition techniques are used to achieve a specific microstructure without increasing the substrate temperature. ARE requires a substrate bias, resulting in further deposition versatility such as pre-deposition plasma etching. Pulsed or RF bias is needed for the deposition of oxides due to the electrically insulating nature of the coating. [71, 72]

Some researchers have found the growth process to be a function of deposition rate, which is not surprising considering that oxide growth is an ordering process, whereby O and Al atoms must find appropriate lattice sites before the next atoms arrive. [66] In the presented work, it is unclear whether the effects of local surface temperature, net evaporation rate and deposition rate were uncoupled.

In summary, the growth process is controlled by the impingement ratio ν_{Me}/ν_{O_2} , the α_c of each species, the net pressure and the substrate material and temperature. [13]

Admitting gas during e⁻beam evaporation is technologically difficult because of the potential for arc discharges within the gun. The advantages of axial e⁻beam is apparent, as the vapour emitting surface and gun can have separate vacuum systems. The first challenge is decoupling the pressure of evaporation chamber from the electron gun. von Ardenne guns used to evaporate YSZ achieve a pressure decoupling of 1000 by incorporating two vacuum sub-chambers along the beam axis, water cooled vacuum constrictions and additional beam focussing lens. [73] Secondly, at the pressure increases, small fluctuations in the gun focus cause significant fluctuations in the evaporation rate and spitting frequency due to gas de/focusing. [74]

Al₂O₃ Evaporation

A series of four Al₂O₃ evaporations were performed in order to gain some insight into the oxide deposition process. For each experiment (C14, C15, C16, D1), a 10 minute pre-heat was performed, followed by a 20 minute deposition at 10 mA/60 kV using a slightly defocussed beam at $w_b=840$ mA. The same target was used for each experiment, with different areas being evaporated during each run. The deflection coil signals are defined in Fig. 5-16. The major distinction to be noted is the 'fast' axis, which was the x axis for C14 and along the y axis in C15,C16,D1. Plots of these patterns are shown in Fig. 5-17, with the corresponding beam speed plot given in Fig. 5-18.

Axis	u	v
Type	Triangular	Triangular
Amplitude [V]	1	0.6
Phase [$^\circ$]	0	90
f [Hz]	10	50

(a) C14

u	v
Triangular	Triangular
1	.5
0	90
50	10

(b) C15, C16, D1

Figure 5–16: Deflection pattern signals $[u, v]$ used during Al_2O_3 evaporation.

The substrate-target height, profilometer thickness and net mass gain over net thickness for each run is given in Table 5–4. The most striking result is the large differences in thickness for the seemingly similar deposition parameters.

	h Height [mm]	Thickness [μm]	Net mass gain/thickness [$\text{g } \mu\text{m}^{-1}$]
C14	90	63	0.0026
C15	90	21	0.0031
C16	107	19	0.0042
D1	72	66	0.0017

Table 5–4: Deposition parameters for Al_2O_3

Let us begin by examining the C14 and C15 depositions. Besides a 300% difference in thickness, the coatings appear visually distinct. C14 is a matte black surface (shown in Fig 5–20a), while C15 is semi-transparent with a brown tint (similar to C16 shown in Fig. 5–20b). Coating C15 also displays a circular pattern on its surface, which is thought to be a thickness/transparency induced diffraction pattern. Experimentally, the difference between C14 and C15 is the orientation of the deflection patterns, shown in Fig. 5–17.

The beam speeds, shown in Fig. 5–18, demonstrate a very marginal difference between the two patterns.

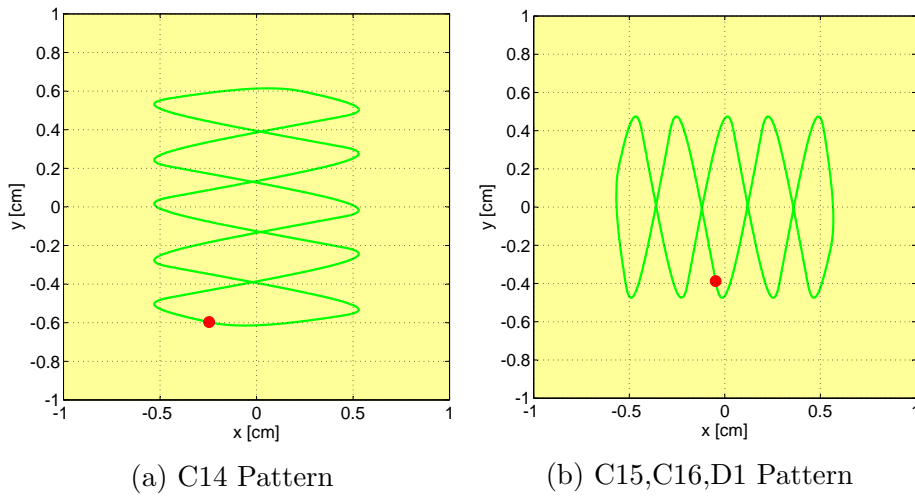


Figure 5-17: Deflection pattern comparison for C14 and C15

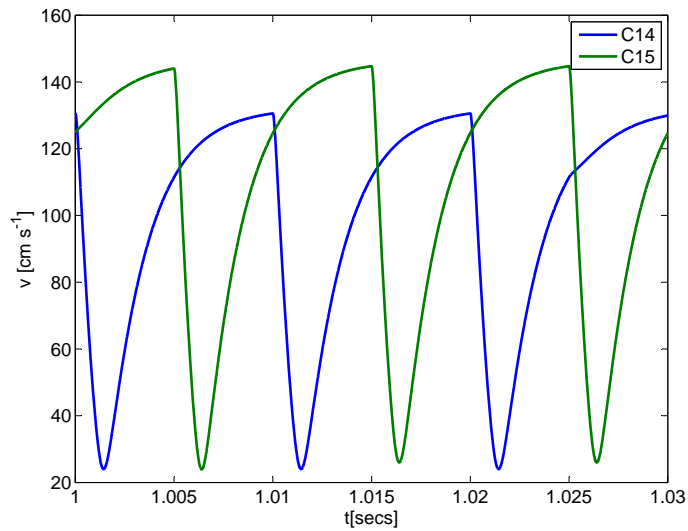


Figure 5-18: Beam speed comparison between C14 and C15

It is believed that the difference between C14 and C15 is due to the geometry of the electron beam gun. Specifically, if we return to Section 3.2.3, we see that the tilt of the electron beam gun results in an ellipsoidal beam spot at the target. For the patterns shown in Fig. 5-17, the ellipsoidal projection will results in

a 70% longer dwell time for C14 compared to C15. Also, the thermophysical material parameters shown in Fig. 5–19 demonstrate that Al_2O_3 has a low thermal diffusivity, making evaporation extremely sensitive to dwell times. Combined with the relative vapour compositions of Fig. 5–15b, we can only qualitatively state that the beam shape is the defining factor, without further advancements in experimentation and modelling.

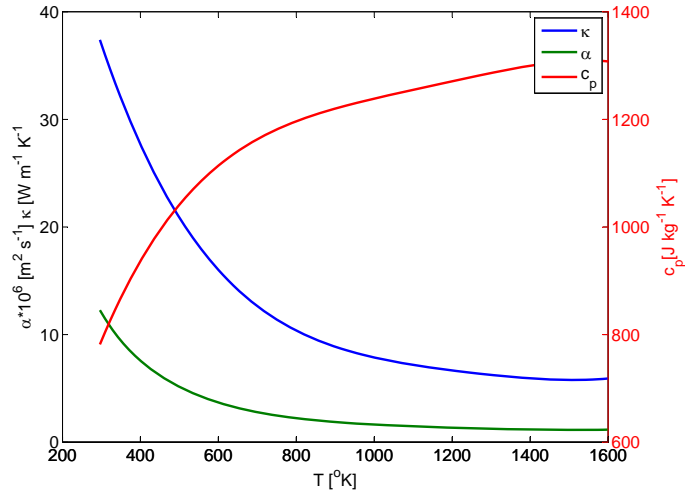


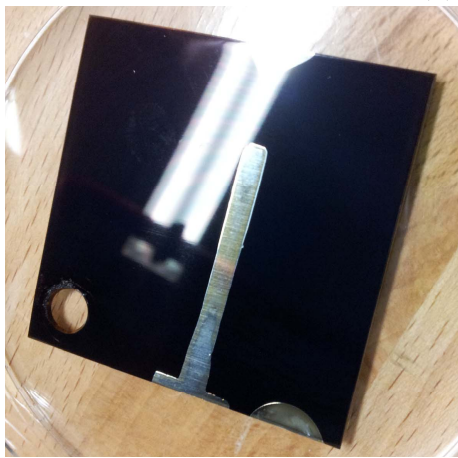
Figure 5–19: Thermophysical material parameters of Al_2O_3 [4]

Examining the C15, C16, D1 series, we see that the major distinction between the coatings is the target-substrate separation distance, h . Interestingly, coating D1 had a white-ish color (shown in Fig. 5–20c) while C15 and C16 were transparent and brown (shown in Fig. 5–20b). In the case of YSZ, the color is indicative of the oxide stoichiometry [20].

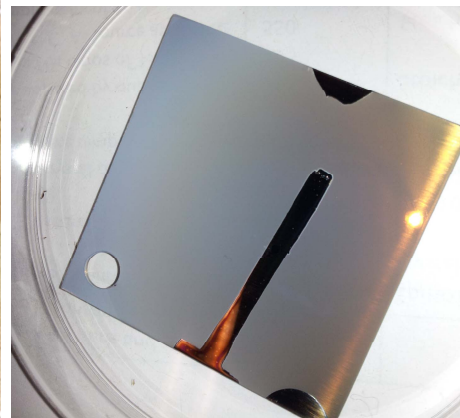
It is believed that the difference in these results is due to the substrate temperature, which will increase with decreasing distance to the target due to radiative and BSE heating. This is especially true if we carefully examine the color



(a) C14



(b) C16



(c) D1

Figure 5–20: Deflection pattern comparison for C14 and C15

of D1, and see that the whiter regions are towards the periphery of the substrate, which will achieve a higher temperature since there will be reduced conduction to the substrate holder.

Finally, we can examine the difference in expected coating thickness of C16 and D1. Assuming a deposition circle of radius $s = 6$ mm (equivalent area of Fig. 5–17b) and equivalent evaporated mass, the expected ratio of maximum coating thickness, according to Eq. 5.9, is $d_{D1}/d_{C16} = 2.2$ while the measured value

is 3.1. It is not clear what exactly is causing this deviation, but D1 appears to be more porous, according to the lower net mass gain divided by net thickness value calculated in Table 5–4. It might be possible that a viscous cloud similar to Fig. 5–10, thus creating a virtual source at $h_v < h$. This idea is also supported by the fact that the chamber view port had significantly smaller coating compared to thinner Ni coatings.

These rather surprising results demonstrate the complexity associated with oxide evaporation. Through four separate experiments, we have demonstrated the interplay between beam parameters, vacuum conditions/gas content, heat transfer, microstructure and chemical reactivity.

Early work on YSZ deposition

As mentioned, electron beam technology diverged at the end of the cold war, with the East developing axial coaters and the West developing transverse coaters. Yet, in the 1980s, both entities researched EB-PVD of Yttria-stabilized Zirconia (YSZ) for aerospace applications using the respective technologies, with the Soviets flying EB-PVD TBCs in 1985 and the West flying in 1989. [20]

In a paper which is suspected to have been published in 1997, [20] Jaslier compares YSZ coatings made with those competing technologies. In the early stages of TBC development, the Western researches used a reactive oxygen atmosphere of 10^{-2} mbar with a 270° transverse gun. The Eastern researchers did not admit oxygen into the deposition chamber, yet achieved stoichiometric coatings at a pressure of 10^{-4} mbar using axial guns. It is possible that the higher power

density of the Eastern EB-PVD coaters resulted in less dissociation, thereby negating the need for additional O₂.

Similarly, the paper claims that Western coaters used radiative and condensation heat to set the substrate temperature, while Eastern workers used a separate electron beam gun. The main focus of the paper is the analysis of the differences in microstructure, but does hint at the complexity surrounding the beam parameters, vacuum parameters and coating performance. The paper also states that the strategic nature of TBC technology makes the processing parameters closely guarded secrets.

Finally, as far as this author can tell, state-of-the-art TBCs produced in the West are applied using axial guns in a reactive oxygen atmosphere of 10⁻³ mbar.

5.4 Vapour Adsorption and Diffusion on a Substrate

Once created, the vapour condenses onto the substrate and forms a coating. Although vapour phase material growth dynamics are not the focus of this thesis, the generation of useful microstructure is paramount to any PVD technique, and will be briefly discussed.

The authors of the seminal *Handbook of deposition technologies for films and Coatings* suggests that the most important factors affecting vapour phase growth are: [75]

- Composition of condensing atoms
- Substrate temperature
- Coating thickness
- Substrate material, cleanliness, crystallinity and orientation

- Deposition rate
- Kinetic energy of atoms impinging on substrate
- Angle of incidence of vapour atoms
- Net and partial pressures within the chamber vacuum

A significant fraction of the microstructure variation appears to be due to the energy of the freshly condensed adatoms. This is demonstrated in the ubiquitous Thornton zone diagram, shown in Fig. 5–21.

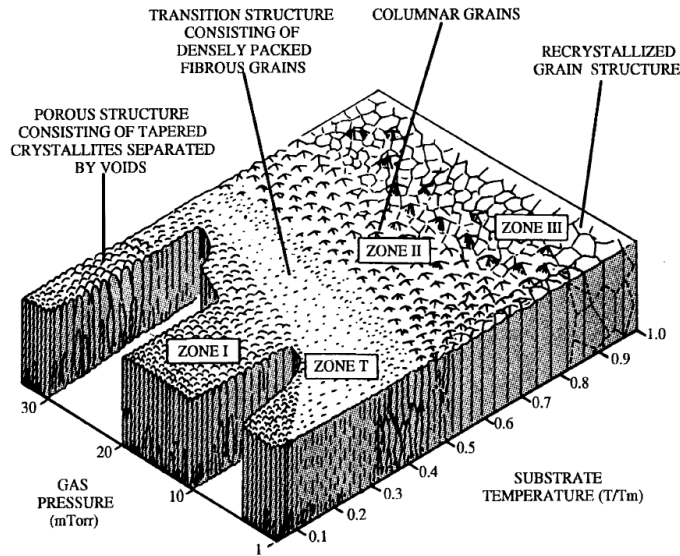


Figure 5–21: Thornton Zone Model: Study of sputtering microstructure revealed repeatable trends: improved coatings can be achieved with appropriate substrate temperature and low residual chamber pressure [76]

As the chamber pressure increases, energetic vapour molecules collide with the surrounding cold gas molecules, and lose kinetic energy in a process called thermalization. The degree of thermalization is proportional to the mean free path of the vapour/gas collisions (ie pressure) versus the source/substrate distance. [55]

Adatoms depositing with low energies have limited ability to move across the surface, forming a porous microstructure. Similarly, low substrate temperature makes less energy available to the arriving adatoms. Thus, their ability to jump from one surface site to the next is reduced, again resulting in a porous microstructure.

CHAPTER 6

Conclusion

The results and discussion presented throughout this research demonstrate the multidisciplinary nature of the EB-PVD process. The main topics covered include vacuum technology, electron beam guns, target heating, heat transfer, vapour transport and vapour condensation. The experiments presented demonstrate the relative magnitude of these process parameters, as well as their interdependencies. At a fundamental level, the challenge of EB-PVD stems from the exponential temperature dependence of the evaporation rate, as defined by the Langmuir equation.

In Chapter 2, the details of the high vacuum environment were discussed. Specific concepts include the molecular flow regime; the relationship between outgassing, pumping speed and base pressure; impingement rate ratio between vapour/gas molecules and vacuum-compatible processes and materials. As shown in later sections, the vacuum affects the e^- beam propagation, evaporation, vapour transport and coating reactions. The Thornton zone model also demonstrates that the pressure is critical in defining the coating microstructure via thermalization. Thus, the vacuum represents a fundamental component of EB-PVD.

In Chapter 3, the specifics of electron beam generation and deflection were presented. Discussions centered on electron emission, current regulation and beam pulsing, beam focus and deflection. These parameters are often referred to as the

electron optics, and they effectively define the local and global heat deposition. A simple model for the deflection coil transfer function was created, and is one of the first steps towards understanding the heat deposition process. Also, the gun/target geometry was analysed from the perspective of beam projection and working distance.

Chapter 4 discussed the electron beam and matter interactions. The fundamental concept of in/elastic electron scattering was presented as a link between electron propagation in a vacuum and a solid. Although vapour is the desired output of the e^- beam, the concept of thermal accounting demonstrates the parasitic effects of X-rays, heat conduction, radiation, BSE and SE. CASINO was used as a means of calculating the BSE power losses as a function of target material and beam parameters. The concept of local and global temperature was demonstrated with a series of nickel evaporations. A simple 1^D heat transfer model was presented, which captures some of the salient features of electron beam evaporation.

Chapter 5 focussed on the process of vapour generation, propagation and vapour condensation. The Langmuir equation was presented, and experimental results representing alloy evaporation(Ti64), co-evaporation(Cu-Ni) and oxide(Al_2O_3) evaporation were given. Although oxide evaporation was one of the initial objectives of this research, the challenges of oxide deposition are increased due to dissociation and charging. Target spitting demonstrates one of the most important constraints of the EB-PVD process: the surface temperature must be high enough to achieve an appreciable evaporation rate, but not high enough to

bring about spitting. A brief discussion regarding vapour condensation and coating microstructure was also presented, with a mention to the Thornton zone model.

Conceptually, the EB-PVD process is simple: heat a surface to a predefined temperature such that the material evaporates then condenses onto a substrate. Technically, it is significantly more complicated, as many phenomena are simultaneously interacting. Also, because of the extreme temperatures involved, the process parameters can only be measured indirectly. Nevertheless, EB-PVD is a versatile coating technique which has and will continue to figure prominently in many fields of engineering.

6.1 Future Work

This work paints a macroscale picture of the EB-PVD process, and thus, no in-depth investigations were performed on a particular process parameter or coating output. It should now be evident that a particular target coating composition, microstructure or thickness requires specific hardware and procedures tailored to the electron beam gun and thermophysical material parameters. Thus, although the work is preliminary, the results contained in this document should serve as a starting point for any future electron beam processing using the PAVAC equipment.

6.1.1 Hardware and Process Work

In terms of process development, hardware and software improvements will be required to accurately regulate the substrate temperature during deposition. Although not a focus of this work, the Thornton zone model demonstrates that the substrate temperature is one of the most important coating process parameters.

An improved substrate holder will be required to stabilize the substrate conduction losses and simplify the thermocouple measurements. Once installed, the substrate heater, which is another electron beam gun, will need to be optimized to achieve a uniform temperature over the condensing surface. This should not be a difficult task, as much of the theory and practice discussed in this work will be directly applicable to the substrate heater.

Repeatable coatings will require an advanced target crucible which stabilizes the radiative and conductive heat losses. Conventional EB-PVD systems utilize a water-cooled copper crucible such that the temperature gradient between the evaporating surface and cooling water reaches steady state. This hardware should improve the predictability of the co-evaporation process. Also, by carefully choosing the appropriate crucible, target materials in pellet or chuck form can be used, as opposed to the 4" sputter targets used at the moment.

Finally, reliable deposition of oxides will require further investigation in order to determine if the beam parameters can be adjusted to result in stoichiometric oxides. The possibility of reactive evaporation should also be considered, but will require significant hardware development, including mass flow controllers, butterfly vacuum valves and electron beam constrictions to decouple the evaporation and gun chambers. Higher evaporating pressures will also allow for plasma-enhanced deposition.

All of the above recommendations are suggested in order to decouple the process parameters. This is a necessary pre-requisite for research and development,

as it allows the process parameters to be independently mapped against the coating performance.

6.1.2 Experimental Work

There still remains significant experimental work to be done on characterizing the electron beam gun, and heat transfer characteristics, not mention to the actual coatings themselves. Firstly, the newly installed electron beam gun will need to be characterized according to the techniques described in this thesis.

Further work should be done on understanding the energy density of the beam as a function of focus current, beam current and pulse setting. It is believed that these values will be critical in predicting the evaporation characteristics of a given material. Potential methods include Faraday cup measurements and bead on plate welds. The focal length/focus coil transfer function should be more thoroughly investigated in order to dynamically adjust the focus current as a function of deflection dependent working distance. These measurements will also be useful if less intense beams are needed for rapid annealing or sintering.

At the moment, the pulse length dependency of optimal focus is not understood. Possibilities include the space-charge effects of electron bunches, electromagnetic wake fields, transit-time effects, capacitance between the bias cap and cathode, or some combination of the above. Future work should examine the interplay between accelerating voltage, beam current, focus current, pulse length and duty cycle with the objective of teasing out the mechanisms which make the

focus pulse-length dependent. As the nickel evaporations have shown, the evaporation depends on the beam focus, thus pulsed evaporation cannot be rigorously investigated until this focusing problem is understood.

Since oxide coatings are to be further pursued, the interplay between deflection patterns, beam focus and dissociation must be further investigated. This requires an in-depth chemical analysis of the coating, in order to map the stoichiometry versus the beam parameters. As was shown, the oxide charging parameters are dependent on the thermal history of the target, and it is unknown whether repeatable results can be achieved when re-using the same target.

These tasks speak to the multi-disciplinary nature of the EB-PVD process, and future researchers should be prepared to step outside of their comfort zone. Although the long term objective is a coatings user-facility, the current status of the machine requires researchers who are familiar with optics, mechanical and electrical engineering, vacuum technology, heat transfer and coatings characterization.

Appendices

APPENDIX A

Abbreviations

PVD	Physical Vapor Deposition
PEB-PVD	Pulsed Electron-Beam Physical Vapor Deposition
EB-PVD	Electron-Beam Physical Vapor Deposition
TBC	Thermal Barrier Coatings
BSE	Back-Scattered Electrons
SE	Secondary Electrons
YSZ	Yttria-stabilized Zirconia
PED	Pulsed Electron-beam Deposition
CW	Continuous Wave
PLD	Pulsed Laser Deposition
ARE	Activated Reactive Evaporation
HVPS	High Voltage Power Supply
ESD	Electron Stimulated Desorption
HV	High Vacuum
FWHM	Full Width Half Maximum
ESD	Electron Stimulated Desorption
ML	Monolayer
RE	Reactive Evaporation
ODE	Ordinary Differential Equation

PDE Partial Differential Equation

WD Working Distance

RTOS Real-Time Operating System

References

- [1] W.F. Gale and T.C. Totemeier. *Smithells Metals Reference Book (8th Edition)*. Elsevier, 2003.
- [2] Kenneth Mills. *Recommended Values of Thermophysical Properties for Selected Commercial Alloys*. Woodhead Publishing, 2002.
- [3] Milton Farber, R. D. Srivastava, and O. M. Uy. Mass spectrometric determination of the thermodynamic properties of the vapour species from alumina. *J. Chem. Soc., Faraday Trans. 1*, 68:249–258, 1972.
- [4] Touloukian. *Specific heat: nonmetallic solids*. Plenum, 1970.
- [5] Ji-Cheng Zhao, Melvin R. Jackson, Louis A. Peluso, and Luke N. Brewer. A diffusion multiple approach for the accelerated design of structural materials. *MRS Bulletin*, 27(04):324–329, 2002.
- [6] A Powell. *Transport Phenomenon in Electron Beam melting and evaporation*. PhD thesis, Massachusetts Institute of Technology, 1997.
- [7] A Mitchell and T Wang. Electron beam melting technology review.
- [8] DM Mattox. *Handbook of physical vapor deposition (PVD) processing : film formation, adhesion, surface preparation and contamination control*. Noyes, 1998.
- [9] J. F O’Hanlon. *A Users Guide to Vacuum Technology*. John Wiley and Sons, 1989.
- [10] M. H Hablanian. *High Vacuum Technology: A practical guide*. Marcel Dekker Inc, 1997.
- [11] BS Halliday. Cleaning materials and components for vacuum use. *Vacuum*, 37(89):587 – 591, 1987.
- [12] All-foil inc. Strongsville, Ohio.

- [13] Leon Maissel and Reinhard Glang. *Handbook of thin film technology*. McGraw Hill, 1970.
- [14] R Hill. *Physical Vapor Deposition*. Temescal a division of the BOC Group Inc, 1989.
- [15] Siegfried Schiller. *Electron Beam Technology*. John Wiley & Sons Ltd., 1982.
- [16] D Wolfe, J Singh, R Millerb, and J Eldridgeb. Tailored microstructure of EB-PVD 8YSZ thermal barrier coatings with low thermal conductivity and high thermal reflectivity for turbine applications. *Surface and Coatings Technology*, 190(E2):132–149, 2004.
- [17] Wikipedia. Molecular beam epitaxy — Wikipedia, the free encyclopedia, 2012. [Online; accessed 24-July-2012].
- [18] BS Halliday. An introduction to materials for use in vacuum. *Vacuum*, 37(89):583 – 585, 1987.
- [19] GM Mladenov. Development of the electron beam melting and refinig in the eastern europe.
- [20] Eb-pvd of thermal barrier coatings: a comparative evaluation of competing deposition technologies. <http://ftp.rta.nato.int/public/PubFullText/AGARD/R/AGARD-R-823/08chap08.pdf>. Accessed: 2013-11-27.
- [21] Miroslave Sedlacek. *Electron Physics of vacuum and gaseous devices*. John Wiley and Sons, 1996.
- [22] J Goldstein. *Scanning Electron Microscopy and X-ray microanalysis*. Springer, 2003.
- [23] J Elmer. Characterization of defocused electron beams and welds in stainless steel and refractory metals using the enhanced modified faraday cup diagnostic. *Technical Information Center Oak Ridge Tennessee*, 2009.
- [24] Hideo Nakamura. *The effect of beam oscillation rate on the evaporation behavior in electron beam melting*. PhD thesis, University of British Columbia, 1989.
- [25] R. Edinger. private communication, 2012.

- [26] A von Ardenne and H Forster. Von ardenne electron beam guns: 30 years of progress.
- [27] A Mitchell. Fundamental development in electron beam melting processes.
- [28] G Franz. *Low pressure plasmas and microstructuring technologies*. Springer, 2009.
- [29] K Amboss. A review of the theory of space charge limited operation.
- [30] DM Tripp. *Modelling power transfer in electron beam heating of cylinders*. PhD thesis, University of British Columbia, 1995.
- [31] Edward B. Graper. Evaporation characteristics of materials from an electron-beam gun. *Journal of Vacuum Science and Technology*, 8(1):333–337, 1971.
- [32] Mikhail Stikovski and K.S. Harshavardhan. Parameters that control pulsed electron beam ablation of materials and film deposition. *Applied Physics Letters*, 82(6), 2003.
- [33] Dominique Drouin, Alexandre Real Couture, Dany Joly, Xavier Tastet, Vincent Aimez, and Raynald Gauvin. Casino v2.42-a fast and easy-to-use modeling tool for scanning electron microscopy and microanalysis users. *Scanning*, 29(3):92–101, 2007.
- [34] P Fischer, Valerio Romano, Hans-Peter Weber, NP Karapatis, Eric Boillat, and Rémy Glardon. Sintering of commercially pure titanium powder with a nd: Yag laser source. *Acta Materialia*, 51(6):1651–1662, 2003.
- [35] BD Cullity. *Elements of X-Ray Diffraction*. Addison-Wesley, 1978.
- [36] FP Incropera and DP DeWitt. *Introduction to heat transfer*. John Wiley and Sons, 1990.
- [37] A Mitchell. Modelling the thermal fields in electron beam remelted ingots.
- [38] M Ritchie, A Mitchell, and CK Rhee. Experimental determination of the effect of fluid flow on composition changes and evaporation during eb melting.
- [39] MC McClelland. Experimental and numerical study of e-beam evaporation of titanium. In R Bakish, editor, *Electron beam melting and refining-State of the Art*, 1996.

- [40] Matlab. <http://www.mathworks.com/products/matlab/>. Accessed: 2013-11-27.
- [41] H Duval. Theoretical and experimental approach of the volatilization in vacuum metallurgy. In R Bakish, editor, *Electron beam melting and refining-State of the Art*, 1997.
- [42] C.W. Bale, P. Chartrand, S.A. Degterov, G. Eriksson, K. Hack, R. Ben Mahfoud, J. Melançon, A.D. Pelton, and S. Petersen. Factsage thermochemical software and databases. *Calphad*, 26(2):189 – 228, 2002.
- [43] J Storer. Electron beam evaporation for titanium metal matrix composites. In R Bakish, editor, *Electron beam melting and refining-State of the Art*, 1994.
- [44] Robert A. Miller. Current status of thermal barrier coatings: An overview. *Surface and Coatings Technology*, 30(1):1 – 11, 1987.
- [45] Douglas E. Wolfe, Jogender Singh, Robert A. Miller, Jeff I. Eldridge, and Dong-Ming Zhu. Tailored microstructure of eb-pvd 8ys thermal barrier coatings with low thermal conductivity and high thermal reflectivity for turbine applications. *Surface and Coatings Technology*, 190(1):132 – 149, 2005.
- [46] Teuvo Santala and Jr. C. M. Adams. Kinetics and thermodynamics in continuous electron-beam evaporation of binary alloys. *Journal of Vacuum Science and Technology*, 7(6), 1970.
- [47] James S. Foster and W. H. Pfeifer. Vacuum deposition of alloys; theoretical and practical considerations. *Journal of Vacuum Science and Technology*, 9(6):1379 – 1384, nov 1972.
- [48] H Lammermann. Pvd- overlay coatings for blades and vanes of advanced aircraft engines. In R Bakish, editor, *Electron beam melting and refining-State of the Art*, 1991.
- [49] KW Westerberg. Analysis of the e-beam evaporation of ti and ti-6al-4v. In R Bakish, editor, *Electron beam melting and refining-State of the Art*, 1997.
- [50] D. Hass. *Directed Vapor Deposition of Thermal Barrier Coatings*. PhD thesis, University of Virginia, 2000.

- [51] U. Schulz, K. Fritscher, and C. Leyens. Two-source jumping beam evaporation for advanced eb-pvd {TBC} systems. *Surface and Coatings Technology*, 133?134(0):40 – 48, 2000.
- [52] M. Oron and C.M. Adams. Controlled electron beam co-deposition of copper-nickel films. *Journal of Materials Science*, 4:252–258, 1969.
- [53] J.J. Hanak. The ?multiple-sample concept? in materials research: Synthesis, compositional analysis and testing of entire multicomponent systems. *Journal of Materials Science*, 5(11):964–971, 1970.
- [54] K. Kennedy, T. Stefansky, G. Davy, V. F. Zackay, and E. R. Parker. Rapid Method for Determining Ternary-Alloy Phase Diagrams. *Journal of Applied Physics*, 36:3808–3810, December 1965.
- [55] J. Groves. *Directed Vapor Deposition*. PhD thesis, University of Virginia, 1998.
- [56] H Smith. Deposition distribution and rates from electron-beam heated vapor sources. In *12th Annual Technical Conference- Soceity of Vacuum Coaters*, 1969.
- [57] E. Darrell Erikson. Thickness distribution of a metal-alloy from a high-rate electron-beam source. *Journal of Vacuum Science and Technology*, 11(1):366–370, 1974.
- [58] G Mattausch. A novel eb evaporation tool for directed vapor deposition. In R Bakish, editor, *Electron beam melting and refining-State of the Art*, 1995.
- [59] D.V. Rigney, R. Viguie, D.J. Wortman, and D.W. Skelly. Pvd thermal barrier coating applications and process development for aircraft engines. *Journal of Thermal Spray Technology*, 6(2):167–175, 1997.
- [60] P Meier. Empirical observations of eb-pvd: Novel diagnostics tools at llnl. In R Bakish, editor, *Electron beam melting and refining-State of the Art*, 1995.
- [61] Edward B. Graper. Evaporation characteristics of materials from an electron beam gun ii. *Journal of Vacuum Science Technology A: Vacuum, Surfaces, and Films*, 5(4):2718–2723, 1987.

- [62] U. Schulz, K. Fritscher, and M. Peters. Eb-pvd Y_2O_3 - and $\text{CeO}_2\text{Y}_2\text{O}_3$ -stabilized zirconia thermal barrier coatings: crystal habit and phase composition. *Surface and Coatings Technology*, 82(3):259 – 269, 1996.
- [63] E Reinhold, P Botzler, and C Deus. Eb-pvd process management for highly productive zirconia thermal barrier coating of turbine blades. *Surface and Coatings Technology*, 120?121(0):77 – 83, 1999.
- [64] H.M. Christen. Pulsed electron deposition of fluorine-based precursors for ybco coated conductors. *Superconducting Science and Technology*, 18, 2005.
- [65] P.A. Cox. *Transition Metal Oxides*. Clarendon Press, 1995.
- [66] V Matolin, V Nehasil, L Bideux, C Robert, and B Gruzza. Vacuum evaporation of thin alumina layers. *Thin Solid Films*, 289(1?2):295 – 299, 1996.
- [67] E Ritter. Deposition of oxide films by reactive evaporation. In *12th National Vacuum Symposium, N.Y.*, 1966.
- [68] R. F. Bunshah and A. C. Raghuram. Activated reactive evaporation process for high rate deposition of compounds. *Journal of Vacuum Science and Technology*, 1972.
- [69] Hari Nalwa. *Deposition and Processing of Thin Films*. Academic Press, 2002. *Ch 13: Pulsed laser deposition of thin films: expectations and reality*.
- [70] R.F. Bunshah. The activated reactive evaporation process: Developments and applications. *Thin Solid Films*.
- [71] S Schiller. New developments for plasma-activated high rate eb-evaporation for metal strip. In R Bakish, editor, *Electron beam melting and refining-State of the Art*, 1994.
- [72] H Morgner and G Mattausch. Plasma activation for directed deposition - a new application for hollow cathode arc plasmas. In R Bakish, editor, *Electron beam melting and refining-State of the Art*, 1995.
- [73] P Lenk. von ardenne electron beam guns and their suitability for pvd processes for tbc's. In R Bakish, editor, *Electron beam melting and refining-State of the Art*, 1995.

- [74] YP Jaslier and year = 1999 month = 06 day = 3 number = US 6251504
B1 type = Patent location = US AH Malie, title = Ceramic heat barrier
coating having low thermal conductivity, and process for the deposition of
said coating.
- [75] R Bunshah. *Handbook of Deposition Technologies for Films and Coatings*.
Elsevier Science, 1994.
- [76] John A Thornton. High rate thick film growth. *Annual review of materials
science*, 7(1):239–260, 1977.